DETERMINATION OF DYNAMIC FRACTURE TOUGHNESS OF BORON MODIFIED AS-CAST Ti-6Al-4V ALLOYS

M.Tech. Thesis

By

AAYUSH PATHAK

DISCIPLINE OF METALLURGICAL ENGINEERING AND MATERIALS SCIENCE

INDIAN INSTITUTE OF TECHNOLOGY INDORE

JUNE 2023

DETERMINATION OF DYNAMIC FRACTURE TOUGHNESS OF BORON MODIFIED AS-CAST Ti-6Al-4V ALLOYS

A THESIS

Submitted in partial fulfillment of the
requirements for the award of the degree
of
Master of Technology

by

AAYUSH PATHAK

DISCIPLINE OF METALLURGICAL ENGINEERING AND MATERIALS SCIENCE

INDIAN INSTITUTE OF TECHNOLOGY INDORE

JUNE 2023

INDIAN INSTITUTE OF TECHNOLOGY INDORE

CANDIDATE'S DECLARATION

I hereby certify that the work which is being presented in the thesis entitled **DETERMINATION OF DYNAMIC FRACTURE TOUGHNESS OF BORON MODIFIED AS-CAST Ti-6Al-4V ALLOYS** in the partial fulfillment of the requirements for the award of the degree of **MASTER OF TECHNOLOGY** and submitted in the **DISCIPLINE OF METALLURGICAL ENGINEERING AND MATERIALS SCIENCE, Indian Institute of Technology Indore**, is an authentic record of my own work carried out during the time period from August 2021 to May 2023 under the supervision of Dr. Eswara Prasad Korimilli, Associate Professor, Department of Metallurgical Engineering and Materials Science, IIT-Indore.

The matter presented in this thesis has not been submitted by me for the award of any other degree of this or any other institute.

31-05-23

Signature of the student with date
(AAYUSH PATHAK)

This is to certify that the above statement made by the candidate is correct to the best of my/our knowledge.

K. Eswara Prasad

Signature of the Supervisor of M.Tech. thesis (with date)

(Dr. K. ESWARA PRASAD)

AAYUSH PATHAK has successfully given his M.Tech. Oral Examination held on **25th May 2023**.

K. Eswara Prasad

Signature(s) of Supervisor(s) of M.Tech. thesis
(Dr. K. ESWARA PRASAD)
Date: 01-06-2023

Convener, DPGC
(Dr. SUMANTA SAMAL)
Date:

31/05/2023

Signature of PSPC Member #1
(Dr. VINOD KUMAR)
Date: 31-05-2023

31/05/2023

Signature of PSPC Member #2
(Dr. I.A. PALANI)
Date: 31-05-2023

ACKNOWLEDGEMENTS

I would like to extend my heartfelt gratitude to Dr. Eswara Prasad Korimilli, my research supervisor, for his unwavering support and continuous guidance throughout the course of this project. His invaluable input and insightful suggestions have played a pivotal role in shaping and progressing my work. His friendly and approachable nature has fostered a positive and collaborative environment, allowing for fruitful interactions and constructive discussions. His unwavering support has been a constant source of motivation, helping me navigate through the various stages of this endeavor. Furthermore, I am immensely grateful for his keen attention to detail in every aspect of the project, whether it be presentations or written work. His meticulousness has instilled in me a greater sense of perfectionism, pushing me to strive for excellence in all that I do. I will forever cherish the valuable teachings I have received from him, as they have not only enhanced my academic knowledge but have also become an integral part of my core values.

I would like to express my gratitude to Dr. Vinod Kumar and Dr. I.A. Palani, the members of my PSPC, for their generous commitment of time in evaluating my work. Their suggestions and comments have been invaluable and have greatly enriched my project.

I would like to express my sincere appreciation to Dr. Syed Nizamuddin Khaderi, Associate Professor at IIT-Hyderabad, for his diligent efforts in conducting the Dynamic Fracture Experiments and engaging in enlightening discussions related to the SHPB.

I express my gratitude to my colleagues Abhinav, Tulika, Janmejai and Sourav for their valuable knowledge sharing regarding the instruments utilized in my experimental studies. Observing their work methodology has been a constant source of motivation for me, encouraging me to adopt a similar mindset and approach. They have consistently demonstrated a willingness to explain concepts whenever I sought their guidance. I am deeply appreciative of the insightful discussions we have had, as they have greatly enhanced my understanding of materials on a conceptual level.

I would like to express my gratitude to the seniors who have supported me during the experimental phase of my work at IIT-Indore. I extend my heartfelt appreciation to the Technical Staff, namely Mr. Mayur Dhake, Mr. Shubham Verma, and Mr. Pranjal Srimali, for their dedicated efforts in ensuring my access to the necessary instruments and for placing their trust in me while handling them. Their assistance has been invaluable, and I am sincerely thankful for their support and belief in my abilities.

I express my gratitude to all my friends who have imparted a multitude of valuable lessons in various aspects of life within a remarkably brief timeframe.

Lastly, I extend my gratitude to my parents and my family for their unwavering support and serving as a perpetual source of inspiration in my life.

DEDICATION

This thesis is dedicated to my parents, family, and friends
for their unwavering support and constant inspiration throughout my journey.

ABSTRACT

The Ti-6Al-4V alloy is highly regarded as the dominant Titanium alloy due to its exceptional specific and fatigue strength, as well as its resistance to oxidation. These qualities make it a favored material in the aerospace industry. However, its widespread use is hindered by the significant costs involved in its wrought processing, which typically requires mechanical working at elevated temperatures beyond its β-transus temperatures to achieve a refined grain size. Recent research has demonstrated that incorporating small amounts of Boron into Ti-6Al-4V alloys aids in grain size refinement, thereby eliminating the need for extra thermo-mechanical steps in processing. Furthermore, the mechanical properties of Boron-modified Ti-6Al-4V alloys have been found to be nearly equivalent to those processed by conventional means. Given that these alloys are frequently exposed to impact loadings in real-life applications, understanding the fracture mechanisms under such high loading rates is both intriguing and essential for designing structures with improved resistance to fracture.

To achieve our research goal, we performed Dynamic Fracture experiments on Ti-64 alloys that were modified with varying weight percentages of Boron (0, 0.04, 0.09, 0.3, and 0.55 wt. %). These experiments involved subjecting the Boron modified Ti-64 alloy samples to dynamic loading conditions using a specially designed fixture and a modified Kolsky bar. The loading rates achieved during the experiments ranged from 10^6 to 10^7 $MPa\sqrt{m}s^{-1}$. To capture and analyze the crack growth dynamics, we employed a combination of strain gauge study and High-Speed camera imaging techniques. Additionally, we aimed to quantify the K_{ID} values for these alloys using multiple methods, including Peak Load, CMOD (Crack-Mouth Opening Displacement), LPD (Load-Point Displacement), and PZS (Plastic-Zone Size). Interestingly, all these methods exhibited a consistent trend in their results. Notably, we observed that the sample with 0.04 wt. % Boron addition demonstrated the highest K_{ID} values among all the samples tested, followed by a gradual decline as the Boron content increased.

TABLE OF CONTENTS

LIST OF FIGURES

LIST OF TABLES

Chapter 1

INTRODUCTION

This chapter offers the fundamental foundation necessary to comprehend the research that was done and presented in this thesis. This chapter starts out by giving a quick introduction of titanium and its alloys, as well as its significance. The metallurgy of titanium, with special emphasis on the crystal structure, is covered in the following section. The alloying elements and their properties, as well as some of the titanium alloys that are used commercially, are addressed in the section after this one. When we move on to the following section, we also address microstructures and deformation modes of titanium at various strain rates. The earlier research on boron modification emphasising the changes in mechanical properties is also briefly described. The apparatus utilised and the changes made to carry out the dynamic fracture studies are covered in the last section.

1.1 Motivation

With a density that is halfway between the traditional light metal Aluminium (Al) and the most extensively used metal on earth, Iron (Fe), Titanium (Ti) is regarded as the heaviest light metal. Leyens C and Peters M [1] in their book discuss that $5gcm^{-3}$ is the value of density that separates the lighter metals with the heavier ones (Fig 1.1). There are many successful applications that require high levels of reliable performance in aerospace [2]–[4] , defence [5] chemical, medicine [6]–[9] and other major industries thanks to titanium and its alloys' exceptional resistance to corrosive environments and high strength to weight ratio, both of which are inherent properties of it. Titanium has replaced heavier, less functional, and costlier materials in many technical applications.

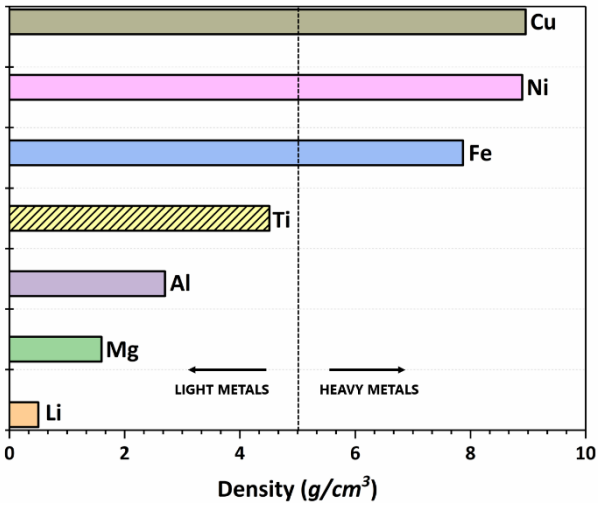

Fig 1.1: Comparison of densities of different metals with Titanium (Reprod. From [1])

Figure 1.2 discusses the variation of Strength (σ_f) with Maximum Serviceable Temperature (°**C**). Carbon Fibre Reinforced Polymers (CFRPs) only outperform titanium alloys in terms of specific strength below 300°C. Titanium alloys are particularly desirable at higher temperatures due to their high strength in that regime. Their oxidation behaviour does,

however, set a maximum application temperature limit (≈ **600°C** [10]). Due to the fact that titanium aluminides somewhat solve this drawback, they are the focus of considerable alloy development efforts. TiAl-based alloys are in direct competition with firmly rooted high temp. steels and Ni-base super-alloys, whereas titanium alloys designed for higher temperatures are generally employed up to temperatures slightly surpassing 500°C.

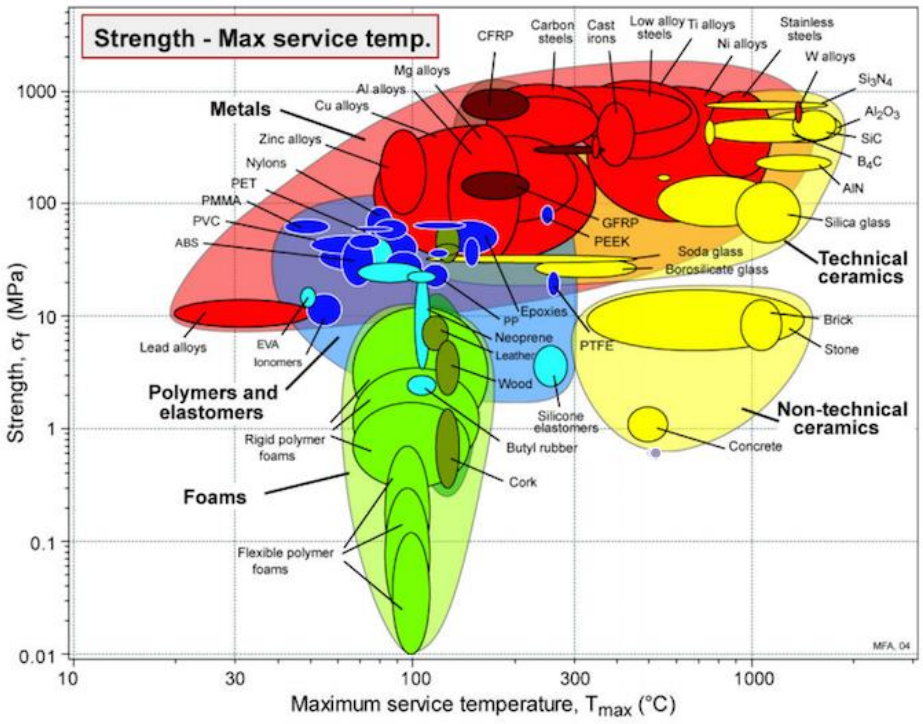

Fig 1.2: Variation of Strength (σ_f) with Maximum Service Temperature (**°C**) for various materials

Out of all the commercially available Ti alloys the Ti-6Al-4V alloy (where 6 and 4 represent the wt % of Aluminium and Vanadium added to it) is the most extensively used one. This alloy demonstrates superior performance across a range of weight-reduction applications in aerospace, automotive, and marine equipments. There are numerous uses for Ti6Al-4V in the field of medicine. Ti-6Al-4V has outstanding biocompatibility, especially when it is necessary to make direct contact with bone or tissue. Liu *et al* [11] discuss the areas where Ti-64 is used in an aircraft and it includes parts like: Wing Box, Engine, Landing Gear, Cockpit Window Frame just to name a few.

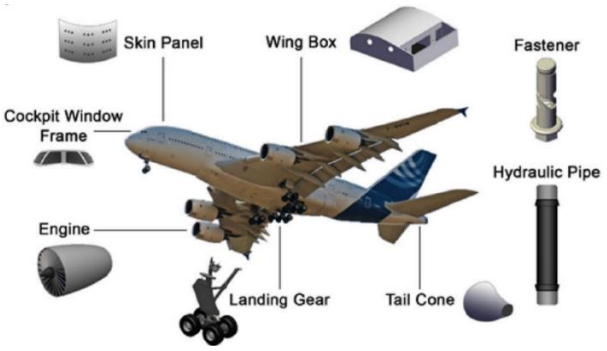

Fig 1.3: Areas where Ti-6Al-4V is used in an aircraft [11]

Such structures experience high strain rates of loading for example the panels of the aircraft during a bird strike or the landing gear when the aircraft comes in contact with the ground upon landing. Yan *et al* [12] describe the order of strain rates for the landing gear to be of the order of $10^4\,s^{-1}$ to $10^5\,s^{-1}$ and thus High Strain Rate studies on such materials is necessary in order to predict their failure behaviour at such loading rates. KT Ramesh [13] discusses the type of experimental setups for different ranges of strain rates and the use of Miniatured Split Hopkinson Bar comes into picture. The regular SHPB differs from the miniatured one in the following ways:

- In comparison to a regular SHPB, a miniatured SHPB has much shorter specimen length.
- The other modification done is the absence of the input bar in the experimental setup (Fig 1.4). During the experiment the specimen is sandwitched between the output bar and the striker bar and the striker bar directly impacts on the specimen rather than striking the input bar (as in the conventional SHPB). Due to this modification the reflected strains are difficult to measure, however [13] addresses two ways through which the reflected strains can be measured:
    - The striker bar is presumed to be rigid as in [14].
    - The reflected strain can also be measured by determining the velocity on the non-impacting end of the striker bar as in [15].
- The third modification is to scale-down the components of the experimental setup. D Jia and KT Ramesh [16] developed a miniatured SHPB having a bar diameter of 3 mm and the length of the bars around 30 mm and were made up of either Tungsten Carbide or Maraging Steel.

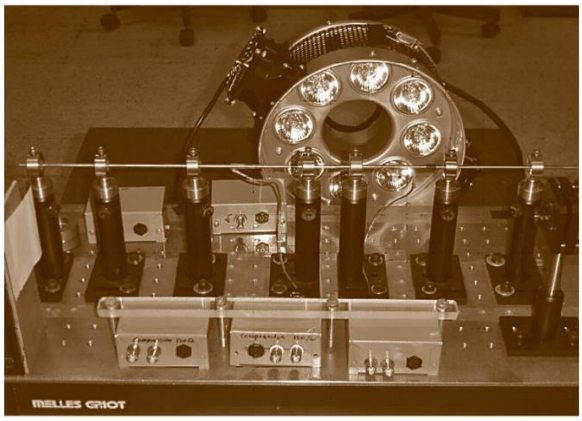

Fig 1.4: Miniatured SHPB Setup [13]

Apart from Aerospace, Biomedical and Chemical Sector Ti alloys are used very sporadically in other sectors due to their high processing costs. Singh *et al* [17] discuss the costs associated at every stage of component manufacturing involving Titanium Alloys (Fig 1.5). It is evident from it that the energy-intensive melting and fabrication procedures needed to create the finished products/goods from the available raw material account for about 60% of the total cost. Therefore, enhancing the processibility of Ti alloys which helps

in lowering the cost of the finished product significantly, thereby increasing their applicability across a variety of industrial fields.

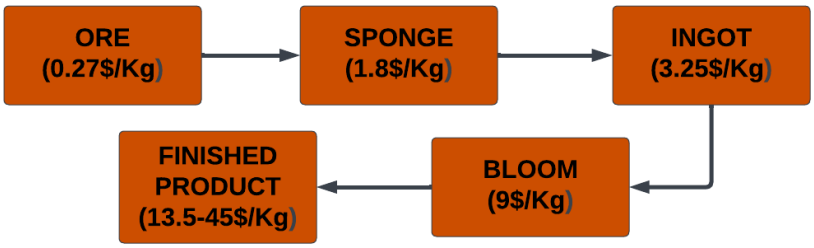

Fig 1.5: Costs associated at every step of component manufacturing involving Ti alloys [17]

Glavicic *et al* [18] reports the prior-β grain size to be of the order of millimetres. Several Thermo-Mechanical steps are required to bring down the grain size to be at the sub-millimetres or micron level. To facilitate this, Boron Modification comes into picture and it has recently been demonstrated that the as-cast grain size of Ti alloys is dramatically reduced by the addition of trace amounts of B. The number of Thermo-Mechanical processing steps might theoretically be decreased, if not entirely eliminated, which could result in significant cost reductions for producing Ti products. The microstructural improvements brought about by the addition of traces of B also help to enhance the mechanical characteristics. Combined, these advantages might significantly lower the price of titanium alloys.

1.2 Metallurgy of Titanium

1.2.1 Crystal Structure of Ti

Just like a variety of metals like Iron, Zirconium, Cobalt, and Tin many crystal forms can be observed when titanium crystallises. Each alteration, however, can only be maintained within a certain range of temperatures. Such a transition where the material changes its crystal structure completely after a particular value of temperature is known as an allotropic transformation and the temperature associated to it is known as the transus temperature.

CP Titanium (generally regarded as α Titanium) is present in a Hexagonal Closed Packed (hcp) Structure and as the temperature increases this hcp structure transforms into a Body Centred Cubic (bcc) structure also called as β Titanium. The transformation temperature is around 882±2°C and is called as the β-Transus Temperature. The hcp and bcc structures of Ti are schematically represented in Fig 1.6.

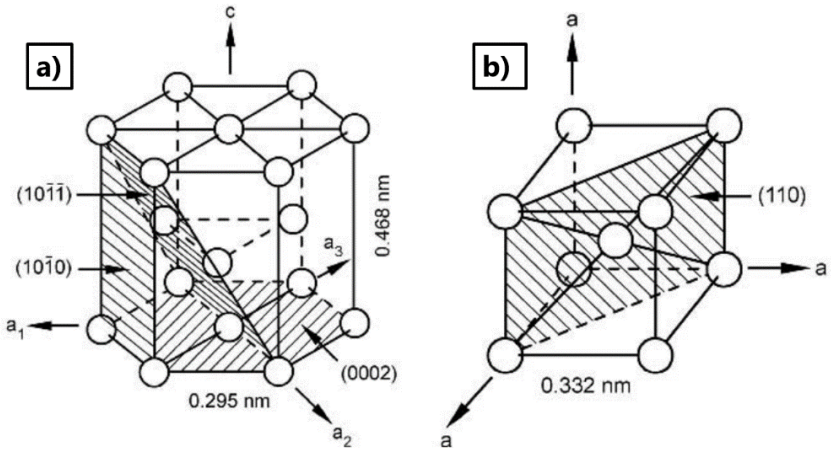

Fig 1.6: Crystal Structure of **a)** α-Titanium (hcp) and **b)** β-Titanium (bcc) [19]

Fig 1.6 (a) represents the c and a value (lattice parameter values) to be 0.468 nm and 0.295 nm respectively and the c/a ratio here comes out to be 1.5864 which is slightly less than the classic c/a ratio of 1.63 for a hcp structure and hence the α-Titanium is said to have a distorted hcp structure. The figure also represents the three planes which are the most densely packed ones:

- The Basal Plane (0002)
- A single Prismatic Plane $\{10\bar{1}0\}$ out of the three
- One out of the six $\{10\bar{1}1\}$ Pyramidal Plane

a_1, a_2 and a_3 basically represent the three closed pack directions denoted by $<11\bar{2}0>$.

Fig 1.6 (b) represents the crystal structure of β-Titanium (bcc). As the structure is cubic in nature there is only one lattice parameter and the value is around 0.332 nm. The family of the most densely packed planes (total 6 in number) is represented by {110} and a represents the closed pack directions <111>.

1.2.2 Plastic Deformation Characteristics

Table 1.1 shows the characteristic properties of the two crystal forms that exist in titanium. The ease of plastic deformation in a crystal lattice is basically governed by the following parameters:

- **The number of slip systems:** The number of SS is basically calculated by the product of Slip Planes and Slip Directions. The α-titanium having the hcp structure has 3 slip systems whereas the β-titanium having the bcc structure has 12 slip systems. Larger the number of slip systems – larger the chances of dislocation movement and due to this reason the α-titanium has less tendency to deform than the β-titanium.
- **The Energy required for plastic deformation:** The shortest slip path's length (denoted by $b_{min}.a$) has a direct impact on the energy required for plastic deformation. Table 1.1 clearly depicts that the minimum slip path distance for α-

titanium is 1 whereas for the β-titanium is $\frac{1}{2\sqrt{3}}$ (which comes around 0.87). As a result, we can draw the conclusion that the bcc structure is simpler to deform than the hcp.

Structure type	N	CN	Packing Density (%)	Slip Plane / Slip Direction	N_{planes} / $N_{directions}$	Slip system per unit cell	Atomic density of slip plane	b_{min}/a
hcp	6	12	74 %	{0001}	1	1*3 = 3	≈ 91 %	1
				<11$\bar{2}$0>	3			
bcc	2	8	68 %	{110}	6	6*2 = 12	≈ 83 %	0.87
				<111>	2			

Table 1.1: Typical characteristic features of different crystal structures of Ti [1]

One more explanation that clearly indicates the difficulty in the deformation of α-titanium is the Von-Mises Criterion. It says '**Metals need to possess a minimum of five independent ss to undergo uniform plastic deformation**' but in the case of hcp titanium there are a total of three ss each for the basal and prismatic planes. Out of these three only two are independent of each other bringing the total of 4 independent slip systems in α-titanium.

1.3 Titanium and its alloys

1.3.1 Alloying Elements

Titanium alloys are majorly classified into five main categories viz. α-alloys, Near- α alloys, α + β alloys, Near-β alloys and β-alloys. The alloying elements added to titanium are basically divided into three categories:

- **α-stabilizers:** The α-stabilizers tend to increase the β-transus temperature hence raising the temperature range of the alpha phase field (Fig 1.7 (b)). Both interstitial and substitutional alloying components are present in the α-stabilizers. The substitutional alloying elements include Aluminium, Gallium and Germanium and the interstitial ones include Oxygen, Carbon, and Nitrogen. The most widely used α-stabilizer is Aluminium due to its high solubility in both the phases (α and β) and it also helps in bringing down the density of the alloy formed. However, there is a certain limit up to which Al is added and it is around 5-6 % because excess Aluminium when added to Titanium gives rise to the formation of Ti_3Al phase in the alloy which makes the alloy brittle. The constancy of the α is influenced by the Al Equivalent:

$$[Al]_{eq} = Al + \frac{1}{3}Sn + \frac{1}{6}Zr + 10\,(O + C + N)$$

- **Neutral Stabilizers:** The Neutral Stabilizers have no or very less influence on the β-transus temperature (Fig 1.7 (a)). The elements that come under this category include Tin, Zirconium and Hafnium. According to some reports, adding Zr and Sn to titanium alloys can boost the stability of the β phase.

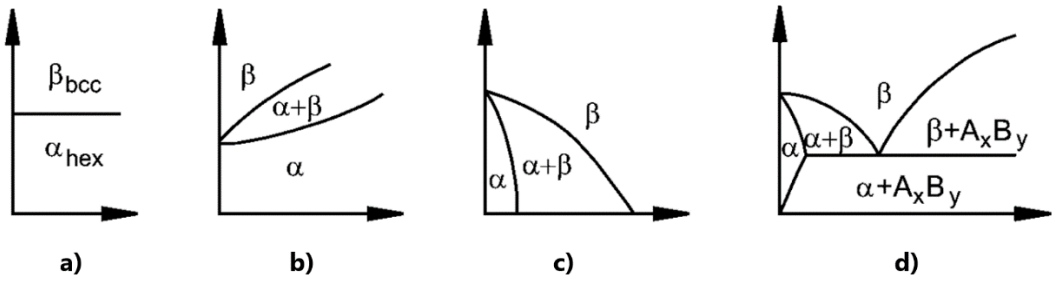

Fig 1.7: Effect of **a)** Neutral-Stabilizer **b)** α-stabilizer **c)** β-Isomorphous and **d)** β-Eutectoid Stabilizers on the phase diagram of Titanium [1]

- **β-Stabilizers:** The β-Stabilizers tend to decrease the β-Transus temperature thus stabilizing the β-Phase. β-Stabilizers are broadly classified into two categories viz. β-Isomorphous and β-Eutectoid. The β-Isomorphous category is more widely used as stabilizers due to their excellent solid solubility in Titanium (Fig 1.7 (c)). The elements that come under β-Isomorphous are Molybdenum, Vanadium and Tantalum. The less extensively used category the β-Eutectoid (Fig 1.7 (d)) include elements like Iron, Manganese, Chromium, Cobalt, and Nickle. These are used in very lower amounts due to their tendency to form inter-metallic compounds which can be detrimental for the alloy formed. For high temperature applications, Si is also frequently added to titanium alloys, and it can increase creep resistance. The stability of the is determined by the expression given by:

$$[Mo]_{eq} = Mo + 0.67V + 0.44W + 0.28Nb + 0.22Ta + 1.6Cr + 1.25Ni + 1.7Co + 2.9Fe$$

1.3.2 Classification of Titanium Alloys

Titanium Alloys are broadly classified into three main categories viz. the α-alloys, the α + β alloys and the β-alloys. They are two more subdivisions: the Near- α alloys and Near- β alloys (Fig 1.8). This classification is basically done on the wt % of β-stabilizer added.

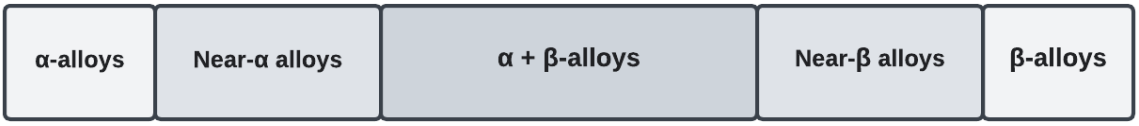

Fig 1.8: Classification of Titanium Alloys

- **α-alloys:** These alloys contain only a single phase (α-phase) and are made with the help of solid solution strengthening by the addition of α or neutral stabilizers. Alpha alloys are stable and have good high temperature qualities, however they cannot be heat treated to change their microstructural properties. Table 1.2 represent the different types of α-alloys commercially used along with their compositions and β-Transus temperature. The principal applications for α-alloys are in the chemical and process engineering fields, where resistance to corrosion and deformation are of utmost importance.

Common name	Alloy composition	$\beta_{transus}$
IMI260	Ti-0.2Pd	915 °C
CP-Ti (Grade 1)	Ti-0.2Fe-0.18O	890 °C
CP-Ti (Grade 2)	Ti-0.3Fe-0.25O	915 °C
CP-Ti (Grade 3)	Ti-0.3Fe-0.35O	920 °C
CP-Ti (Grade 4)	Ti-0.5Fe-0.4O	950 °C
TC-21	Ti-6Al-2Sn-2Zr-3Mo-1Cr-2Nb-Si	960 °C

Table 1.2: Some commercially used α-Titanium alloys along with their T_β [19], [20]

- **Near-α alloys:** β-Stabilizers are added to these alloys in the amounts ranging from 1 to 2 wt % in order to increase their workability and strength. These alloys, which offer a nice middle ground between high-strength α + β alloys and the excellent creep resistant α-alloys. These alloys are generally used in high temperature applications (jet engines). Table 1.3 represent some commercially used Near-α alloys along with their β-Transus temperatures.

Common name	Alloy composition	$\beta_{transus}$
Ti-5111	Ti-5Al-1Sn-1Zr-1V-0.8Mo	980 °C
IMI685	Ti-6Al-5Zr-0.5Mo-0.25Si	1025 °C
Ti-6242	Ti-6Al-2Sn-4Zr-2Mo-0.1Si	995 °C
Ti-1100	Ti-6Al-2.7Sn-4Zr-0.4Mo-0.45Si	1015 °C

Table 1.3: Some commercially used Near-α Ti alloys along with their T_β [21]–[24]

- **α + β alloys:** The amount of β-Stabilizer added to these alloys is slightly higher (4-6 wt %) than the Near-α alloys. Heat treatment of these metals can produce a range of microstructures and mechanical characteristics. Due to a good balance in properties these alloys are used in structural applications like Aircrafts, Ships and Bridges. Table 1.4 represent some common α + β alloys along with their composition and β-Transus temperatures.

Common name	Alloy composition	$\beta_{transus}$
Ti-64	Ti-6Al-4V	995 °C
Ti-662	Ti-6Al-6V-2Sn	945 °C
Ti-6246	Ti-6Al-2Sn-4Zr-6Mo	940 °C
Ti-17	Ti-5Al-2Sn-2Zr-4Mo-4Cr	890 °C

Table 1.4: Some commercially used α + β Ti alloys along with their T_β [21]

- **Near-β alloys:** Around 10-15 wt % of β-Stabilizers are present in these alloys. These alloys have excellent hardenability, forging properties, high strength, and toughness over a broad temperature range. As strengthening agents, these alloys contain trace quantities of α -stabilizing elements. At a specific strength level, β and near- β alloys offer greater fracture toughness than α + β alloys [25]. They are being used more frequently in structural aircraft uses. Table 1.5 represent some commercially used Near- β alloys along with their composition and β-Transus temperatures.

Common name	Alloy composition	$\beta_{transus}$
Ti-7333	Ti-7Mo-3Nb-3Cr-3Al	850 °C
Ti-55531	Ti-5Al-5Mo-5V-3Cr-1Zr	845 °C
Ti-55511	Ti-5Al-5Mo-5V-1Cr-1Fe	873 °C
Ti-1023	Ti-3Al-10V-2Fe	800 °C

Table 1.5: Some commercially used Near-β Ti alloys along with their T_β [26]–[29]

- **β-alloys:** Very large amounts of β-Stabilizers are added here (≈ 30 wt %). In their solution-treated state, titanium alloys typically have lower strengths. Yet, due to the precipitation of the fine α -phase during ageing, through the process of aging, these alloys can be conditioned to achieve exceedingly elevated levels of strength. By choosing the proper ageing temperature and duration, these alloys can be designed to have the ideal mix of strength and fracture toughness. With their high density and low ductility, β-alloys behave like refractory metals and are employed in a variety of highly specialised burn- and corrosion-resistant applications.

1.3.3 Properties of Titanium Alloys

This section basically covers the properties of different classes of Ti alloys. Based on their Mechanical, Physical, and technological characteristics, the three alloy classes α, α + β, and β are distinguished from one another in Table 1.6.

Property	α-alloys	α + β -alloys	β-alloys
Density	↑	↑	↓
Strength	↓	↑	↑↑
Ductility	↓/↑	↑	↑/↓
Fracture Toughness	↑	↓/↑	↑/↓
Creep Strength	↑	↑/↓	↓
Corrosion Behaviour	↑↑	↑	↑/↓
Oxidation Behaviour	↑↑	↑/↓	↓
Weldability	↑	↑/↓	↓
Cold Formability	↓↓	↓	↓/↑

Table 1.6: Property comparison of various classes of Ti alloys (Reproduced from [1])

The density of α-alloys is low as compared to its counterparts – the α + β, and β due to the fact that the most extensively used α-stabilizer is Al ($\rho \approx 2.7$ g/cm^3) whereas the β-stabilizers used for the α + β, and β alloys are Molybdenum and Vanadium having densities of 10.28 g/cm^3 and 6.1 g/cm^3 respectively.

α-alloys, being single-phase materials, typically only exhibit moderate strength. Nonetheless, it is possible to harden near- β alloys and the two-phase α + β alloy to extremely high and moderately high strength levels, respectively.

Metastable- β alloys must trade off their high strength levels for low ductility. They have reasonably strong ductility, comparable to that of α and α + β alloys, if not age-hardened. Also, the microstructure and ductility are closely connected.

There is no clear relationship between the various alloy classes because the fracture toughness of Ti alloys greatly depends on the microstructure and the ageing state. Particularly, compared to fine and equiaxed microstructures, the lamellar and coarse microstructures have higher fracture toughness values. The ability of lamellar microstructures to divert propagating cracks along variably orientated lamella packets helps to explain their high toughness. As a result, the fracture front profile becomes rough, requiring more energy to propagate the crack.

The primary factor causing α's superior creep behaviour is the relatively constrained capacity of atoms to disperse and crystals to get deformed in hcp lattices. Ti-alloys exhibit worsening creep behaviour as vol. fraction of β increases. Two-phase microstructures

having a non-continuous β distribution exhibit high creep resistance as well. This is primarily true for lamellar structures and to a lesser extent for bimodal structures.

The strong resistance to corrosive surroundings of Ti alloys is due to titanium's high affinity for oxygen, which causes a very thin and significantly dense oxide layer (TiO_2) to form even in air at ambient temperature. α is a more stable alloy class than β.

Titanium alloys' maximum working temperature is mostly affected by their comparatively poor oxidation behaviour rather than by a lack of appropriate strength. In this case, β is more prone to oxidize than α.

One problem with titanium alloys is that they are highly reactive with O_2 and H_2 present in the environment, which can weaken the alloy. This means that inert gas or a vacuum environment must be used for titanium alloy welding. β alloys can be more difficult to weld than α and α + β alloys, especially once the former has reached high strength levels via ageing.

It follows that α and α + β alloys can be contorted at soaring temperatures because the α phase has a more limited capacity for deformation and a stronger capacity for work hardening. When the β volume percentage rises, the deformation temperature falls, and in some near-β alloys, deformation is possible even at room temperature. A small, equiaxed microstructure encased in an ongoing β phase is necessary for super-plastic deformation.

1.3.4 Commercially used Titanium Alloys

With a nearly 30% decrease in the cost of CP-Ti over the past five years, titanium, and especially titanium alloys, have become more affordable. Titanium alloys play a vital role as an essential material in a wide range of civil and military applications spanning various fields such as energy, transportation, medical (for observing the human body using MRI magnets), water treatment, and the transportation of corrosive liquids and gases. These benefits comprise reduced weight, favourable mechanical characteristics, resilience to extremely low temperatures, resistance to electro-chemical corrosion, and compatibility with biological systems. Fig 1.9 represents the distribution of usage of Ti alloys in various sectors in the Western market (Data is up till 2017).

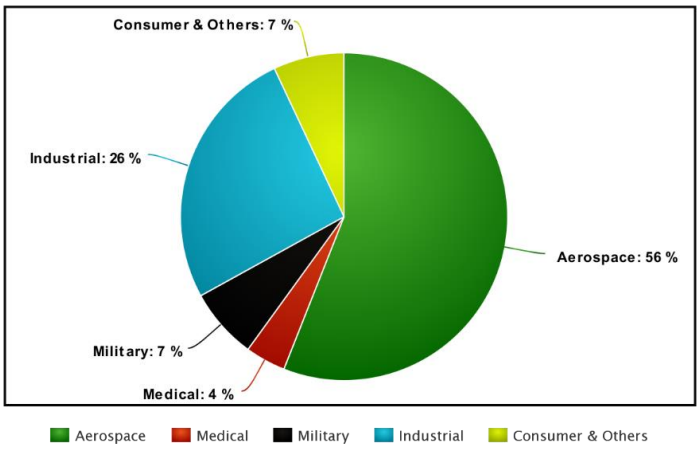

Fig 1.9: Applications of titanium in the West, broken down by market (Till 2017) [30]

The major Ti alloys used in the different sectors mentioned in Fig 1.9 are briefly explained in the subsequent sections.

1.3.4.1 Titanium in the Aerospace Industry

The following are the main defences for employing titanium in the aircraft sector:

- **Weight Reduction** (So that it can be used as a replacement of Steel)
- **Space Restrictions** (Can be used as a replacement for Aluminium)
- **Temperature of Operation** (Thus can replace Aluminium and Nickle)
- **Resistance to Corrosion** (Can act as a replacement for Aluminium and low alloy Steels)
- **Compliance with Composites** (Thus can act as a replacement for Aluminium alloys)

R.R. Boyer [31] provides a great description of the many Ti alloy classes and the applications for each in the aerospace industry:

➢ α-alloys

- The most commonly used α-alloy (**CP-Ti**) after annealing is used in environment control systems that run at temperatures up to roughly 230°C which is excessive for alloys made of aluminium, ducting for anti-icing, tubes or pipes in the bathroom system, clips and brackets, and floor support structures in the galley and restroom areas.
- The alloy **Ti-3Al-2.5V** is used as an active alternative for 21Cr-6Ni-9Mn Stainless Steel as it helps in reducing the weight of high-pressure hydraulic lines by about 40 %. In situations where more strength is needed than CP-Ti can offer, it is also employed to create honeycomb cores.
- In their 1978 publication Van Stone *et al* [32] carried out quasi-static fracture tests on the α-alloy **Ti-5Al-2.5Sn** at cryo temperatures of 20K and 77K and it retained good K_{IC} and ductility values even at those temperatures and hence it is predominantly employed on the hydrogen-facing side of the high-pressure fuel turbo-pump utilized in the space shuttle.
- Another α-alloy **Ti-8Al-1Mo-1V** (when duplex annealed) is used for rip straps and fan blades in military engines as well as fan blades in commercial airframes.

➢ Near-α alloys

- The most widely used near-α alloy **Ti-6Al-2Sn-4Zr-2Mo** (Ti-6242) because it's both lightweight and resistant to high temperatures and is used at temperatures where the famous Ti-6Al-4V alloy becomes inoperable (around 315 °C) for structural applications. It is also used in area involving high pressures like Compressors.

- Rolls-Royce (RR) manufactures engines for aircrafts and uses two newly developed near-α alloys (IMI 829 and IMI 834). The **IMI 829** (Ti-5.5A1-3.5Sn-3Zr-1Nb-0.25Mo-0.3Si) is used in areas like spacers and blades of engines and also for the discs used in compressors where the temperatures rise up to 550 °C [33]. The other alloy **IMI 834** (Ti-5.8Al-4Sn-3.5Zr-0.7Nb-0.5Mo-0.35Si-0.06C) is used in the discs of compressors (Both the first 4 stages of the high-pressure compressor and the final 2 stages of the intermediate pressure compressors).

➢ α + β alloys

- The **Ti-6Al-4V** alloy makes up around 60% of all titanium production, is the pillar of this sector. It possesses excellent fatigue and fracture characteristics (which can be optimised through heat treatment), is a forgiving alloy to work with, and is used in all product forms, including forgings, bars, castings, foil, sheets, and plates as well as extrusions, tubing, and fasteners. It is typically used at a minimum tensile strength of 896 MPa. Other applications include floor support structure, like places for galleys and restrooms and other portions of the aircraft, including the fuselage, nacelles (Fig 1.10 (a)), landing gear (Fig 1.10 (b)), wing, and empennage (Fig 1.10 (c)).

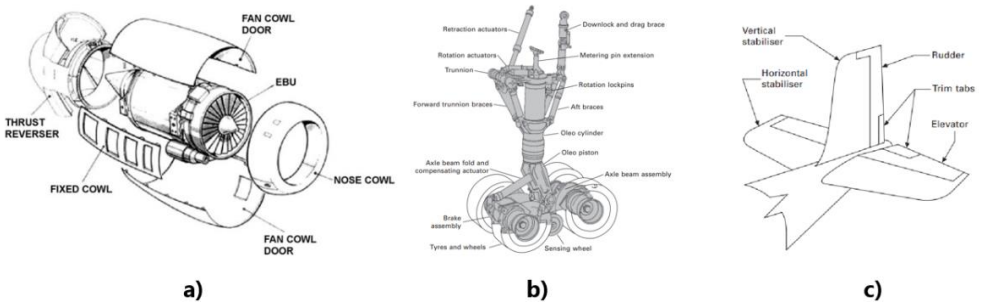

Fig 1.10: Applications of Ti-6Al-4V in **(a)** Nacelles [34] **(b)** Landing Gear [35] **(c)** Empennage [35]

- The **Ti-662** alloy (Ti-6Al-6V-2Sn) is utilised for the same purposes as Ti-64 and would result in greater weight reductions, although the fracture toughness is compromised to an extent. Due to its greater corrosion resistance to low alloy steels and its ability to reduce weight in applications like drag braces, bell cranks and torsion links, it was widely employed in the landing gear support structure of the 747.
- **Ti-6-22-22** (Ti-6Al-2Sn-2Zr-2Mo-2Cr) created by RMI in the early 70s as a deep hardenable alloy. For the Lockheed/Boeing F-22 programme, it has lately been revived as a moderate strength-damage tolerant alloy.

- **Near-β alloys**

    - **Ti-B 120 VCA** (Ti-13V-11Cr-3Al) was the first Ti alloy in β/Near-β regime to be used commercially [1]. In essence, the whole main and nose landing gear as well as wing and body coverings, frames, ribs, bulkheads, longerons and rivets were made of it. Titanium was utilised because it was light and could withstand high temperatures while still meeting mission criteria. The thermal stability of Ti-13-11-3 was one of the main factors in its choice.
    - Other Near-β alloys include **Ti-1-8-5** (Ti-1Al-8V-5Fe) – used in fasteners, **VT 35** (Ti-15V-3Cr-1Mo-0.5Nb-3Al-3Sn-0.5Zr) serves as a high strength alloy for the casting used in airframe structures.

- **β-alloys**

    - **Alloy C** (Ti-35V-15Cr, Ti-40Mo, Ti-30Mo) is one of the β-alloy which is used due to its strong ignition resistance, this alloy can now be used in applications that previously required Ni-based alloys, such as the cast compressor components and vectored exhaust structure on the FI-19 engine that powers Boeing F-22 aircraft.
    - Stall Strips of aircrafts (Fig 1.11) are primarily made up of the **Ti-15-3** (Ti-15V-3Cr-3Sn-3Al). The ability to produce strips from this alloy, cold shape it, and heat treat it to high strengths are its benefits. Ti-15-3 may be easily brake-formed or formed into rectangular, round, or oval shapes thanks to its good cold forming properties.
    - The 777's main landing gear is almost entirely made of **Ti-10-2-3** (Ti-10V-2Fe-3Al), which reduces the weight of each aeroplane by around 270 kg and does away with the risk of stress corrosion cracking that comes with using steel.

1.3.4.2 Titanium in the Biomedical Industry

Biomaterials must adhere to the following standards:

- Resistance to Corrosion
- Biocompatible
- Osseointegratable: The scientific word for bone ingrowth into a metal implant is osseointegration. An artificial implant is surgically anchored and incorporated into bone, where it becomes permanently integrated. The most frequent applications of osseointegration are in joint replacement surgery and dental implants.
- Favourable mechanical characteristics, such as a Young's modulus (E) that is comparable to bone and fatigue strength depending on the application.
- Processability (welding, brazing, machinability, powder metallurgy, deformation, casting, etc.)
- Economical

The most widely used alloying elements used with Ti for biomedical purposes are Niobium, Molybdenum, Tantalum and Zirconium. These alloys have excellent biocompatibility in addition to having a high percentage of β stabilizing elements, which causes them to have a lower elasticity modulus than α + β alloys. Since they are more closely suited according to the modulus of a human bone, low modulus values are favourable for usage in implants (about 35 GPa). As Ti alloys naturally osseointegrate, they can be used to create implants that stay in place for longer. As titanium is not magnetic, it is safe to use magnetic resonance imaging to securely check patients with titanium implants, making it an advantageous choice for long-term implants.

Akinwamide *et al* [36] mentioned some of the major biomedical titanium alloys along with their application areas:

- **Ti-12Mo-6Zr-2Fe** [37]: Due to its exceptional biocompatibility and corrosion resistance, TMZF alloy (also known as Ti-12Mo-6Zr-2Fe) has been employed as a femoral stem in complete hip replacements since the early 2000s. Nevertheless, producing TMZF alloy via traditional techniques like casting, forging, and wroughting is expensive and time-consuming, and it can be difficult to machine the resulting complex-structured biomedical implant.
- Other Ti-alloys along with their applications are mentioned below:
    - **Ti-35Nb-7Zr-5Ta** is used for dental implant purposes [38]
    - **Ti-29Nb-13Ta-4.6Zr** is used for artificial knee joints [39], [40]
    - **Ti-24Nb-4Zr-8Sn** is used for Spine joints and bone plates [41]

1.3.4.3 Titanium in the Automobile Industry

Although the considerable interest the industry has shown in titanium materials in terms of their lightweight nature, fuel efficient characteristics, and performances, the applications of Ti alloys to the automotive industry have been restricted to racing cars and special-purpose automobiles due to their high cost.

Fujii *et al* [42] discussed how Ti and its alloys are now often utilised for numerous components of mass-produced cars:

- As a result of stricter requirements for lightweight components, global warming can be prevented by lowering carbon dioxide emissions.
- The development of technologies to produce inexpensive titanium has advanced remarkably.
- The public has grown to appreciate titanium's distinctive appearance and modernity.

Fujii *et al* [42] also highlighted the advantages one could get if an automotive company uses Ti alloys instead of their counterparts:

- Considering that components such as exhaust valves are subjected to temperatures exceeding 400 °C while in contact with exhaust gas, titanium emerges as the most suitable material for achieving weight reduction, thanks to its superior specific strength compared to steel, as well as its superior heat resistance when compared to aluminium. For instance, a study showed that switching from steel to titanium can lower the weight of a 2-wheeler by around 3 kg and a 4-wheeler vehicle by about 8 kg.
- They [42] also reported that Ti exhibits half the value of Standardized Stress (the product of α and E) as compared to Ferritic Steels and hence the former performs better than the latter in terms of their fatigue properties.
- The materials used for automotive parts must also be cold workable because they are produced using a variety of forming processes, including cold press, or bending. In this regard, titanium may completely meet the aforementioned standards.
- In addition to performing the aforementioned tasks, titanium must also exude youth and style, especially when used as a muffler (a component whose design is focused on the exterior of an automobile, making it a key selling feature). Also welcomed in the market are the unique surface appearances of titanium that cannot be found in other metals. It also has a distinctive exhaust sound that is its unique feature and not present in steel, which draws attention from the public in addition to the many interference colour changes that occur on its surface when it is employed.

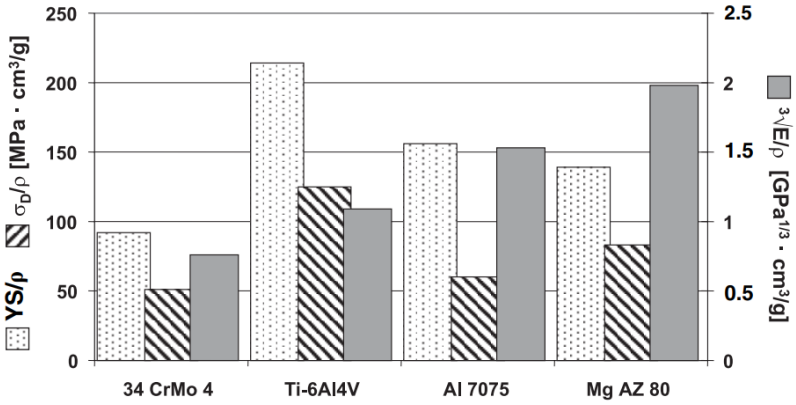

Fig 1.11: Comparison of Properties (Specific) [1] [YS, FS and E] of **34CrMo4** (A type of forging steel), **Ti-6Al-4V** (an α + β titanium alloy), **Al-7075** (a type of high strength Al alloy), **MgAZ80** (a type of high strength Mg alloy)

In terms of achieving optimal strength or fatigue resistance for structural components, titanium alloys unequivocally outperform other metallic materials. However, given its relatively low E, which is evident in the grey columns (Fig 1.11), titanium is less suitable for structural components that must be built for optimal rigidity. Aluminium or Magnesium are excellent materials to use in this situation to achieve lightweight construction. Potential uses for titanium are mostly found in the chassis and engine because the body is built for maximum torsional and bending stiffness.

Following are the major Ti alloys used by different car manufactures [1]:

- Mercedes-Benz uses the **Grade 2 CP-Ti** for the guide pins of the brakes of the S-Class models
- For all of its models Volkswagen uses **Grade 1 CP Ti** for their Sealing Washers. Honda also used the same Ti alloy for the gear shifting knob of the S2000 Roadmaster ® models.
- The connecting rods of the Porsche GT-3® were made of the most famous α + β alloy: **Ti-6Al-4V**. Turbocharger rotors of the diesel truck manufactured by Mercedes-Benz were also made using **Ti-6Al-4V**. The engine inlets of the CMIA® by Nissan used **Ti-6Al-4V**.
- Toyota used **PMd Ti-6Al-4V** for the valves of the Altezza® models.
- G Luterjing and J.C. Williams [19] also discuss the use of **Ti METAL LCB** (Ti-6.8Mo-4.5Fe-1.5Al) in their book. Volkswagen LUPO's® suspension springs were made using this alloy.
- The Gallant 1® model of the Mitsubishi Motors used **Ti-22V-4Al** for its engine retainers [21]. The turbocharger's rotor head in the LANCER® model by Mitsubishi uses the **γ-TiAl** inter-metallic.
- Nissan in one of its models (The CIMA®**)** used **Ti-6Al-2Sn-4Zr-2Mo-Si** alloy for its exhaust valves.

1.4 Microstructure of the α + β alloy

By altering the thermo-mechanical processing pathways, three distinct types of microstructures can be produced in α + β alloys, which are listed below:

- Fully Lamellar
- Fully Equi-axed
- Bi-modal microstructure (which contains equi-axed α_P [primary α] in the lamellar matrix of α + β)

1.4.1 Fully-Lamellar Microstructure

With the help of annealing in the β phase field, lamellar microstructures can be produced quite quickly during the last stages of the processing procedure (Stage III i.e., the Recrystallization Step). Fig 1.12 depicts the processing steps required to obtain a lamellar microstructure.

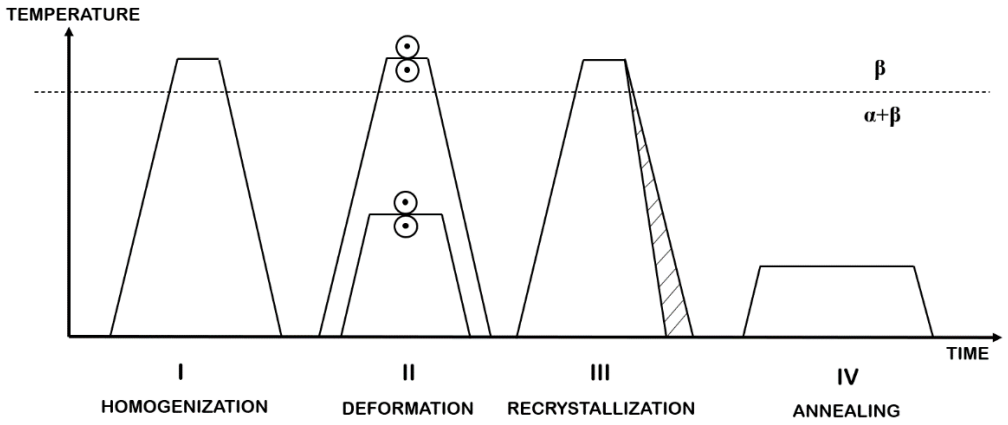

Fig 1.12: Lamellar Microstructure processing steps (Reproduced using [19])

Forging or rolling can be used to perform the deformation process (step II), either in the β-phase region or in the α + β-phase region. Due to the lower flow stress in the β-phase region, the material is typically first deformed there before being deformed in the α + β-phase region to prevent the formation of large sized β grains. In order to maintain control over the β grain size, step III's recrystallization temperature is often maintained between 30 and 50 °C above the β-transus. The β grain size of completely lamellar microstructures is hence generally 600 μm.

Step-III (Cooling Rate) in Fig 1.12 is the most important step as it governs the size of the α-lamellae, the size of the α-colony and also the α layer thickness at the GBs. G. Lütgering [43] also in one of his publications support that Cooling Rate is one more defining factor which decides the size of the α-lamellas. Fig 1.13 represents the microstructures at different cooling rates for the Ti-6242 α + β-alloy. Fig 1.13 (a) represents the microstructure at a

cooling rate of 1°C/min [Furnace Cooling], Fig 1.13 (b) is at 100 °C/min and Fig 1.13 (c) is at 8000 °C/min [Water Quenching].

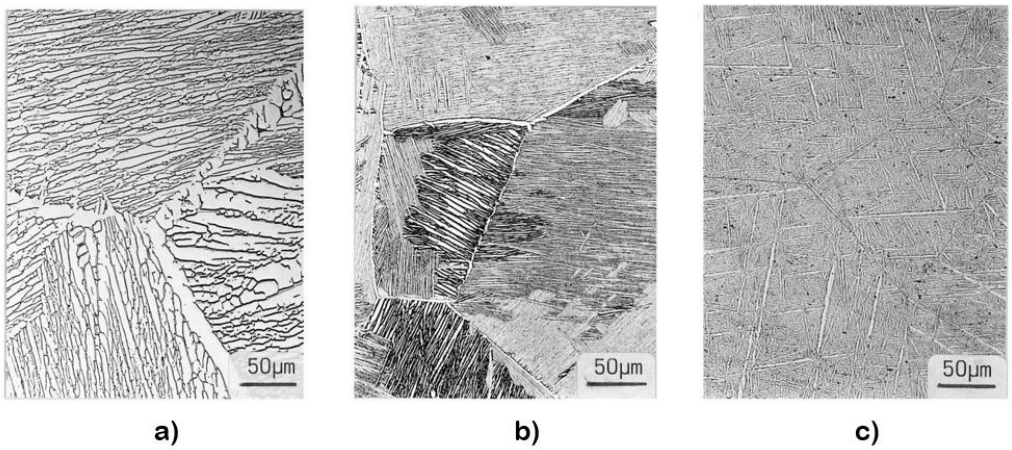

Fig 1.13: Effect of Cooling Rate (a) 1°C/min (b) 100 °C/min and (c) 8000 °C/min on the microstructure of Ti-6242 α + β-alloy [43]

All three of the aforementioned microstructural characteristics have been observed to decline with an increase in cooling rate. But the features: size of the α-lamellae and the size of the α-colony change differently at varying cooling rates. This is evident from the experiments performed by G. Lütgering [43] where he observed that the size of α decreased from 5 µm (1°C/min) to 0.5 µm at a cooling rate of 100°C/min (Fig 1.14)

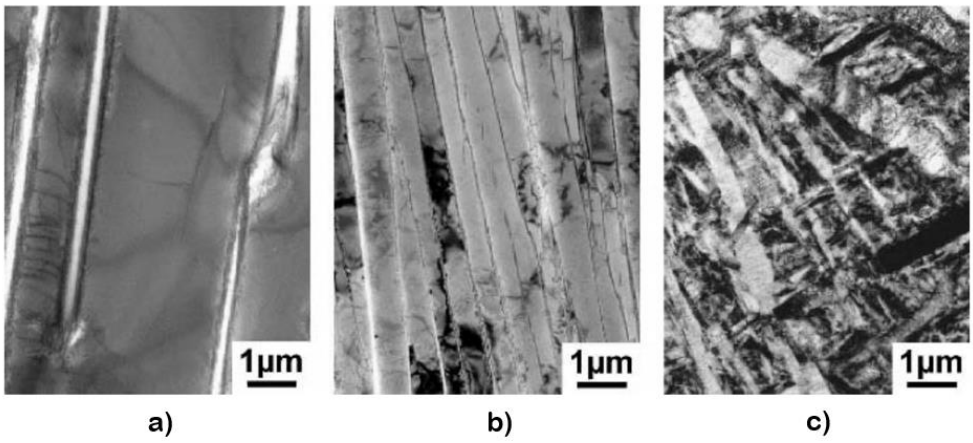

Fig 1.14: Effect of Cooling Rate (a) 1°C/min (b) 100 °C/min and (c) 8000 °C/min on the α-plate width [19]

Although a further increase in cooling rate only causes the average martensite plate width to decrease to about 0.2 µm, with some noticeably thicker martensite plates still present in the microstructure (See Fig 1.14 (c)). A cooling rate of 100°C/min causes the α colony size to be as large as half the size of the β grain in slowly cooled material, e.g., about 300 µm, to reduce to only slightly about 100 µm. (Fig. 1.13 (b)). Hence, between 100°C/min and 8000°C/min, if we compare the width of discrete martensite plates, a significant fall in colony size occurs.

1.4.2 Bi-Modal Microstructure

Fig 1.15 represents the steps required to achieve a Bi-Modal (Duplex) type of microstructure. As cooling rate is responsible for the size differences of the α-lamellae, in order to achieve this microstructure, the cooling rate after achieving the homogenization temperature is a critical characteristic here also.

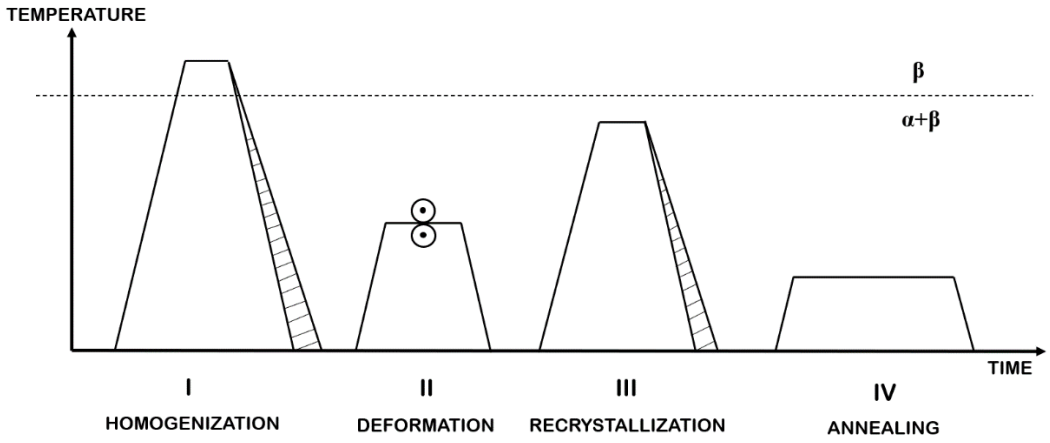

Fig 1.15: Bi-Modal Microstructure processing steps (Reproduced using [19])

G Lütjering [19] also compared two bi-modal microstructures (Fig 1.16) of the α + β-alloy IMI834 by varying the cooling rates after achieving the homogenization temperature and observing the changes in the α-lamellae obtained.

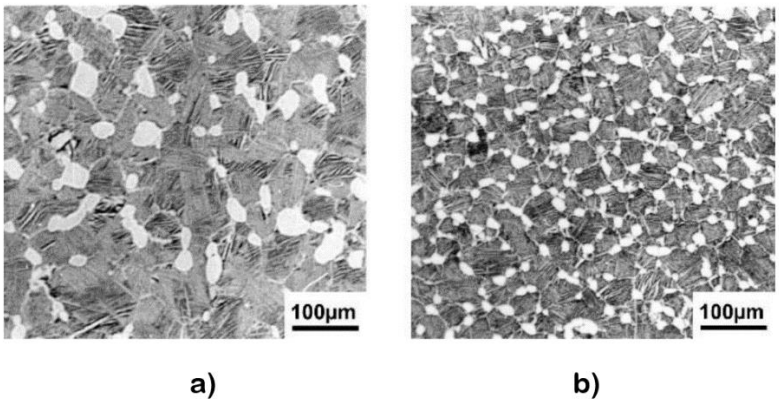

Fig 1.16: Variation of the α-lamellae size with **(a)** at slower cooling rate **(b)** faster cooling rate [19]

The lamellar structure is plastically distorted in step II i.e., the deformation step in the α + β region. In step III, the α and β phases must completely recrystallize, therefore the plastic

deformation should be as high as it can be while still being high enough to retain energy while introducing enough dislocations.

G Lütjering [19] also defines the important process parameters and their influence on the bi-modal microstructure of the α + β-alloys. These parameters are listed below:

- Cooling rate in step-I defines the size of the α-lamellae.
- Deformation in the α + β region (Step-II) governs the texture intensity and dislocation density.
- The annealing temperature in step-III governs the volume fraction of primary α.

1.4.3 Equi-axed Microstructure

To achieve a fully equiaxed microstructure, two options exist:

- Up to step III, where recrystallization takes place, the first option's processing path is the same as the path taken to generate a bi-modal microstructure (Fig 1.15). The only difference is that of the cooling rate in step IV i.e., if the cooling rate is slow enough so that no α-lamellae occurs in the β-grains and only the growth of α_P is possible then one can achieve a equi-axed type of microstructure.
- The second option for obtaining a fully equiaxed microstructure is to recrystallize in step III of the processing route (Fig 1.17) at such a low temperature that the equilibrium volume fraction of α phase at that temperature is high enough to generate the fully equi-axed microstructures directly from the distorted lamellar structures during the recrystallization step.

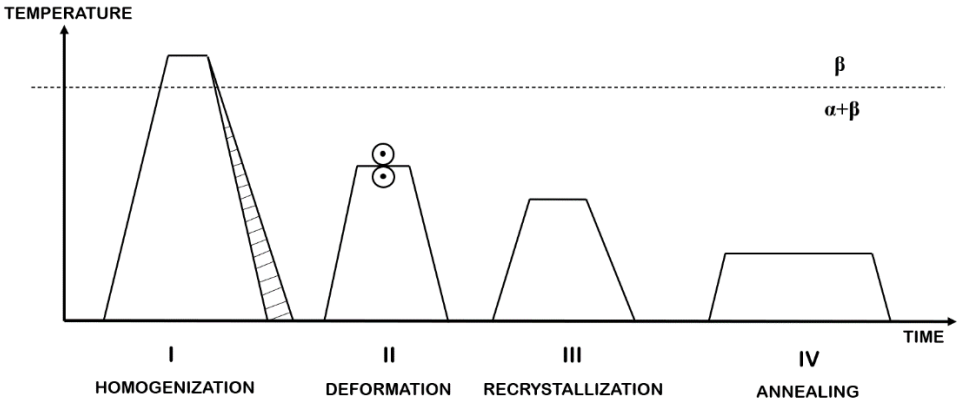

Fig 1.17: Equi-axed Microstructure processing steps (Reproduced using [19])

1.4.4 Property variation for different microstructures of α + β-alloys

The characteristics of titanium alloys are greatly influenced by the microstructure. Table 1.7 illustrates qualitatively the influence of phase size (comparison of coarse and fine types of microstructures) and phase arrangement (comparison of lamellar and equiaxed microstructures) on a number of significant selected mechanical parameters.

Fine	Coarse	Property	Lamellar	Equiaxed
○	○	Elastic Modulus	○	↑/↓
↑	↓	Strength	↓	↑
↑	↓	Ductility	↓	↑
↓	↑	Fracture Toughness	↑	↓
↑	↓	Fatigue Crack Propagation	↓	↑
↓	↑	Creep Strength	↑	↓
↑	↓	Super-plasticity	↓	↑
↑	↓	Oxidation Behaviour	↑	↓

Table 1.7: Influence of titanium alloy microstructure on specific characteristics [1]

The different microstructures significantly affect how the titanium alloys behave mechanically. Both ductility and strength are increased by fine-scale microstructures. They also hinder the formation of cracks and are necessary for profound plastic deformation. On the other hand, coarse microstructures are more resilient to creep and fatigue fracture development. Lamellar microstructures have high K_{Ic} values and exhibit superior resistance to creep and fatigue crack propagation, but equiaxed microstructures frequently have excellent ductility as well as fatigue strength and are favoured for profound plastic deformation. Bimodal microstructures have a balanced property profile because they mix the benefits of both the lamellar and equi-axed microstructures.

1.5 Deformation modes of Titanium

Different classes of Ti alloys have a predominant deformation mode according to the characteristics they possess. For ex, because of the generation of twinning in addition to the more typical slip caused by dislocations, the hcp-α titanium exhibits ductile behaviour, particularly at low temperatures. In general CP-Ti and other α-alloy deform using the twinning mode. On the other hand, twinning is almost totally suppressed in two phase α + β-alloys due to their tiny phase dimensions, high solute percentage, and the existence of Ti_3Al precipitates, these alloys are very ductile at low temperatures.

When talking about β-alloys in addition to slip, the bcc β phase also exhibits twinning, but twinning in β alloys only occurs in the single-phase condition and becomes less common with increasing solute load. Twining may take place in certain alloys during the forming processes before ageing.

1.5.1 Slip mode of deformation

The different slip planes and directions for the hcp Ti are shown in Fig 1.18. The slip directions are of the family <11$\bar{2}$0>. The slip planes corresponding to this slip direction are three (0002), three {10$\bar{1}$0} and six {10$\bar{1}$1} planes which brings the total at 12 slip systems. But the independent slip systems out of the three (0002), three {10$\bar{1}$0} and six {10$\bar{1}$1} are 2, 2 and 4 respectively now bringing the total of independent slip systems to be 8. The shape changes brought about by the combined effect of (0002) and {10$\bar{1}$0} families are identical to those brought about by the {10$\bar{1}$1} family, hence this number is further dropped to merely 4 independent slip systems.

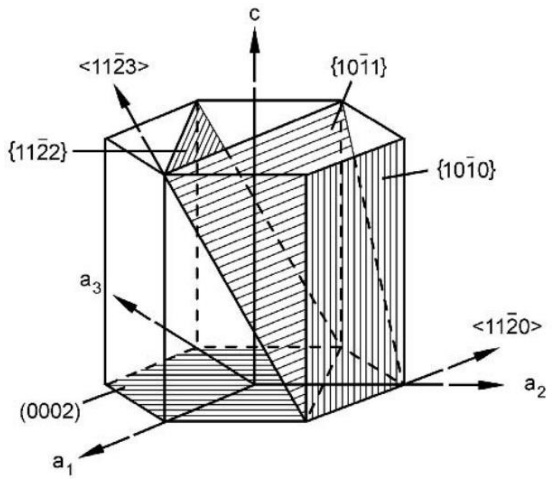

Fig 1.18: Slip planes and directions for hcp-titanium [19]

According to the criterion for homogenous plastic deformation given by Von-Mises there has to be at least 5 independent slip systems therefore one of the non-basal Burger's vectors must be activated, either the $\vec{c}$ type with the slip direction [0001] or the $\vec{c} + \vec{a}$ type with the slip direction of <11$\bar{2}$3>. TEM observations of some of the Ti-alloys depict the presence of the $\vec{c} + \vec{a}$ type of the Burger vector.

1.5.2 Deformation due to twinning

When the material exhibits very low temperature deformation, high purity, or coarse grain size, twinning mode is preferred over slip. When a significant quantity of elastic energy is injected into the system, above the critical value of the shear stress, twinning is advantageous. The mobility of atoms becomes negligible because of twinning. The {1102} is the most common plane for the twinning mode of deformation.

Depending on the circumstances, a certain deformation method may be preferred. As temperature changes during the hcp phase, the number of twin systems grows. Moreover, the favoured mode is influenced by strain rate. Twining is the preferred method of deformation when strain rates are large.

1.6 Deformation mechanism of Ti-6Al-4V at high strain rates

Alaghmandfard *et al* [44] carried out experiments on electron beam melted Ti64 at high strain rates ($1150s^{-1}$, $1500s^{-1}$, $1650s^{-1}$, $1900s^{-1}$, $2100s^{-1}$, $2700s^{-1}$) to study the deformation characteristics of Ti64 at such strain rates. They discovered that **Adiabatic Shear Bands** (ASBs) were developed at each of the strain rates mentioned above as evidenced by the distorted microstructures of all specimens. According to Nemat-Nasser [45] around 90% of the projectile's kinetic energy is transferred to thermal energy when the alloy is subjected to impact loading, raising the temperature of the tested specimen. As a result, a material that has been subjected to such impact loading encounters both the effect of strain hardening due to plastic deformation and the thermal softening effect due to the material's increased temperature.

Whenever material undergoes high-strain rate deformation the stress induced in the material can either increase or decrease depending on the fact that out of the two effects (strain hardening and thermal softening) which one is dominating. Meyers *et al* [46] observed the shear band using TEM and found out that the ASB's interior lacks features, which could be the result of softening events like dynamic recovery.

By creating voids, shear stress localisation in ASBs speeds up the failure mechanisms. The regions of ASBs soften during the thermal softening, reducing the energy needed for void nucleation. When any microstructural flaws are present, flow localization also quickens. Hence, the deformation/failure mechanism in Ti-6Al-4V is summarised in the following steps:

- **Void-Nucleation**: Tensile stresses when applied in the regions of ASBs during deformation caused by high strain rate compression, results in the production of micro-voids, which are often elliptical or circular in shape (Fig 1.19 (a)).
- **Void-Growth**: When these nucleated voids in the ASBs approach the border regions, where the strength of the material being deformed is different due to the significantly lower temperature than the temperature rise in the Adiabatic Shear Bands, they expand and lengthen along the it in the direction of shear stress (Fig 1.19 (b)).

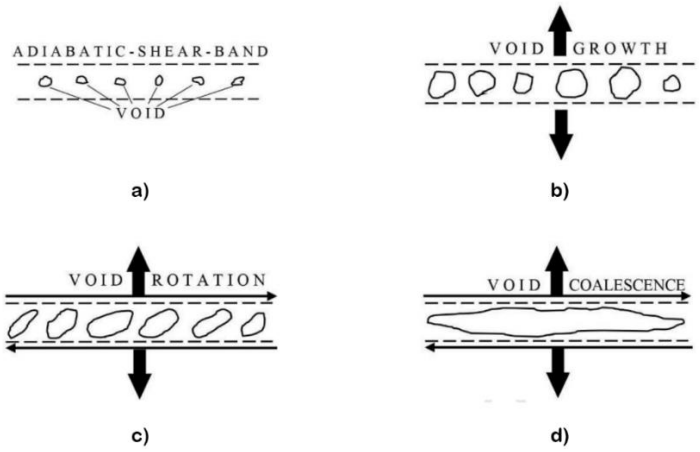

Fig 1.19: Deformation mechanism steps **(a)** Void Nucleation **(b)** Void-Growth **(c)** Void-Rotation and **(d)** Void-Coalescence for Ti-6Al-4V [44]

- **Void-Rotation and Coalescence:** As vacancies reach a large enough size, rotation happens (Fig 1.19 (c)) as a result of the continuing deformation, which causes the voids to merge (Fig 1.19 (d)) and start a crack. Initiated cracks spread under the impact of tensile stress at the time of unloading or shear stress during dynamic compression loading, which finally causes fragmentation of the specimens at greater strain rates. and the test specimens experience failure when being subjected to such impact loads.

1.7 Boron addition to Ti-6Al-4V

1.7.1 Literature review of the studies done on boron modification

The practice of boron addition to Ti alloys has been the recipient of an abundance of investigations going back to the 1950s, with the goal of enhancing the stiffness and strength. According to studies done by Glavicic *et al* [18] the microstructure of Ti-64 consists of β-grains that have the size of the order of a few millimetres. Singh *et al* [17] emphasised the need for certain thermo-mechanical processes to bring down the β particle size to micron scales. Recently, it has been demonstrated that the grain size if as-cast titanium alloys can be reduced by an order of magnitude by the addition of tiny amounts of B (up to 0.1 wt%). The number of thermo-mechanical processing steps might theoretically be decreased, if not entirely eliminated, which could result in significant cost reductions when producing Ti products. The microstructural improvements brought about by boron addition are also advantageous for enhancing mechanical characteristics.

Kamiya *et al* [47] investigated how the microstructure and tensile characteristics of as-cast Ti alloys used for dental applications were affected by trace additions of B (0.57 wt%). They also saw a notable refinement in the microstructure of Ti alloys due to B addition. The materials studied in this study included Pure Ti, Titanium-Silicon alloy (Ti-0.5Si) and Ti-6Al-4V. The composition of Boron added to the aforementioned materials were as follows:

- **Pure-Ti-xB** (x = 0, 0.008, 0.011, 0.025, 0.048, 0.086, 0.41, 1.02 wt %)
- **Ti-0.5Si-xB** (x = 0, 0.12, 0.46 wt %)
- **Ti-6Al-4V-xB** (x = 0.016, 0.04, 0.12, 0.48 wt %)

After reviewing the microstructures, they reported that although the boron concentration is relatively low, ranging from 0.011 to 0.048 wt %, some needle-shaped TiB particles are randomly distributed throughout the titanium matrix. The majority portion of boron is converted into TiB after interacting with Ti, indicating that titanium has a very poor solubility of boron. As the boron level exceeds 0.086 mass%, needle-shaped TiB particles with a length of 5 to 40 micrometres form along the boundary of earlier β grains. When the boron content rises, so do the TiB volume fraction. The variation reported in the mechanical properties were as follows:

- According to the observations reported by [47], adding boron caused a significant rise in each alloy's elongation. The peak value of Δl (elongation) was attained at a boron concentration of between 0.086 and 0.15 wt%, which is two times higher than that of titanium and its alloys in the absence of boron. As the B wt % keeps rising, a noticeable decrease in tensile ductility is then observed.
- They also reported that when the boron level rises, so does the titanium alloys' hardness.
- The tensile strength of each alloy increases up to a certain boron wt % (≈ 0.011 wt %) and then slowly dips. They described the TiB particles' stiffness, grain refining qualities and dispersion strengthening to be responsible for this behaviour.

But some of the most ground-breaking work in the field of Boron modification in titanium alloys is done by S. Tamirisakandala [48]–[52].

1.7.2 The Ti-B phase diagram

Fig 1.20 represents the Ti-B equilibrium phase diagram up till 50 at. % of Boron. In Titanium' liquid phase, B is totally soluble. But, on the other hand the solid solubility is ≈ 0.02 wt % in the solid α or β phases. It has been reported by Feng *et al* [53] and Ravi Chandran *et al* [54] that the amount of Boron added above the solid-solubility limit leads to the formation of TiB, which is actually an inter-metallic compound having the orthorhombic crystal structure (Fig 1.21). TiB manifests as truncated whiskers exhibiting a needle-shaped morphology.

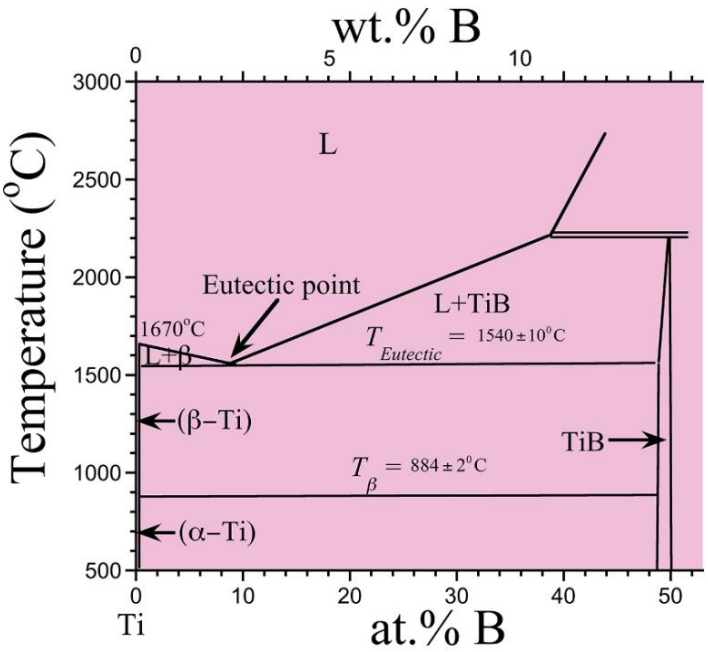

Fig 1.20: The Ti-B phase diagram [17]

Depending on the boron concentration, the binary Ti-B alloy system can be categorised as hypo-eutectic, eutectic, or hyper-eutectic. According to Tamirisakandala *et al* [55] the Ti-

alloys are regarded as Boron-modified when the Boron content in the Ti alloy does not exceed the eutectic limit i.e., when the concentration of Boron in the alloy is less than 1.55 wt %. The boron-modified alloys are identical to those without B in terms of microstructure, processing feedback, and mechanical characteristics.

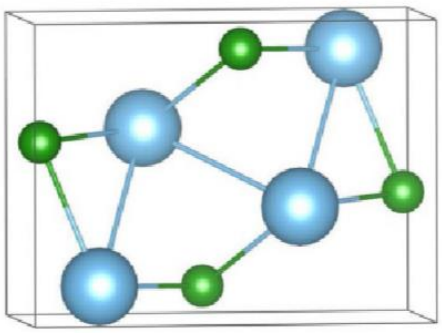

Fig 1.21: The orthorhombic crystal structure of TiB containing 4 Ti and 4 B atoms [56]

If the wt % of boron in the Ti alloy is greater than the eutectic limit then the volume fraction of TiB in the alloy is very high changing the alloy to a composite called as Titanium Metal-Matrix Composite. It has been reported by Miracle *et al* [57] and Morsi *et al* [58] that strength, resistance to wear and stiffness increase as the volume fraction of TiB increase in the hypo-eutectic regime. As a result, hypoeutectic alloys with low boron contents (<1 wt%) are technologically consistent for applications requiring fracture-critical materials since the ductility and toughness losses associated with B addition in these alloys are very less pronounced.

1.7.3 Effect of Boron Addition

Zhu et al [47] was the first to note that the presence of B significantly reduced the grain size of Ti alloys, and he attributed this to the TiB particles serving as heterogeneous nucleation areas. However, the TiB phase diagram indicates that TiB only develops in hypoeutectic compositions (<1.55 wt%) at $T_{eutectic}$ following the β-solidification of the alloy. Carrying this concept further Ramamurty *et al* [59] concluded that TiB needles are unable to serve as β-Ti nucleation regions. Also knowing about the extremely low solid solubility of B in Ti (<0.02 wt %), the excess B is rejected into the matrix resulting in the phenomenon of constitutional supercooling which boosts the rate of nucleation and also acts as a catalyst for it. In addition, the barrier created by extra B at the solid-liquid contact slows Ti's rate of development. Hence grain size refinement (Fig 1.22) occurs due to the combined effects of an escalation in nucleation rate and a decline in growth rate.

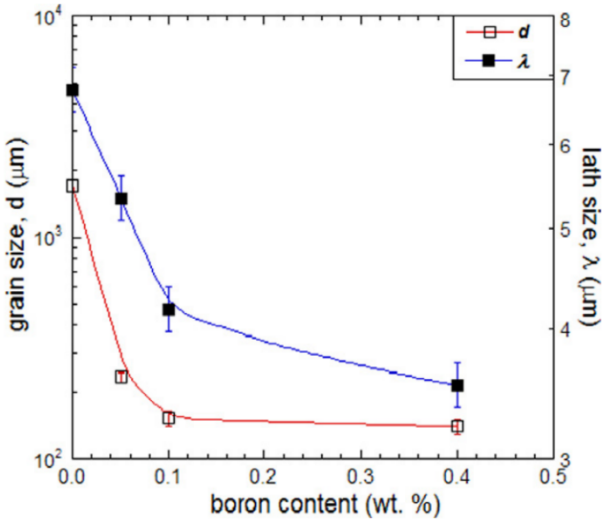

Fig 1.22: Variation of Grain and Lath size with increasing B content [59]

It has been seen that there is a thermal conductivity difference between the matrix and the TiB needles. As a result, the rate of nucleation of α-laths drastically increase during the cooling stage. This leads to a decline in the lath size also with increasing boron concentration (Fig 1.22).

1.7.4 Microstructural changes on Boron Addition

Ramamurty *et al* [60], [61] and Pederson *et al* [62] carried out thorough investigations on the changes in microstructural features in Ti-64 on the addition of Boron. The concentration of Boron traces was as follows:

- Ramamurty *et al* [60], [61] studied Ti-6Al-4V-xB (x = 0, 0.04, 0.09, 0.3, 0.55 wt % of B)
- Pederson *et al* [62] also studied Ti-6Al-4V-xB (x = 0, 0.06, 0.11 wt % of B)

According to Pederson *et al* [62] addition of traces of boron leads to a decrease in β-grains and α-colony sizes. The α-plates become smaller but broader and is present along the β-grain boundaries. The Tamirisakandala *et al* hypothesis [52] which states that boron contributes to grain size reduction during the process of solidification in two phases:

- Introduction of the Ti-β phase.
- Because of the boron-rich layer that has formed around the GBs, the beta nuclei's ability to grow will be limited as they cool further.

As the temperature falls below the $T_{solidus}$ at the time of solidification, a eutectic reaction occurs in which the liquid that is still present changes into the solid-β phase and TiB develops at the β-GBs. The TiB particles then hinder the beta grains' ability to proliferate

during the cooling process after leaving the high temperature regions. The transition from the beta phase to the alpha phase begins when the temperature falls below the material's $\beta_{transus}$. The first phase to emerge under specific cooling circumstances is known as grain boundary α because it occurs along the β-grain boundaries. The already present TiB particles then cohabit with this grain boundary. More grain boundary area per volume for the material is made possible by the smaller β grain size present in the boron treated materials. The number of α phase nucleation sites at the β grain boundaries increases due to the expansion of the β grain boundary region. The whole process is represented in Fig. 1.23.

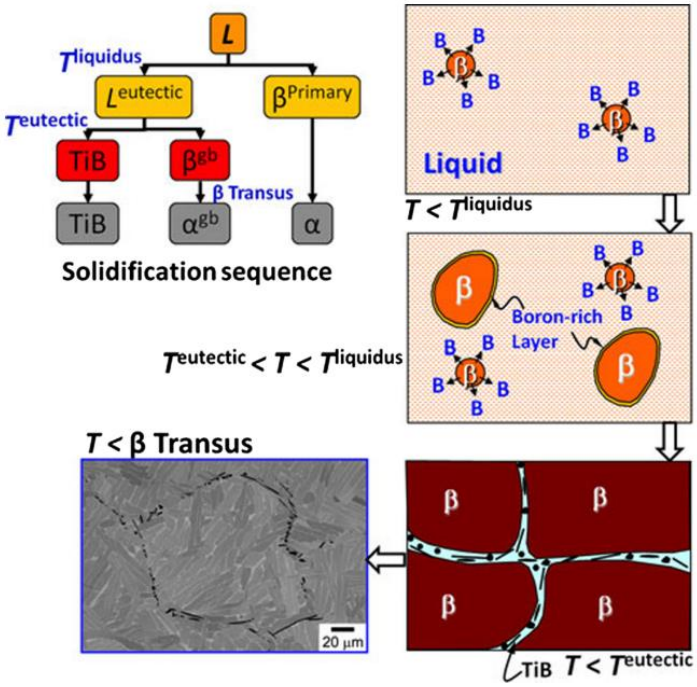

Fig 1.23: Grain size reduction process and solidification pathway for B-modified Ti-alloys specifically for the hypo-eutectic boron concentrations [17]

With the help of Optical microscopy and taking over 100 measurements for each Ti-6Al-4V-xB (x = 0, 0.04, 0.09, 0.3, 0.55 wt % of B) alloy Ramamurty *et al* [60] determined the size of the prior-β grains, the α-colony size and also measured the volume fractions of α, β and TiB by constructing an array of around 100 SEM images over an area of $1mm^2$ of the specimen for each alloy composition. The values of these parameters are mentioned in Table 1.8.

Composition	d (µm)	c (µm)	λ (µm)	V_α (%)	V_{TiB} (%)
Ti-64-0.00B	2386.2 ± 870.9	244.4 ± 51.1	2.5 ± 0.9	88.1 ± 2.1	0
Ti-64-0.04B	732.8 ± 278.0	22.2 ± 6.1	6.1 ± 2.0	92.8 ± 0.9	[a]
Ti-64-0.09B	223.9 ± 52.8	37.8 ± 10.7	4.5 ± 1.3	89.6 ± 1.6	0.49 ± 0.1
Ti-64-0.30B	121.1 ± 27.6	23.7 ± 6.6	4.7 ± 1.3	88.5 ± 3.3	1.8 ± 0.5
Ti-64-0.55B	100.1 ± 26.5	21.0 ± 7.1	5.3 ± 1.4	85.2 ± 3.3	2.7 ± 0.7

Table 1.8: Variation of different microstructural features with B content [60]

Where,

d = Prior-β grain size (in μm)

c = Size of the α/β colony (in μm)

λ = Size of the α-laths (in μm)

V_α = Vol. frac of α (%)

V_{TiB} = Vol. frac of TiB (%)

[a] = Value which is too low to be measured

1.8 High-Strain rate experiments

According to standardized testing techniques, material parameters like yield and ultimate strength that are mentioned in handbooks and design guides are often acquired under quasi-static loading circumstances utilising common testing load frames. The mechanical reaction of a material under such type of loading needs to be correctly defined in order to ensure product quality and dependability under impact conditions such those present in impact sports, automobile collision, or drop tests of electronic devices. Nevertheless, high-rate loading situations are outside the capabilities of standard material testing equipment.

Song and Chen [63] in their 2011 book define how the strain rate is actually calculated through an example: Suppose if a specimen's one end (10 mm in length) is deformed at speeds ranging from $1ms^{-1}$ to $100ms^{-1}$ then we can say that the body/specimen is experiencing a strain rate in the range of 10^2s^{-1} to 10^4s^{-1}. This strain-rate range is frequently encountered in loading circumstances including collisions. Nevertheless, most testing machines struggle to operate within this range in a precise manner. On the contrary, the ranges of strain rates during a hammer impact correlates to dynamic events frequently observed in engineering applications, such as bird impacts on aviation engine parts and club impacts on golf balls and hard surfaces. The material's characteristics should therefore be ascertained under hammer blowing circumstances.

Strain rate range	Classification	Experimental setup used
$< 10^{-6}$ s^{-1}	Creep	Servo hydraulic Machines
10^{-6} s^{-1} – 10^{-3} s^{-1}	Quasi-static deformation	
10^{0} s^{-1} – 10^{2} s^{-1}	Intermediate Rate	Drop towers
10^{2} s^{-1} – 10^{4} s^{-1}	High Strain Rate	Conventional SHPB
10^{4} s^{-1} – 10^{5} s^{-1}	Very High Strain Rate	Miniatured Kolsky Bars
10^{5} s^{-1} – 10^{6} s^{-1}		Pressure-shear plate impact
$> 10^{6}$ s^{-1}	Ultra-High Strain Rate	

Table 1.9: Experimental setups required at varied strain rates (Reprod. using [13])

The main experimental approaches used to measure the rate-dependent characteristics of materials are described by KT Ramesh [13] (Table 1.9).

1.8.1 The Split-Hopkinson Pressure Bar

Kolsky [64] in 1949 developed a really clever solution to the issues with high strain rate testing in order to acquire dynamic feedback of a material under controlled laboratory circumstances. He used two elastic rods (made up of Silver Steel) on either side of the specimen as a substitute for direct impact by blasting one out of the two rods with an explosive. The schematic of such a setup is represented in Fig. 1.24. Two lengthy bars that are intended to remain elastic at all times during the test make up the device's input and output bars. The small specimen (often cylindrical) sandwiched between these bars is anticipated to experience inelastic deformations. Usually, high-strength steels with very high values of σ_{YS} (Yield Strength) and significant toughness, like maraging steel, are used to make the bars. The gas gun along with the compressor setup helps in building up a substantial amount of pressure, thus creating an explosion like situation. Due to this explosion a compressive stress wave is formed pushing the striker bar to come in contact with the incident bar. Upon arrival at the interface of I/S, a fraction of the wave undergoes specular reflection back towards the incident bar, directed towards the impact end, while the residual segment propagates through the specimen, penetrating towards and entering the transmission bar.

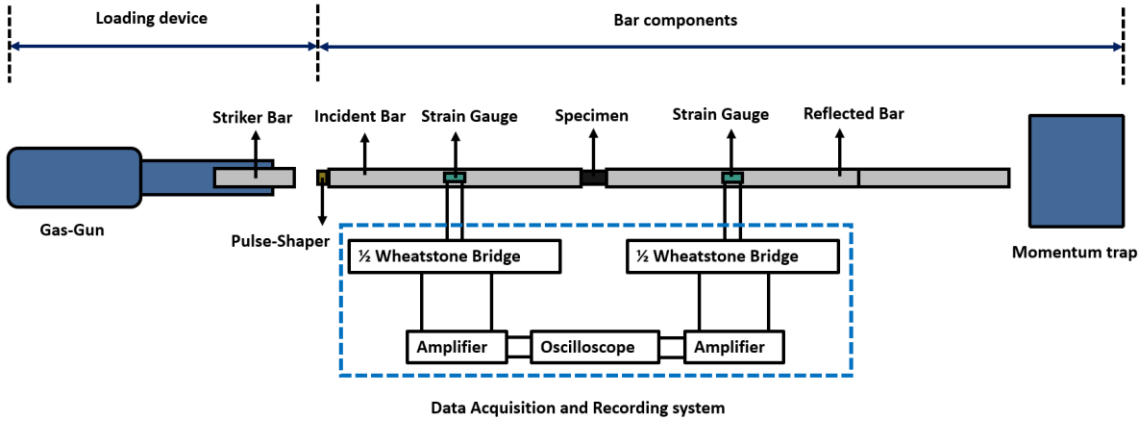

Fig 1.24: A general schematic of the SHPB setup (Reprod. using [63])

1.8.2 Miniatured Kolsky Bar

In a miniatured kolsky bar, very high strain rates ($\approx 5 \times 10^4\ s^{-1}$) can be achieved while the lowest strain rate achievable in such setups are around $10^3 s^{-1}$. Both theoretical and experimental results carried out by [16] show that this increased capability may be achieved without breaching the conditions for successful high-rate testing, and in fact while improving the correctness and accuracy of the experimental results. The bar diameter for such setups are around 3 mm and 30 mm in length [16].

1.8.3 Modified Kolsky Bar

For many years, the Charpy test was the most widely used testing method for categorising materials and determining their ductile-to-brittle transition temperatures; this is primarily due to its low cost and ease of application. The Charpy test apparatus has enabled the assessment of the x-t history while impact testing by either mounting a strain gauge on the tub or on the specimen. To acquire the pertinent fracture mechanics criteria, the x-t history can be employed in conjunction with the conventional quasi-static fracture mechanics analysis. Yet, because of inertial effects, the load received from the strain gauges oscillates around the real load. Furthermore, the time required for the load to reach its maximum value doesn't correspond to the time required for the fracture to initiate. This results in incorrect values of K_{Id} (Dynamic Fracture Toughness) according to the Quasi-static formula to calculate the dynamic fracture initiation toughness. Hence, the modified version of SHPB is used (Fig 1.25).

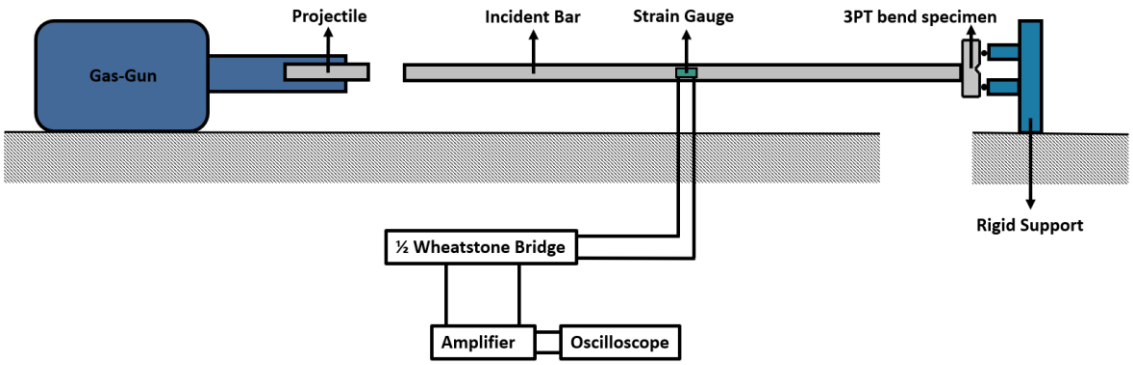

Fig 1.25: Schematic representation of the Modified SHPB for dynamic fracture experiments

The Modified Kolsky Bar uses the concepts of 1-D wave propagation and can be used to calculate the x-t history during the time of loading. The Modified SHPB has the following advantages over the conventional Charpy impact setup:

- Its setup is quite straightforward
- 1-D wave propagation concepts are used to accurately determine both P (Load) and $U_p(t)$ (Load-Point Displacement), and
- Material's Inertia repercussions are minimized to a large extent.

Chapter 2

LITERATURE REVIEW

This chapter describes the research conducted to investigate the influence of Boron modified as-cast Ti-6Al-4V alloys on mechanical properties. Previous research on the influence of boron addition on the K_{IC} (Quasi-Static Fracture Toughness) and K_{ID} (Dynamic Fracture Toughness) values of these alloys is also summarised. Following that, literary works that emphasise the Dynamic Fracture analysis are discussed. Finally, the chapter describes the research voids and the work objectives.

2.1 Mechanical Properties of Boron modified as-cast Ti-64 alloys

2.1.1 Elastic Modulus

Fig 2.1 summarizes all the obtained values of E, after reviewing numerous literary articles for as-cast Ti-6Al-4V-xB alloys. The figure includes the wt % of Boron as low as 0.016 wt % (less than the solubility limit of 0.02 wt %) to 2.2 wt % (hyper-eutectic composition in the TiB phase diagram). Singh *et al* [17] performed experiments on 5 specimens of Ti-64-xB (x = 0, 0.04, 0.09, 0.3 and 0.55) and found out that the Elastic Modulus increased from a value of 113 GPa to a value of 126 GPa for the 0.55 wt % sample. According to Singh *et al* [17] the Elastic Modulus (E) of Ti-6Al-4V-xB depends on the following factors:

- The E values for the different phases (α, β and TiB) present in the metal-matrix
- The volume fractions of the aforementioned phases in the matrix
- Composition of the elements present at the interstitial sites (Oxygen and Nitrogen to be specific)

I. Sen *et al* [61] performed nano-indentation experiments on as-cast Ti64-xB (x = 0, 0.04, 0.09, 0.3 and 0.55) to separately calculate the values of E for the α, β and TiB respectively. They found out that the TiB segregated at the grain boundaries was nearly 4 times stiffer than the α-phase ($E_{TiB} \approx 384.5 \pm 40.2$ GPa and $E_{\alpha} \approx 132.2 \pm 12.2$ GPa) while the β had the highest compliance. The reason given for the increase in stiffness with increase in Boron was the arrangement of TiB characterized by a configuration reminiscent to that of a necklace along the previous- β GBs.

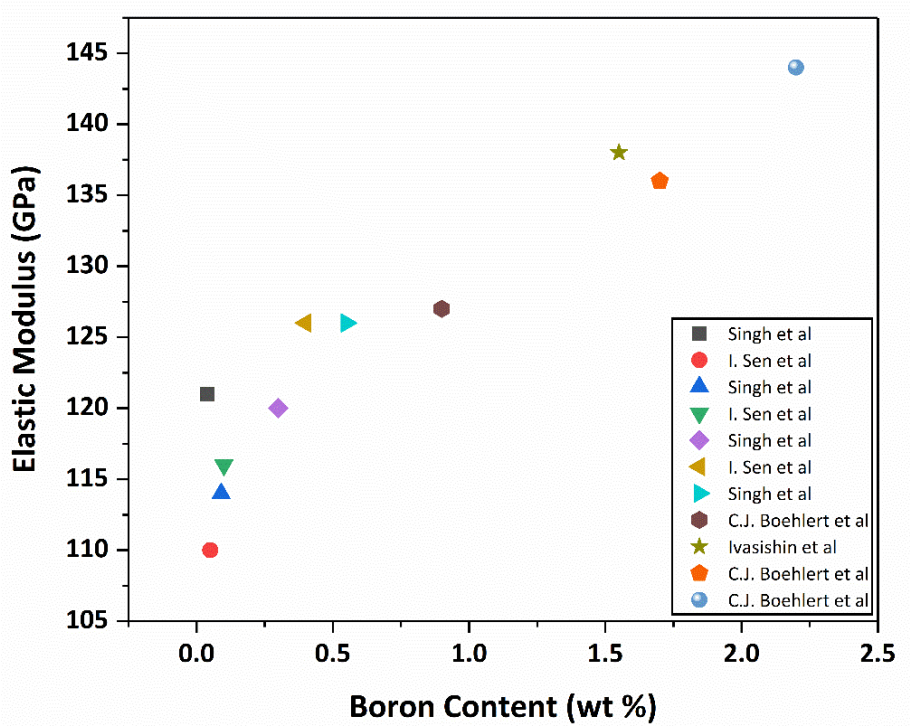

Fig 2.1: Variation of E with increase in Boron (Literature Survey Plot)

Table 2.1 provides a compilation for the different composition of Boron added to as-cast Ti-64 alloys along with their Elastic Modulus values.

Ti-64-xB Composition	Elastic Modulus Values (GPa)	Author and Journal	Ref
Ti-6Al-4V-0.04B	121	Singh *et al* (Progress in MS) [2021]	[17]
Ti-6Al-4V-0.05B	110	I. Sen *et al* (Acta Materialia) [2007]	[59]
Ti-6Al-4V-0.09B	114	Singh *et al* (Progress in MS) [2021]	[17]
Ti-6Al-4V-0.10B	116	I. Sen *et al* (Acta Materialia) [2007]	[59]
Ti-6Al-4V-0.30B	120	Singh *et al* (Progress in MS) [2021]	[17]
Ti-6Al-4V-0.40B	126	I. Sen *et al* (Acta Materialia) [2007]	[59]
Ti-6Al-4V-0.55B	126	Singh *et al* (Progress in MS) [2021]	[17]
Ti-6Al-4V-0.90B	127	C.J. Boehlert *et al* (Scripta Materialia) [2006]	[65]
Ti-6Al-4V-1.55B	138	Ivasishin *et al* (M & M Transactions A) [2008]	[66]
Ti-6Al-4V-1.70B	136	C.J. Boehlert *et al* (Scripta Materialia) [2006]	[65]
Ti-6Al-4V-2.20B	144	C.J. Boehlert *et al* (Scripta Materialia) [2006]	[65]

Table 2.1: Elastic Moduli values for as-cast Ti-64-xB alloys

2.1.2 Yield and Ultimate Tensile Strength

The Yield and Ultimate Tensile Strength is observed to increase with increasing Boron Content. The different reasons found in the literature for this to happen are as follows:

- According to I. Sen *et al* [59], the inclusion of B increases the strength mostly owing to the refinement in the microstructure (as discussed in the introduction chapter).
- The Hall-Petch relation also supports the statement mentioned above. The Hall-Petch relation is as follows:

$$\boldsymbol{\sigma_y = \sigma_0 + \frac{k}{\sqrt{d}}}$$

Where,

σ_y = Yield Stress

σ_0 = Resistance of the lattice to dislocation movement (Material Specific)

k = Strengthening Coefficient

d = Grain Diameter

As the microstructure gets refined, the grain size reduces leading to an increase in the σ_{YS} according to the Hall-Petch relation.

- Studies done by G. Lütjering [43] and Yapici *et al* [67] depict the role of the decrease in α-lath size leading to the decline in the effective slip length to be the reason for this increase in the Yield Strength.

- Better load distribution between the matrix and the TiB particles was observed by C. J. Boehlert *et al* [65] and they describe this load-sharing phenomenon to be the major reason for this increase in strength.

- Zhu *et al* [47] highlighted the concept of dispersion strengthening due to the presence of TiB particles which in turn acts as obstacles for the movement of dislocations during plastic deformation and thus imparting strength to the alloy.

Fig. 2.2 summarize the Yield Strength variation with the increasing Boron content after reviewing numerous literary articles for as-cast Ti-6Al-4V-xB alloys.

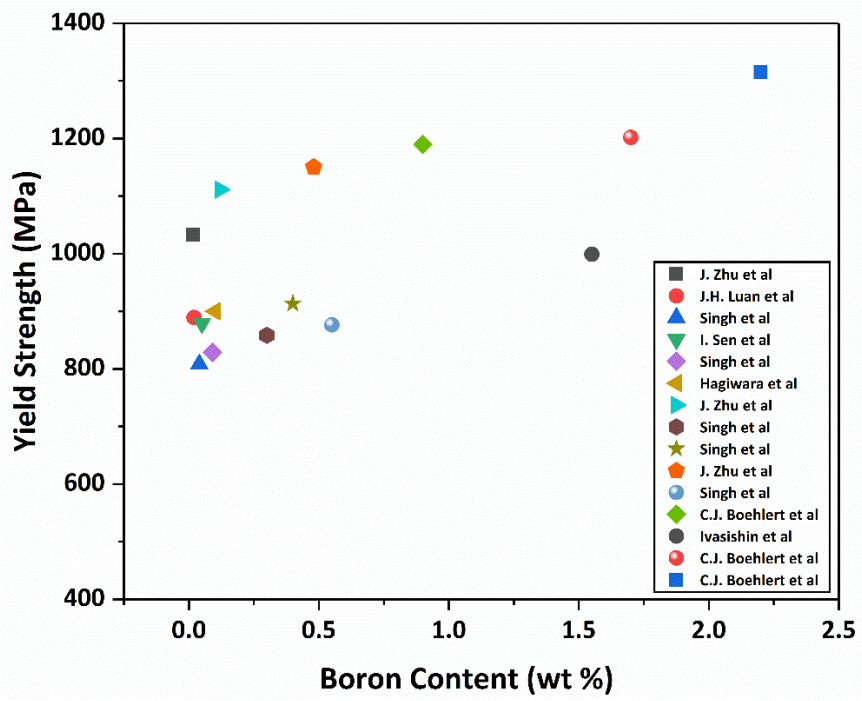

Fig 2.2: Variation of Yield Strength with increase in Boron (Literature Survey Plot)

A analogous pattern is discernible for the case of UTS of the as-cast Ti-6Al-4V-xB alloys. Fig 2.3 clearly depicts this increase in UTS after reviewing various as-cast Ti-64 alloys with different traces of Boron. The lowest Boron wt % is 0.02 (solid solubility limit of Boron in Ti-64) and it goes as high as 2.2 wt % (hyper-eutectic composition).

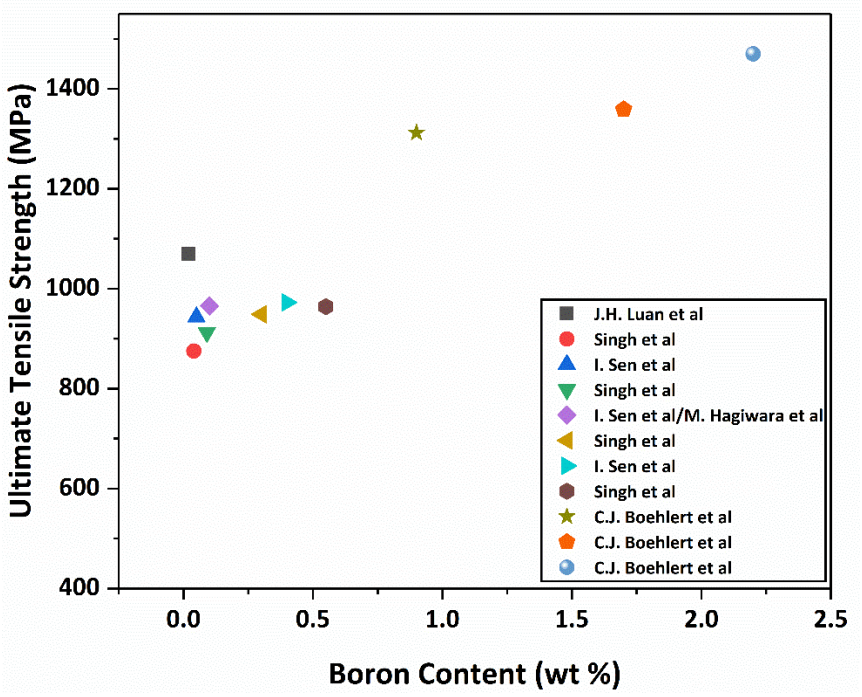

Fig 2.3: Variation of UTS with increase in Boron (Literature Survey Plot)

2.1.3 Hardness

The hardness is observed to increase with the increasing concentration of Boron in the Ti-64 alloy as seen in numerous literary works. The reasons reported for this increase are listed below:

- Anthony C. in his book *Nanoindentation* [68] concluded that during hardness testing (Static Case), generally load is applied using a spherical or a pyramidal indenter. He also mentions that it is really intriguing to study the pressure distributed around the indenter during the application of load. It has been proven using experiments that p_m (mean effective pressure) between the specimen being tested and the indenter used is directly proportional to the material's Yield Strength and is given by the Tabor's equation as:

  $$\boldsymbol{H_v \sim C_v \sigma_y}$$

  Where, C_v is called as the Constraint Factor and its value depends on the material type, the indenter type and other criterions related to the experiment. Anthony C. [68] also reports that the experiments show that the value of C_v is nearly equal to 3 for materials having a very high ratio of Young's Modulus (E) to the Yield Strength (Y) i.e., E/Y ratio (Like in the case of Metals).

- I. Sen *et al* [59] developed empirical relations between the Vickers's Hardness and the size of the α-lath and the β-grains using the Hall-Petch relation:

  $$\boldsymbol{H_v = 302.1 + 883.4\left(d_\beta\right)^{-1/2}}$$

  $$\boldsymbol{H_v = 188.6 + 369.2\ \left(d_\alpha\right)^{-1/2}}$$

  However, they also mention the presence of the TiB inter-metallics segregated at the grain boundaries to be the reason for this enhanced hardness as the hardness reported for TiB by K. Euh *et al* [69] is around 700 VHN.

2.1.4 Strain to failure (ε_f %)

I. Sen *et al* [60] tested Ti-64-xB (x = 0, 0.04, 0.09, 0.3, 0.55) and found out that the ductility/strain to failure increased up to 0.09 wt % of Boron and then dipped. The increase up to 0.09 wt % B was attributed to the grain refinement experienced due to B addition. The reason for the dip after 0.09 B was due to the high-volume fractions of brittle and hard TiB found in the 0.3 and 0.55 wt % specimens.

2.2 Effect of Boron addition on fracture behaviour of Ti-64-xB

2.2.1 Quasi-Static Fracture

The Quasi-Static Fracture Toughness (K_{IC}) tend to decrease as the Boron concentration increases in the alloy. I. Sen *et al* [59] provides a thorough explanation about the possible reasons that could lead to such an observation:

- The decrease in Quasi-Static Fracture Toughness (K_{IC}) is mainly due to the refined microstructure obtained after the addition of Boron. Because as the microstructure gets the defined the crack path becomes more and more tortuous hindering its ease to propagate.
- Scanning Electron Microscopy images showed a diminishment in the fracture surface roughness with increase in B content. This might be the other reason for this decrease in toughness.
- They also report that the Fracture Toughness of a material is dependent on an optimal mix of σ_y (Yield Strength) and COD (Crack Opening Displacement) and both the quantities aforementioned are dependent on each other too i.e., as the Yield Strength increases the COD dips drastically.
- The local ductility (near the crack tip) plays a major role in defining a specimen's Fracture Toughness. The local ductility is a function of the COD and hence dips as the COD decreases. It is worth noting that the global ductility is not a defining factor for K_{IC} (as seen by the ε_f % in the previous section).
- The major phenomenon responsible for an increased flow stress is strain hardening. Absence of it near the crack tip limits its susceptibility to localization. But due to the presence of TiB particles near the crack tip the phenomenon of localization can be activated and as a result COD decreases. With increasing B concentration, the volume percentage of TiB increases, resulting in decreased toughness.
- Ritchie R – Knob J – Rice J (RKR) [70] developed a micro-mechanical model for the critical stress against the fracture toughness for mild steel samples so I. Sen *et al* [59] explained the possible reason for the decrease in the Quasi-Static Fracture Toughness for Ti-64-xB using this model. According to the RKR model in materials where a trans-granular type of cleavage fracture occurs (due to the initiation of slip) there is an unstable propagation of cracks when the highest value of the local principal stress ($\sigma_y^{max}|_{\theta=0}$) exceeds the critical stress value required for fracture (σ_f^*) over a microstructurally consequential distinctive length scale (l_0^*). RKR [70] defined the dependency of K_{IC} as follows:

$$\boldsymbol{K_{IC} = \sqrt{l_0^*}\ \frac{(\sigma_f^*)^{\frac{n+1}{n}}}{(\sigma_y)^{\frac{n-1}{2}}}\ [g(n)]^{\frac{-(n+1)}{2}}}$$

Where, $[g(n)]$ is basically a constant dependent on the Poisson's Ratio of the material and also on n (work hardening exponent). Studies done by I. Sen *et al* [59] describe very less to no changes to n with varying Boron content and studies also

show the value of n to be nearly equal to zero. So, the equation suggested by the RKR model now reduces to:

$$K_{IC} \propto \sqrt{l_0^* \sigma_y}$$

Fractography showed typical cleavage of the α-laths so I. Sen *et al* [59] concluded the micro-structural length scale to be the lath-size (λ). Table 2.2 represents the reported α-lath sizes and σ_y values with increasing Boron content. With increasing Boron content, the lath size decreases drastically vis-à-vis increase in the Yield Strength, hence the overall product mentioned in the aforementioned equation decreases.

Ti-64-xB Composition	**Lath-Size (λ) [in μm]**	**Yield Strength (σ_y) [in MPa]**	**Source**
Ti-64	6.8 ± 1.8	833.9	I. Sen et al, Acta Materialia (2007) [59]
Ti-64-0.05B	5.3 ± 1.5	878.7	
Ti-64-0.1B	4.2 ± 1.2	900.0	
Ti-64-0.4B	3.5 ± 1.1	913.3	

Table 2.2: Defining Parameters for the RKR Model used for the calculation of K_{IC}

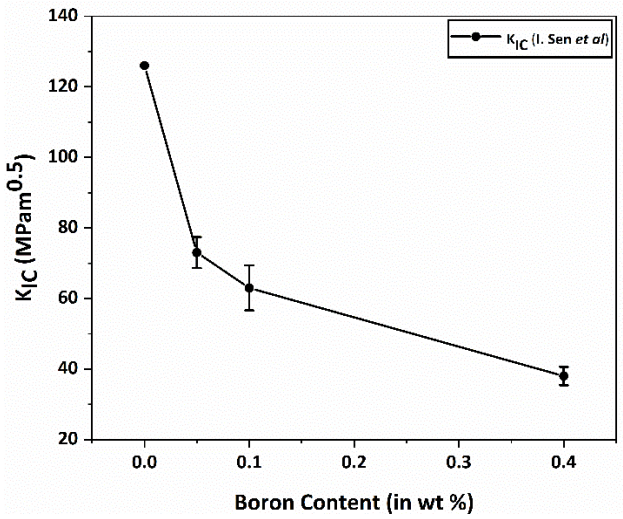

Fig 2.4: Variation of K_{IC} with Boron Content (Reprod. using [59])

2.2.2 Dynamic Mechanical Behaviour

The literature available on the dynamic behaviour of Boron Modified as-cast Ti-64 alloys is very limited. Yu *et al* [71] compared the dynamic mechanical properties of the Ti-64 alloy with the Ti-64-0.1B sample by dynamic compression using a Split Hopkinson Pressure Bar. They also used different heat treatment methods to obtain different microstructures and develop a microstructure – dynamic property relationship between the two. Fig. 2.5 represent the true stress – strain curves for Ti-64 and Ti-64-0.1B for different microstructures.

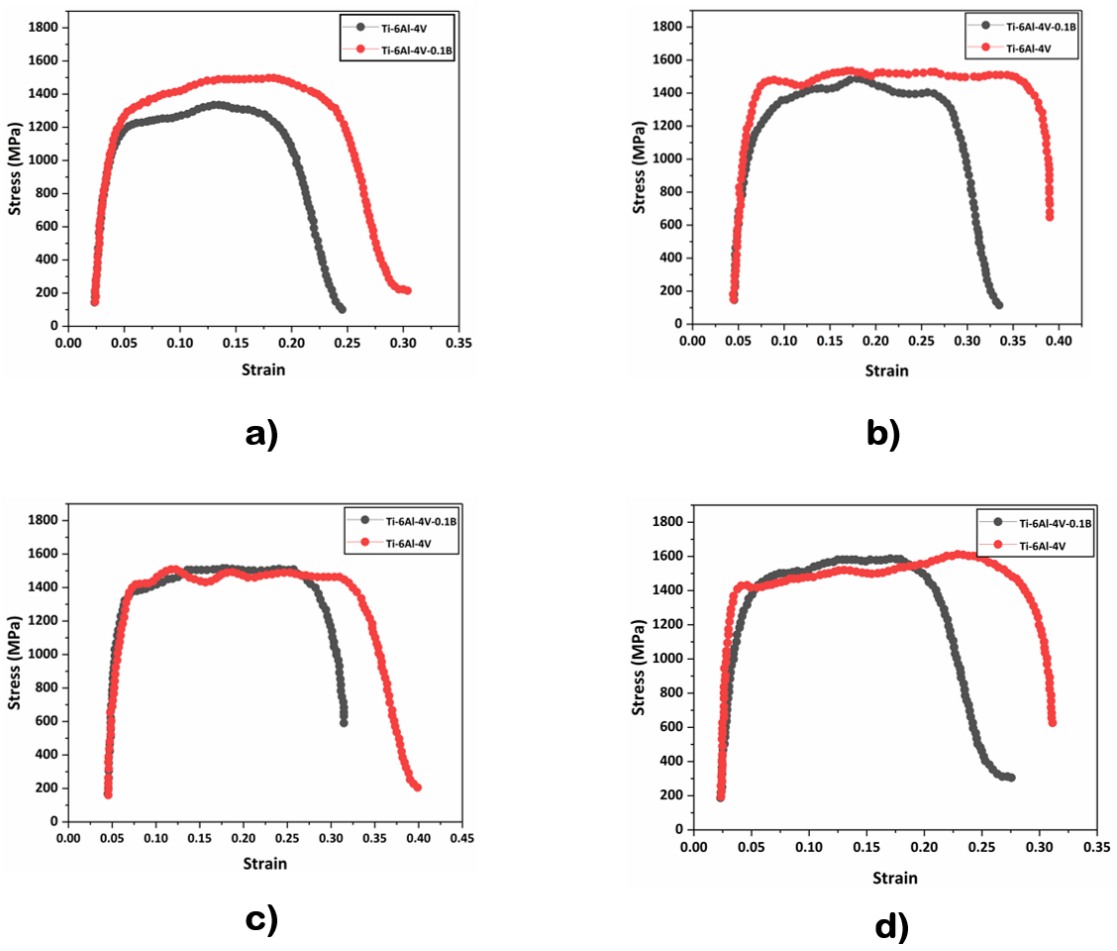

Fig 2.5: The dynamic σ_{true} v/s ε_{true} curves comparison for Ti-64 and Ti-64-0.1B having different microstructures: **a)** as-cast **b)** equi-axed **c)** bimodal **d)** Widmanstätten (Reprod. using [71])

They also describe the dynamic deformation process viz. Firstly the samples underwent elastic deformation followed by the plastic deformation and finally due to the localization of adiabatic shear bands the material failed. Table 2.3 represents the values of Average Flow Stress and the Plastic Strain observed reported by Yu *et al* [71] . The strain rates at which the experiments were carried out are also represented.

Type of Microstructure	Alloy Composition	Strain Rate (s^{-1})	Plastic Strain	Avg. Dynamic Flow Stress (MPa)
As-Cast	Ti-6Al-4V	3500	0.17	1255
	Ti-6Al-4V-0.1B	3500	0.22	1407
Equi-axed	Ti-6Al-4V	4000	0.33	1510
	Ti-6Al-4V-0.1B	3500	0.24	1403
Bimodal	Ti-6Al-4V	4000	0.3	1450
	Ti-6Al-4V-0.1B	3100	0.27	1461
Widmanstätten	Ti-6Al-4V	4000	0.26	1500
	Ti-6Al-4V-0.1B	3500	0.18	1506

Table 2.3: Dynamic Properties of Ti-64 v/s Ti-64-0.1B as reported by Yu *et al* [71]

Yu *et al* [71] also mentioned the vital role of the absorbed energy during dynamic deformation and developed a relation between the microstructure of the alloy and the energy absorbed by it. According to Yu *et al* [71] the amount of energy absorbed during dynamic deformation plays a significant metric for determining dynamic mechanical properties. The mathematical equation they used to calculate the absorbed energy for different microstructures was as follows:

$$\boldsymbol{E = \int_{\varepsilon_s}^{\varepsilon_f} \sigma . d\varepsilon}$$

Where, the quantities ε_s and ε_f denote the strains at the start and the finish of the plastic deformation. Table 2.4 represent the maximum energy absorbed by samples having different microstructures.

Microstructure	$E_{Ti\text{-}6Al\text{-}4V}$ (MJ/m^3)	$E_{Ti\text{-}6Al\text{-}4V\text{-}0.1B}$ (MJ/m^3)	Remarks
As-Cast	214	321	↑ in Energy Absorption
Equi-axed	490	340	↓ in Energy Absorption
Bimodal	440	388	↓ in Energy Absorption
Widmanstätten	400	269	↓ in Energy Absorption

Table 2.4: Energy absorbed by specimens possessing different microstructures for Ti-64 and Ti-64-0.1B samples as reported by Yu *et al* [71]

So, Yu *et al* [71] concluded that on the addition of Boron (0.1 wt %) to the as-cast samples the dynamic properties improved while for the other microstructures the properties dipped on the addition of Boron. The least decrease happened for Widmanstätten followed by Equi-axed and finally Bimodal.

2.3 Experimental studies done on Dynamic Fracture

When a material fractures, different phenomenon occur at different time intervals near the tip of the crack and these material fracture properties are also quantified using different parameters viz.

- Initiation of the Crack (Quantified using Dynamic Fracture Toughness [K_{ID}])
- Propagation of the crack (Quantified using Propagation Fracture Toughness)
- Arrest of the Crack (Quantified using the Arrest Toughness)

Out of all the three the Dynamic Fracture Toughness/Dynamic Fracture Initiation Toughness is the most critical Fracture Mechanics criterion. It is well understood that the fracture behaviour of materials is proportional to the loading rate. Numerous studies show that K_{ID} (Dynamic Fracture Toughness) differs significantly from K_{IC} (Quasi-Static Fracture Toughness). Fracture Toughness is an attribute of a material that varies with loading rate. The loading rate for a particular dynamic experiment is defined in terms of a quantity coined as the Stress Intensity Factor Rate (K_I) and follows the following equation:

$$\boldsymbol{K_I = \frac{K_{ID}}{t_f}}$$

Where, K_{ID} is the Dynamic SIF and t_f is the time required for the crack to initiate.

In comparison to dynamic loading, the experimental methodologies used to determine quasi-static fracture toughness for both brittle and ductile materials are well known. The Quasi-Static studies are so well known that even ASTM has published a set of procedures and rules for determining the Quasi-Static Fracture Toughness under ASTM-E399 (LEFM). Very few standard procedures are available for dynamic fracture toughness calculations of materials like for example: ASTM E24.03.03 suggests standard test procedures for testing materials using the Charpy Impact Testing machines but that was only confined to loading rates up to 10^5 MPa$\sqrt{ms^{-1}}$ and no defined SOPs are mentioned for loading rates in the range of 10^6 MPa$\sqrt{ms^{-1}}$ to 10^7 MPa$\sqrt{ms^{-1}}$ which generally arise while testing materials using the Split Hopkinson Pressure Bar.

Numerous modifications have been done to study a material's dynamic response using the SHPB. The modification aforementioned may be in the testing apparatus itself, or the specimen geometry. Some of the tests are mentioned below:

2.3.1 One Bar – One Point Bend Fracture Test (1B/1PB)

Homma *et al* [72] were the first ones to modify the conventional SHPB into a 1B/1PB setup by removing the transmission bar. The setup only consisted of the Striker Bar, The Incident Bar, and the Pre-Cracked Specimen. Both modes of Fracture (I and II) were compatible with this setup. Fig. 2.6 shows the schematic of such a setup.

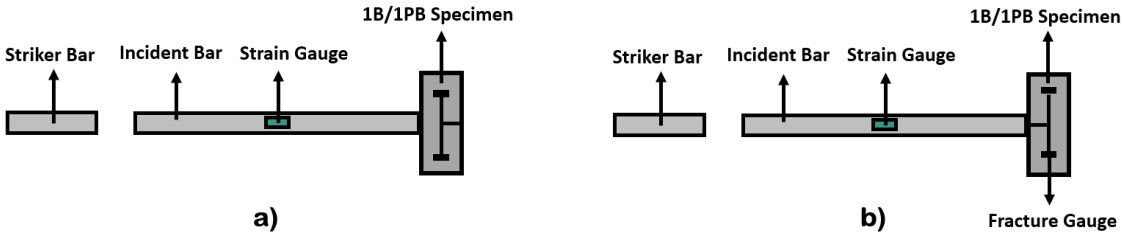

Fig 2.6: A typical schematic of the 1B/1PB Fracture Test in **a)** Mode-I (Reprod. using [73]) **b)** Mode-II (Reprod. using [74])

With this modification to the Hopkinson Bar Homma *et al* [72] performed Dynamic Fracture experiments for SM50A Steel. Later on, he also tested the 7075-T651 [75] and 6061-T651 [76] Al alloys. Similar testing setup was used by Wada *et al* [77]–[79] for the Dynamic Fracture testing of Poly-Methyl-Methacrylate (PMMA).

Another modification done to the Hopkinson Bar was to remove the incident bar and use the Striker Bar directly as an impacting entity. Kalthoff *et al* [80], [81] and Rosakis *et al* [82], [83] used this modification to test different material's dynamic fracture initiation toughness.

2.3.2 One Bar – Three Point Bend Fracture Test (1B/3PB)

The only differentiating factor in the 1B/3PB setup as opposed to the 1B/1PB setup is the presence of 2 supports in the former which is absent in the latter. The experimental setup of a 1B/3PB Hopkinson Bar almost resembles the simply supported beam (Fig. 2.7). Mines and Ruiz [84] were the first ones to modify the conventional Charpy Impact Testing setup by introducing an additional tup which remains in contact with the specimen. So, the Tup which would have directly impacted on the specimen now impacted on this additionally added tup.

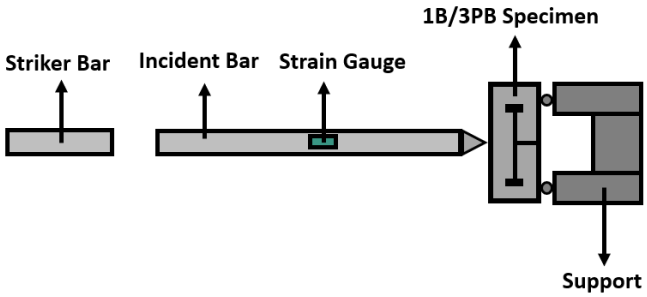

Fig 2.7: A typical schematic of the 1B/3PB Hopkinson Bar Experimental Setup (Reprod. using Rubio *et al* [85])

In the same year Mines and Ruiz used the same type of modification in the SHPB setup [86]. They used a comparatively longer striker bar (approximately 1000 mm long) in order to generate a loading pulse which was longer in duration so that the material gets fractured in the first loading period itself thereby averting the effect of multiple stress waves which in turn helps in deciphering the experimental results easily. Table 2.5 and 2.6 provides an overview of the materials tested using the 1B/3PB Hopkinson Bar setup.

Material Tested	Specification	Authors and Journal	Reference	Remarks
STEELS	EN24	Dutton *et al* (1991) [International Journal of Fracture]	[87]	A 1-D spring-mass model of the SHPB was designed and the same was used to estimate the K_{ID} values.
	40 Cr Steel	W.G. Guo *et al* (1997) [Theoretical and Applied Fracture Mechanics]	[88]	FEM analysis was used to calculate the time history of the propagating stress wave, load-point displacement and K_{ID}. The results showed good agreement with the ones deciphered experimentally.
	40 Cr and 30CrMnSiNi2A	Zejian *et al* (2006) [Acta Metallurgica Sinica]	[89]	The variation of KID with the loading rate was examined. A combined numerical and experimental approach was used. FEA concluded that 40Cr's K_{ID} is insensitive to the loading rate and K_{ID} increased with loading

				rate for 30CrMnSiNi2A. The loading rate was around 10^6MPa$\sqrt{}$ms^{-1}.
	AISI 4340 Steel	Anderson *et al* (2003) [AIP Conference Proceedings]	[90]	A rather uncomplicated Quasi-Static model was used for KID calculations.

Table 2.5: Different types of Steels tested using the 1B/3PB Experimental Setup

Material Tested	Specification	Authors and Journal	Reference	Remarks
COMPOSITES	C/C-SiC	Srivastava *et al* (2004) [Composite Science and Technology]	[91]	1B/3PB tests were carried out to calculate K_{ID} for both the Oxidized and Non-Oxidized Specimens of C/C-SiC Composites. The roughness of the specimen's surface, created via oxidation was found to diminish the dynamic stress amplitude. Although the $(K_{ID})_{oxidized}$ is always less than the non-oxidized one. This demonstrates that the loading technique and material conditioning have a significant impact on composite specimens.

Table 2.6: Composites tested using the 1B/3PB Experimental Setup

2.3.3 Two Bar – Three Point Bend Fracture Test (2B/3PB)

This is a slight modified version of the 1B/3PB Hopkinson Bar setup. The 2B/3PB test differs from the 1B/3PB in mainly two ways viz. Instead of just the incident bar, transmission bar is also present in the 2B/3PB test and also permanent grooves are made in both the bars so as to support the specimen from both the sides as if forming a simply supported beam type of setup. Fig. 2.8 represents the schematic of such a setup.

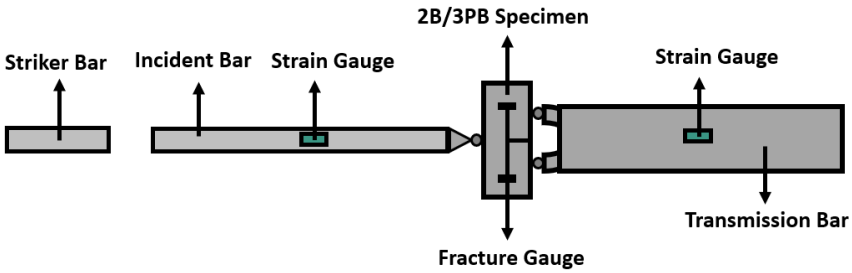

Fig 2.8: A typical schematic of the 2B/3PB Hopkinson Bar Experimental Setup (Reprod. using Vecchio *et al* [92])

2.3.4 Three Bar – Three Point Bend Fracture Test (3B/3PB)

A 3B/3PB Hopkinson Bar Experimental setup consists of the striker bar, the incident bar and two transmission bars. The specimen is placed between the incident bar and both the transmission bars. This technique was developed by 2 professors of the Osaka University viz. T. Yokohama and K. Kishida [93]. Fig. 2.9 shows the schematic of the setup proposed by the aforementioned professors.

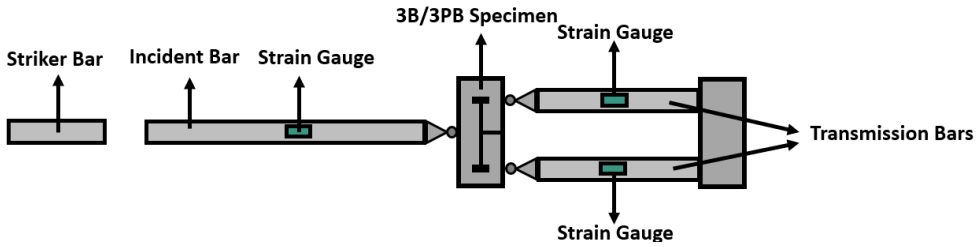

Fig 2.9: A typical schematic of the 3B/3PB Hopkinson Bar Experimental Setup (Reprod. using Yokohama and Kishida [93])

Table 2.7 gives an overall summary of the prominent research groups primarily working in the field of Dynamic Fracture of Materials worldwide.

Group	Institute	Active Research Conducted	Loading Method Used	Method of K_{ID} Interpretation
Rosakis	Caltech, USA	K_{ID} Calculations and Crack Dynamics	1B/1PB	Coherent Gradient Sensing (Optical Method)
Homma	Toyohashi University of Technology, Japan	K_{ID} Calculations and Fracture Mechanics	1B/1PB	FEA and Strain Gauge Method
Rittel	IIT, Israel	K_{ID}, K_{IID} Calculations and Fracture Mechanics	1B/1PB and 2B/CCS	FEA and Strain Gauge Method
Prakash	Case Western Reserve University, USA	K_{ID} Calculations and Fracture Mechanics	1B/3PB	Quasi-Static Fracture Approximation and Strain Gauge
Shukla	University of Rhode Island, USA	K_{ID} Calculations, Fracture Mechanics, and Crack Dynamics	1B/3PB and 1B/1PB	CGS and Strain Gauge Method
Vecchio	UCSD, USA	K_{ID} Calculations and Fracture Mechanics	2B/3PB	Strain Gauge Method and Quasi-Static Theory
Todo	Kyushu University, USA	K_{IID} Calculations and Fracture Mechanics	3B/3PB	FEA and Strain Gauge Method

Table 2.7: Prominent Research Groups and the Active Research Conducted by them

2.4 Research Gaps

- Significant research has been conducted to investigate the dynamic behaviour of Ti-64 alloys with various microstructures generated via various processing techniques at various strain rate regimes. But very less efforts are made to study the Dynamic Behaviour of Boron Modified as-cast Ti-64 alloys. The literature which is available is only confined up to a Boron concentration of 0.1 wt % and no data is available above this composition.
- The limited research done on Boron Modified Ti-64's Dynamic Behaviour is only confined to strain rates ~ 10^3 s^{-1}.
- A clear explanation of the involvement of TiB particles in the Ti-64-xB matrix is still lacking in the literature, and the deformation process causing the dynamic fracture behaviour remains unknown.
- No literature is available on till now that focuses on evaluating the Dynamic Fracture Toughness (K_{ID}) of Boron Modified as-cast Ti-64 alloys.
- The research done on Dynamic Fracture Mechanism and the role of microstructures in influencing such phenomenon is still obscure.

2.5 Objectives

- Modify the Conventional Hopkinson Bar setup into a One Bar/ Three-Point Bend (1B/3PB) setup to evaluate the Dynamic Fracture Toughness (K_{ID}) of Boron Modified as-cast Ti-64 alloys at a loading rate ranging from 10^6 MPa$\sqrt{m}s^{-1}$ to 10^7 MPa$\sqrt{m}s^{-1}$.
- Employ a High-Speed Camera facility to study the crack propagation behaviour at such high rates of loading frame-by-frame.
- To scrutinize the influence of Boron on the microstructure, mechanical characteristics, and dynamic fracture behaviour of the as-cast Ti-64-xB alloy.

Chapter 3

METHODOLOGY

This chapter presents an exhaustive exposition, providing intricate insights and comprehensive coverage of the material's manufacturing as well as the experimental and microstructural characterisation methodologies used in the current work.

3.1 Material Used

The samples of Ti-6Al-4V-xB (x = 0, 0.04, 0.09, 0.3, 0.55) were procured from the Flow Serve Corporation (at Dayton, Ohio). The as-received samples were in the form of cylindrical ingots. The diameter and the length of the as-received cylindrical ingots were 75 mm and 180 mm respectively. The ISM (Induction Skull Melting) technique was used to prepare the casting. Through the use of an induction coil and a vacuum or controlled atmosphere, induction skull melting (ISM) is a technique used for melting metals in a segmented, water-cooled copper vessel. There is no refractory lining present and a direct contact is established between the metal to be melted and the metal with which the refractory lining is made up of. While casting, a regulated environment was present, and when elemental Boron was added to the melt, it completely dissolved. Finally, to make sure the obtained casting is pore free the Hot-Isostatic Pressing treatment was employed and the parameters were as follows:

- Duration: Approx. 2 hrs
- Temperature: 1173 K
- Pressure: 100 MPa

3.2 Experimental Characterization

3.2.1 Machining of the Specimens

3.2.1.1 For Microstructural and Scanning Electron Microscopy Analysis

Cylindrical samples having a length of 4 mm and a diameter of 2 were cut using the Electrical Discharge Machining Technique from the as-received cylindrical ingots. Fig. 3.1 represents the schematic of the samples used for the analysis.

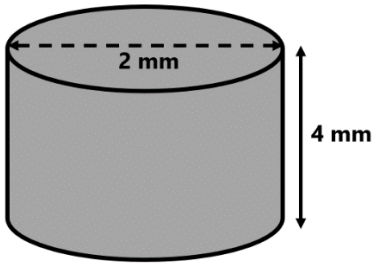

Fig 3.1: Schematic of the specimen used for Microstructural and SEM analysis

3.2.1.2 For Microhardness Testing

Cuboidal samples having a Length, Width and Height of 50 mm, 5 mm and 10 mm respectively using the Electrical Discharge Machining Technique from the as-received cylindrical ingots. Fig. 3.2 represents the schematic of the samples used for the analysis.

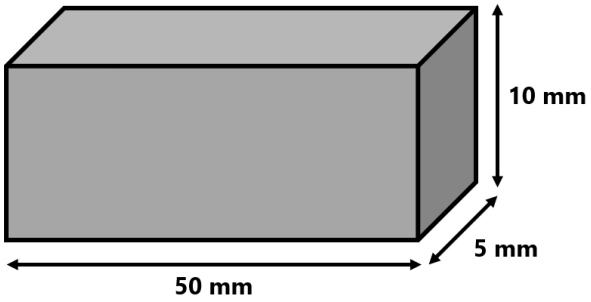

Fig 3.2: Schematic of the specimen used for Microhardness Testing

3.2.1.3 For Dynamic Fracture Experiments

A typical 3PB specimen having a Length, Width, Breadth and Crack length of 50 mm, 10 mm, 5 mm, and 4 mm respectively was used for the Dynamic Fracture experiments on the Modified Hopkinson Bar. Fig. 3.3 represents the schematic of the samples used for the analysis.

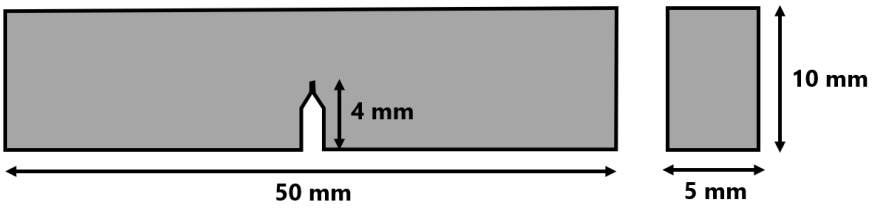

Fig 3.3: Schematic of the specimen used for 1B/3PB Dynamic Fracture experiments

3.2.2 Polishing of the Specimens

To analyse the microstructure of the different specimens of Ti-64-xB the EDMd samples (mentioned in 3.2.1.1) were encapsulated using a Thermosetting Resin by the name of PhenoCure, which exhibits a phenolic nature using the Buehler's SimpliMet 3000 Hot Mounting Press. After finishing the mounting process, the samples were then polished on the Bainpol VTD polishing machine (made by Chennai Metco) using a range of emery papers (starting from a grit size of 600 and going up to a grit size of 3000). In order to attain a mirror finish, Alumina Paste having the particle size ranging from 0.25 μm to 2 μm was used to polish the samples on a velvet cloth. Lastly, the samples were cleaned using an Ultrasonicating Machine (by PCI Analytics) in a solution of Water and Ethanol and then air-dried.

3.2.3 Microstructural Characterization

To observe the microstructure, the samples were etched using Kroll's reagent. A 50 ml solution of the Kroll's reagent has the following constituents:

- De-Ionised Water: 46 ml
- Nitric Acid (HNO_3): 3 ml
- Hydrofluoric Acid (HF): 1 ml

The etching was carried out for a time of approximately 20 sec for each sample followed by washing them using clean water and air drying using a blow dryer. Microstructural details are made visible via etching that are otherwise invisible on the sample after polishing. The characteristics of the existing phases, inclusions, as well as the dimension, form, arrangement and segregation of the grains, may all be seen in a properly prepared specimen.

ZIESS's Axio Vertical A1 Inverted Optical Microscope was used to capture the microstructures of various Ti-64-xB samples at different magnifications, starting from 100 X and going up to 2000 X. To study the microstructural features more deeply, SEM analysis was done using the JEOL's Benchtop FESEM-EDS setup.

3.2.4 Microhardness Testing

A partially automatic Vicker's Hardness machine was used to measure the hardness of the samples. A 50 g load was used and the machine had a dwell time of 20 sec and the velocity of the loading/unloading was around 60 μm/sec.

3.2.5 Dynamic Fracture

3.2.5.1 Modifications done to the conventional SHPB

The addition of a fixture to hold the specimen in a 1B/3PB configuration transformed the standard 12 mm Hopkinson Bar into a modified SHPB. The schematic of such a setup was represented in Chapter 1 (Fig. 1.25). The specifications of the modified Hopkinson Bar used to perform the Dynamic Fracture experiments are listed below:

- All the bars of the modified Hopkinson Bar were made up of an Aluminium alloy (Al-2062-T6). The diameter of each bar is 12 mm.
- The length of the input bar was 2500 mm. The strain gauges are mounted at diametrically opposite positions on the input bar to capture the signals during the time of impact. Also, the strain gauges are mounted at the centre of the bar just to avoid overlapping of the waves.
- The length of the striker/projectile bar was 650 mm and produces a loading pulse of around 250 μs. A quick discharge of compressed air from a pressure vessel

propels the striker, which accelerates the striker bar until it collides with the incident bar. The striker bar was able to reach speeds of about 12 m/s during the testing.

- A High-Speed Camera (Phantom V12) having a 256*128-pixel resolution was placed parallel to the specimen to analyse the crack opening and propagation. The V12 had a sampling rate of 130000 frames per second and captured images after every 7.7 μs. To analyse the high-speed camera images the Cine Viewer (CV 3.7) software, from the makers of the V12 was used.

3.2.5.2 Basis of K_{ID} measurement

According to Rubio *et al* [85] in order to calculate the K_{ID} we need to quantify two parameters viz. the progression of the Stress Intensity Factor with time ($K_{I(t)}$) and the time required to fracture the specimen (t_f). Rubio *et al* [85] proposed 3 methods for the quantification of the Dynamic Stress Intensity Factor and the 4th method was proposed by the Anderson *et al* [24]. All of these methods are explained briefly below:

- **Peak Load Method** (Rubio *et al* [85], *Experimental Mechanics* [*2003*])

The equation proposed by Rubio *et al* [85] for K_{ID} taking the applied load $P(t)$ into account is as follows:

$$\boldsymbol{K_{ID} = \frac{3}{2}\frac{P(t)\beta}{B\sqrt{W}}\frac{\sqrt{\alpha}}{(1+2\alpha)(1-\alpha)^{3/2}}f(\alpha)}$$

With,

$$\boldsymbol{f(\alpha) = (1.99 - \alpha(1-\alpha)(2.15 - 3.93\alpha + 2.7\alpha^2))}$$

Where, $P(t)$ is the applied load at the time of impact, a is the length of the crack, S is the span or it can also be defined as the distance between the two supports in a 1B/3PB setup, W is the width of the specimen, α is the ratio of the crack length to the width and β is the ratio of the span to the width of the 3PB specimen.

- **Load Point Displacement Method** (Rubio *et al* [85], *Experimental Mechanics* [*2003*])

Bacon *et al* [94] proposed the formula for the static stress intensity factor (K_{IC}). Assuming the relation also holds true in the dynamic regime Rubio *et al* [85] proposed the following equation to quantify the K_{ID}:

$$\boldsymbol{K_{ID} = \frac{3}{2}\frac{\beta}{B\sqrt{W}}\frac{u_p(t)}{C(\alpha)}k_\beta(\alpha)}$$

Where, $u_p(t)$ represents the load-point displacement, $C(\alpha)$ is the compliance of the specimen under test and $k_\beta(\alpha)$ is a non-dimensional factor which depends on the values of α and β. The values of both $C(\alpha)$ and $k_\beta(\alpha)$ for different cases can be found in Guinea *et al* [95].

Rubio *et al* [85] made a straightforward assumption that the value of load-point displacement was equal to the displacement of the impacting end of the incident bar. This is only possible if the specimen and input bar remain in constant contact.

- **CMOD Method** (Rubio *et al* [85], *Experimental Mechanics* [*2003*])

Kishimoto *et al* [96] proposed the formula to calculate the K_{IC} for Quasi-Static Three Point Bend Experiments. Assuming the relation also holds true in the dynamic regime Rubio *et al* [85] proposed the following equation to quantify the K_{ID}:

$$\boldsymbol{K_{ID} = \frac{E w_m}{4\sqrt{a\alpha}} \frac{k_\beta(\alpha)}{v_\beta(\alpha)}}$$

Where, w_m is the value of the Crack-Mouth Opening Displacement (CMOD), E is the value of the Young's Modulus of the specimen under testing, $k_\beta(\alpha)$ and $v_\beta(\alpha)$ are two non-dimensional parameters depending on the values of α and β. The values of both $v_\beta(\alpha)$ and $k_\beta(\alpha)$ for different cases can be found in Guinea *et al* [95].

- **Plastic Zone Size Method** (Anderson and Rosakis, *Experimental Mechanics* [*2006*])

The equation proposed by Anderson and Rosakis taking the Plastic Zone Size near the crack tip into account is as follows:

$$\boldsymbol{r_p = \frac{1}{2\pi}\left(\frac{K_{ID}}{\sigma_{YS}}\right)^2}$$

Where, σ_{YS} is the Yield Stress of the sample under test and r_p is calculated at the point of crack initiation and the point of initiation of crack is determined using the high-speed camera images. According to Anderson and Rosakis the yield stress typically depends on strain rate, the crucial plastic zone size also depends on the rate at which crack tips are loaded and the pace at which they spread, with the latter influence predominating for growing cracks.

All the aforementioned methods are taken as the basis of K_{ID} quantification in the current study.

Chapter 4

RESULTS

This chapter covers the microstructures of the different compositions of Ti-64-xB alloys followed by the Micro-Hardness test results for the same. Later in the chapter, the interpretations from the High-Speed Camera images are presented. The results of the Dynamic Fracture tests conducted at a rate of 10^6 MPa$\sqrt{}$ms^{-1} to 10^7 MPa$\sqrt{}$ms^{-1} on the modified Hopkinson Bar setup is also discussed. Fractographic analysis of the dynamically fractured samples is also presented. The chapter concludes with a discussion of the calculations of the Dynamic Fracture Toughness (K_{ID}) values via different methods (as mentioned in Chapter 3).

4.1 Microscopy

4.1.1 Optical Microscopy

Fig. 4.1 represents the microstructures (Optical Images) of the 0, 0.04, 0.09, 0.3 and 0.55 wt % Ti-6Al-4V-xB alloys. The images indicate a typical lamellar type of microstructure with the α-phase (hcp) and β-phase (bcc) acquiring alternate laths in the Ti-64-xB matrix. In comparison to β laths, the α laths are larger in size and are represented by a lighter colour in the optical images, while the former (β) is darker in contrast and also has a smaller size. The α-hcp, which is tinted lighter is also present at the GBs. These alternate α-hcp and β-bcc laths are positioned along favoured orientations and they almost look like colonies in the Ti-64-xB matrix. Within one prior-β grain, a number of such colonies are present at random. As the solid solubility of Boron in Ti-64 is around 0.02 wt %, anything beyond this wt % will result in the formation of TiB. This can be observed in samples having 0.04, 0.09, 0.3 and 0.55 wt % of Boron. This TiB formed gets oriented at the GBs and have an approximate length of 2 to 5 μm with an elongated framework which almost looks like a cylinder. These objects have a needle like shape and are clearly observable in samples having 0.09, 0.3 and 0.55 wt %. The characteristics observed in the optical images are discovered to be strong accord with the research done by Sen *et al* [59].

4.2 Mechanical Behaviour

4.2.1 Micro-Hardness Testing

Fig. 4.2 shows how hardness varies as the amount of Boron rises in the material. Almost 50 measurements were taken for each sample. If we compare the mean hardness values, we see that hardness increases steadily as Boron wt % increases. Fig. 4.3 represents the % increase in hardness of the Ti-64-xB samples with respect to the 0 B sample. By just 0.04 wt % Boron addition the hardness value went up by approximately 8.2 % and close to 23.5 % as the Boron content increases to 0.55 wt %. The refining of the grains on the addition

of Boron is what causes this increase in hardness. Because there are less TiB particles in the matrix than in other Boron-rich samples (0.09, 0.3 and 0.55), there is a significant range in the hardness values for the 0.04 B sample. As the reported hardness values for TiB particles are around 700 VHN (As reported by Sen *et al* [59]), hardness measurements done in areas where TiB particles are abundant will provide higher values, whereas hardness measurements taken in areas where TiB particles are scarce will produce lower values. Overall, the improvement in hardness is a result of both refined grain size and the presence of TiB particles.

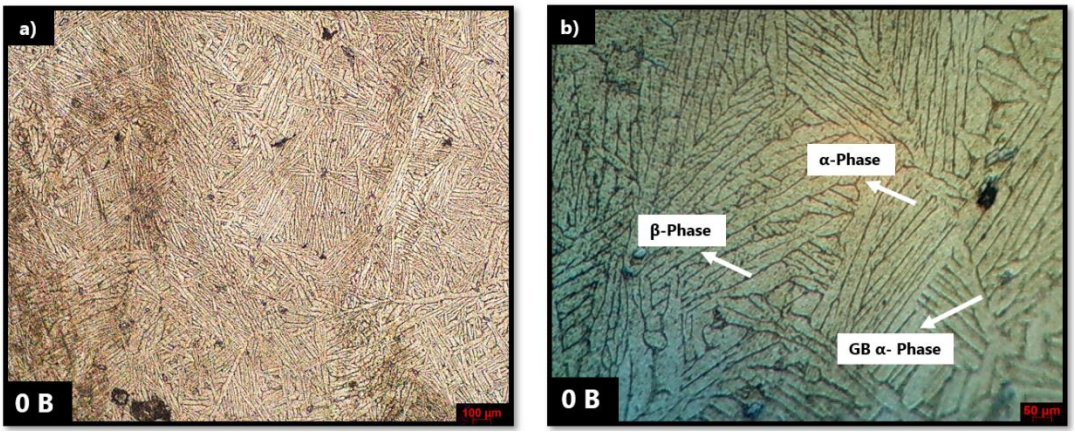

a) 0 B

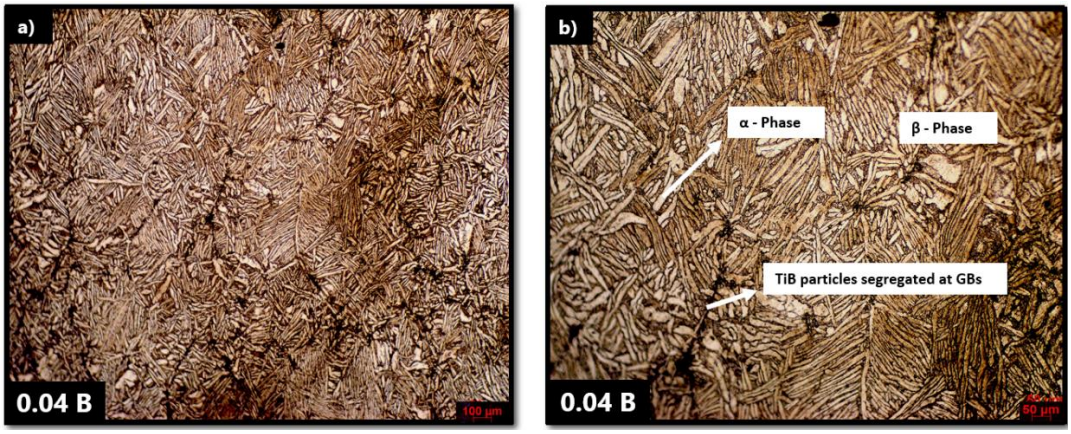

b) 0.04 B

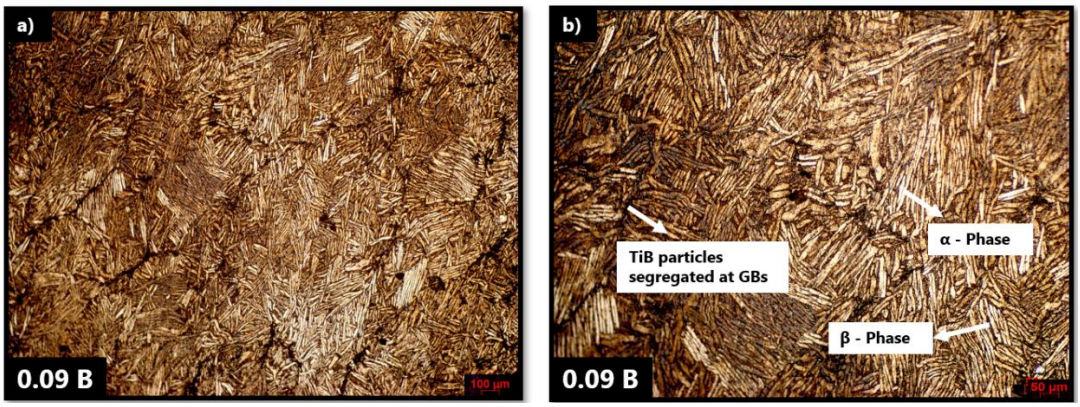

c) 0.09 B

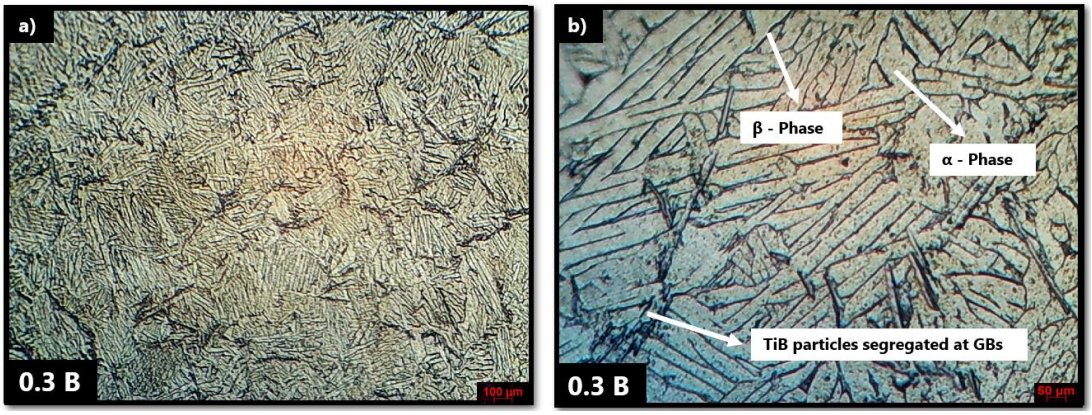

d) 0.3 B

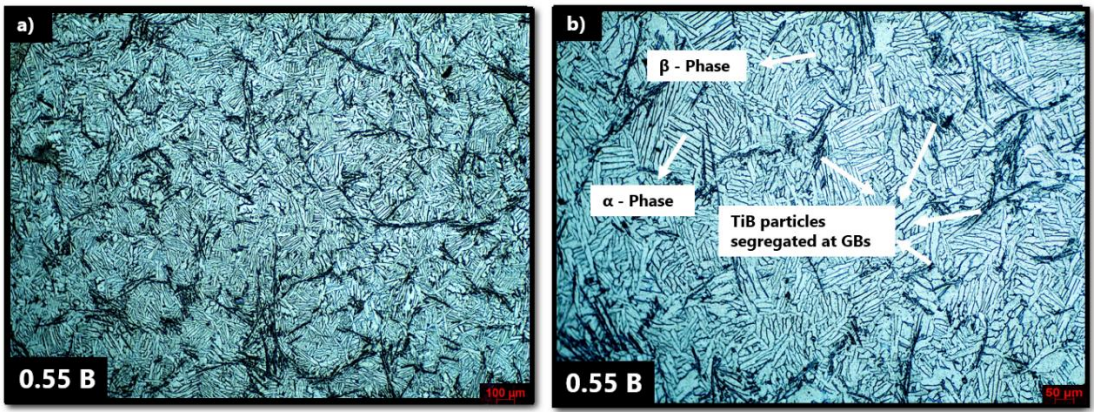

e) 0.55 B

Fig 4.1: Optical Microscopy Images of Ti-64-xB alloys where x is **a)** 0 B **b)** 0.04 B **c)** 0.09 B **d)** 0.3 B and **e)** 0.55 B (All compositions are in wt %)

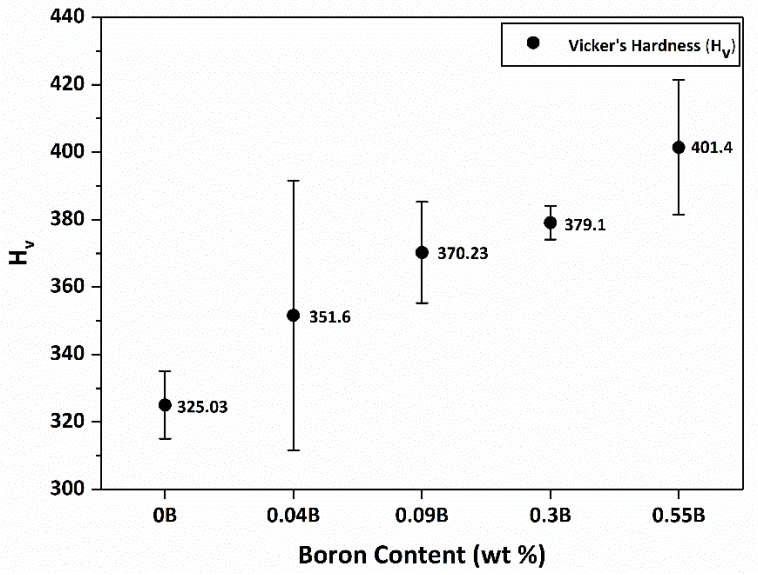

Fig 4.2: Variation in Vicker's Hardness values with increasing Boron content

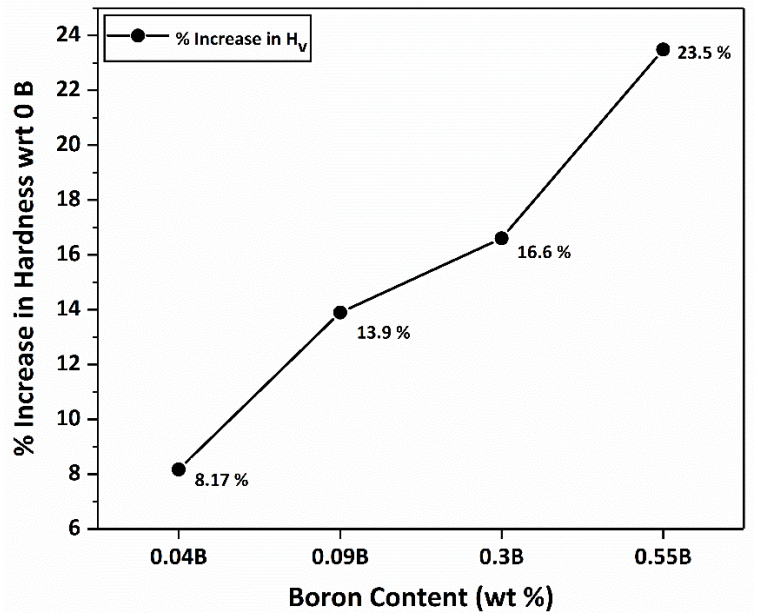

Fig 4.3: Percentage increase in Hardness of Ti-64-xB samples wrt. 0 B sample

4.2.2 High-Speed Camera Interpretations

4.2.2.1 Crack Mouth Opening Displacement (CMOD)

a) Variation in CMOD with time

Using the Phantom High Speed Camera Facility available at IIT-Hyderabad and with the help of the CV 3.7 Software the Dynamic Fracture videos of the samples were analysed and the CMOD values at the time of crack-initiation were measured. For the 0 B sample the CMOD value was found out to be 0.3704 mm. For the 0.04B sample the CMOD value were 0.4167 mm and 0.3701 mm for the impact speeds of 11.69 ms^{-1} and 10.39 ms^{-1} respectively. The CMOD values for the 0.09B were 0.375 mm and 0.3997 mm for the impact speeds of 10.79 ms^{-1} and 11.55 ms^{-1} respectively. For the 0.3B and 0.55B samples the CMOD values were 0.3747 mm and 0.4583 mm (at 10.74ms^{-1} and 12.07ms^{-1}) and 0.4 mm and 0.4396 mm (at 11.9ms^{-1} and 12.37ms^{-1}) respectively. Fig. 4.4 also shows the Frame-by-Frame CMOD plots for the various samples.

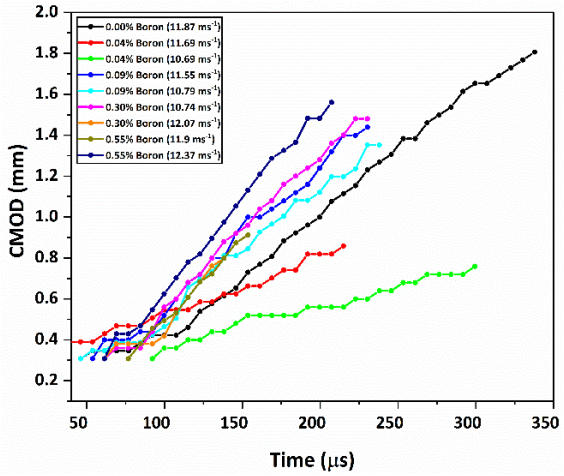

Fig 4.4: Frame-By-Frame CMOD variation for different Ti-64-xB samples (Master Plot)

Table 4.1 summarises the CMOD values for different samples tested at different impact speeds.

Boron Content (in wt %)	Impact Speeds (in ms^{-1})	CMOD Values (mm)
0	11.87	0.37
0.04	10.39	0.37
	11.69	0.42
0.09	10.79	0.38
	11.55	0.40
0.3	10.74	0.37
	12.07	0.46
0.55	11.9	0.4
	12.37	0.44

Table 4.1: Variation in CMOD at the time of Crack-Initiation for different Ti-64-xB samples at different impact speeds

b) Variation in CMOD with impact velocity

Fig. 4.5 represents the variation in CMOD observed for samples tested at two different impact speeds (samples except the 0 B one). The inferences obtained after analysis the High-Speed Camera images are as follows:

- **0.04B Sample:** For both the samples of 0.04 B we observe a similar trend in CMOD with time, the only difference is that the sample tested at a higher impact speed exhibited higher CMOD value as compared to the one tested at a lower impact speed. Fig. 4.5 (a) represents the aforementioned fact.
- **0.09B Sample:** In this case also we see a similar trend for the variation of CMOD with time. But we cannot comment on the variation of CMOD with impact speed because the plots for both impact speeds almost coincide depicting no relation between CMOD and impact speed. Fig. 4.5 (b) supports the following fact.
- **0.3 B Sample:** For the 0.3 B sample we observe that the sample tested at a higher impact speed fractured very quickly as compared to the one tested at a lower impact speed. The former one fractured after 150 μs while the latter took around 250 μs to do so. This clearly indicated that Brittle Fracture prevailed in samples having higher Boron content and there was an overall effect of the Sharp Brittle Fracture and Higher Impact Speed which led to an early fracture for one of the samples. Fig. 4.5 (c) supports the following interpretation.
- **0.55 B Sample:** We observe similar trend for CMOD for both the samples. The sample tested at a higher impact speed showed higher CMOD value as compared to the one tested at a lower speed. Fig. 4.5 (d) represents the aforementioned fact.

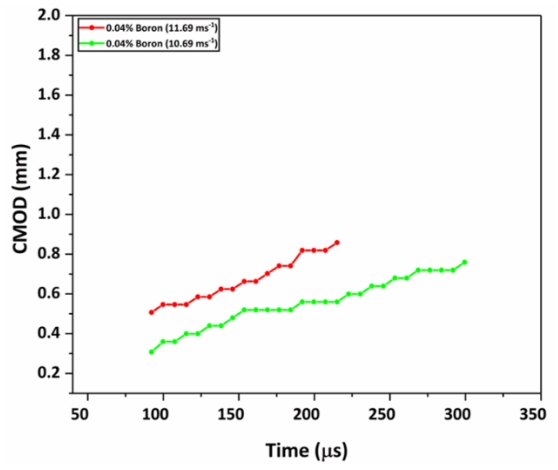

a)

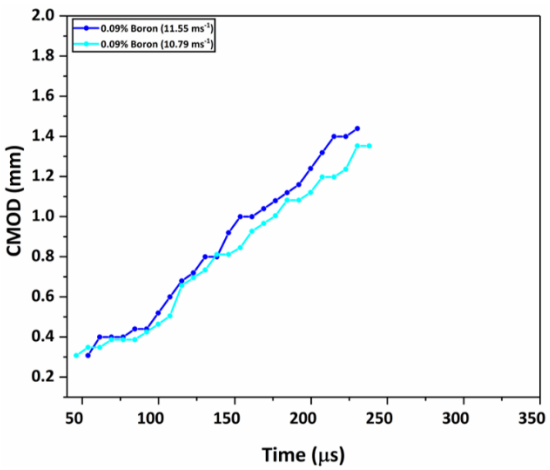

b)

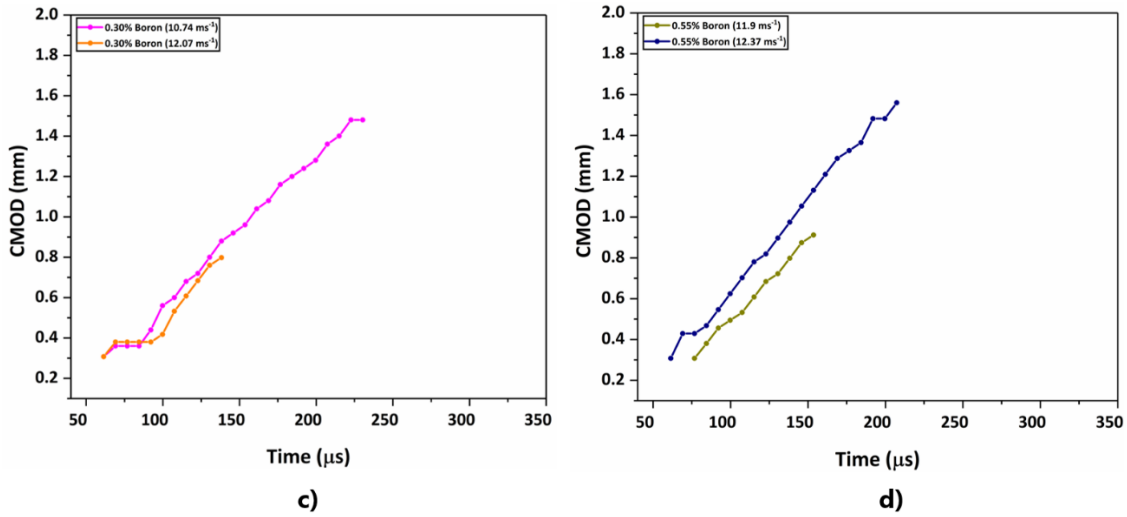

Fig 4.5: CMOD comparison of **a)** 0.04 B **b)** 0.09 B **c)** 0.3 B and **d)** 0.55 B Samples with variation in impact speeds

c) Variation in CMOD with Boron Content

Fig. 4.6 represent the comparison of CMOD values of different Ti-64-xB samples (0.04, 0.09, 0.3 and 0.55) with the one containing no Boron at all. It has been observed that the highest CMOD for the sample having 0B was 1.8067 mm whereas the highest value for samples having 0.04B ranges from 0.7594 mm to 0.858 mm. this indicates as the boron content rises to 0.04 wt. % the CMOD value reduces by about 50 %. The highest CMOD 0.09B ranges from 1.3521 mm to 1.4388 mm which is nearly 23 % lesser than 0B. The curves are also a bit steeper for 0.09B which means the rate of increase of CMOD is higher for 0.09B as compared to 0B. The CMOD values for 0.3 B and 0.55 B are 18 % and 14 % lesser than 0 B samples. So, it can be inferred from the plots that as the Boron content increases the Crack Mouth Opening Displacement values decreases. Fig. 4.7 also summarises the % decrease in CMOD with increasing Boron Content.

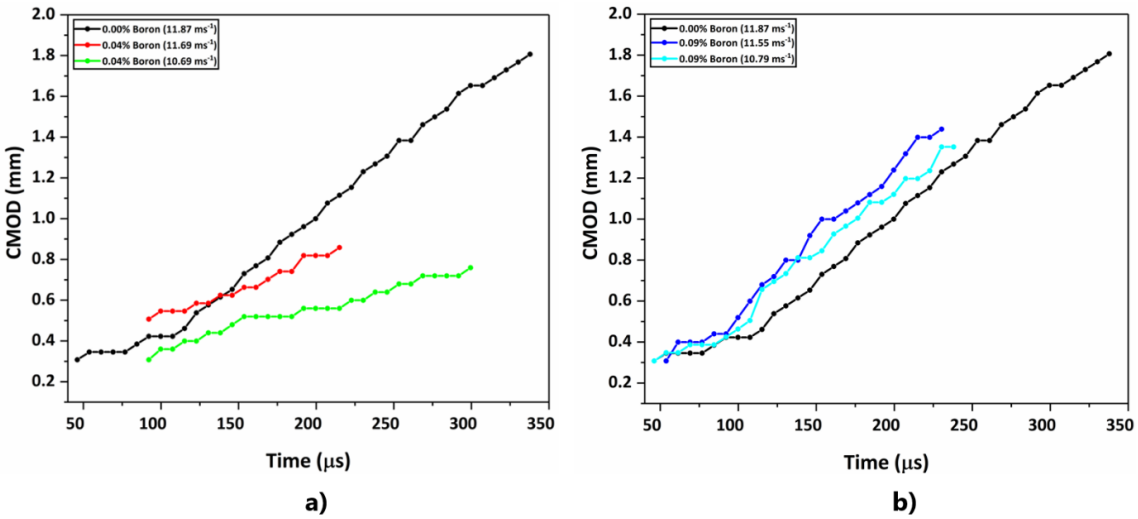

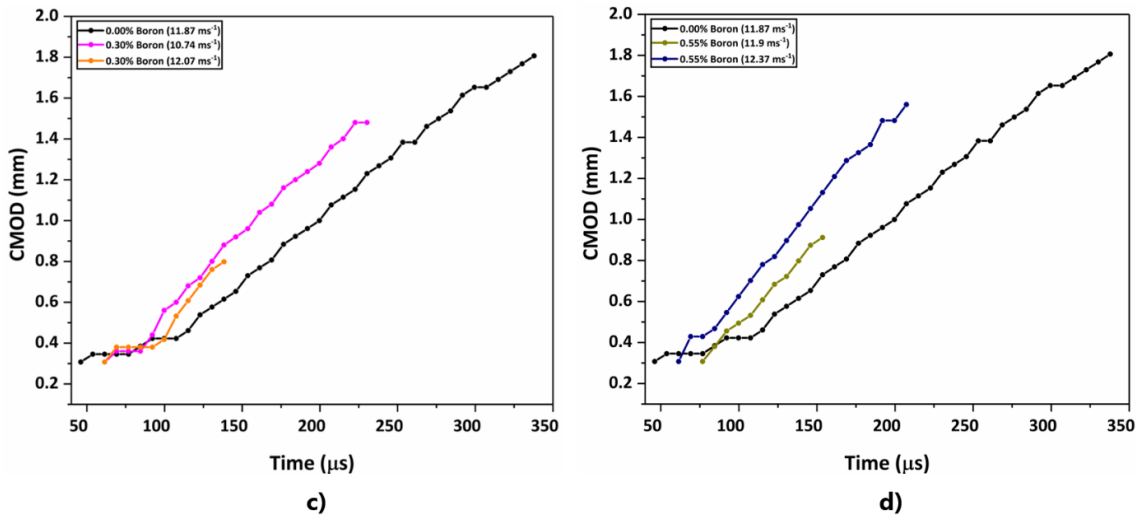

Fig 4.6: CMOD comparison of 0 B sample with **a)** 0.04 B **b)** 0.09 B **c)** 0.3 B and **d)** 0.55 B Samples

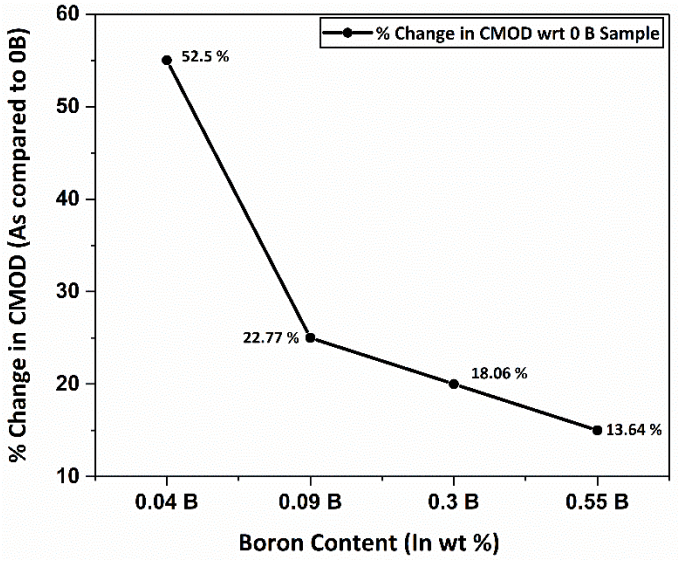

Fig 4.7: % decrease in CMOD of various Ti-64-xB samples wrt 0 B

4.2.2.2 Crack Tip Opening Angle (CTOA)

With the help of the Phantom CV 3.7 Software the Crack-Tip Opening Angles for different Ti-64-xB samples were measured. It was observed that the CTOA values decrease from 17.3° for the 0 B sample to 8.47° for the 0.55 B sample. Fig. 4.8 represents the measured CTOA values from the High-Speed Camera videos and the steady decreasing trend of CTOA with increasing Boron content is summarised in Fig. 4.9.

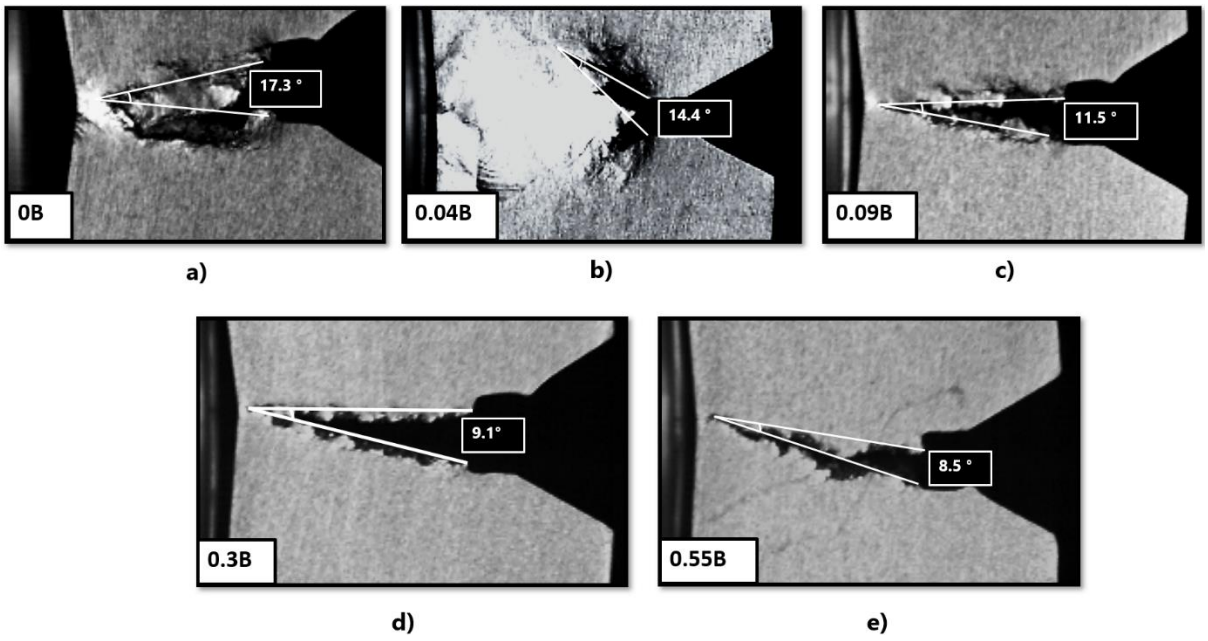

Fig 4.8: CTOA values measured for various Ti-64-xB samples using High-Speed Camera Images

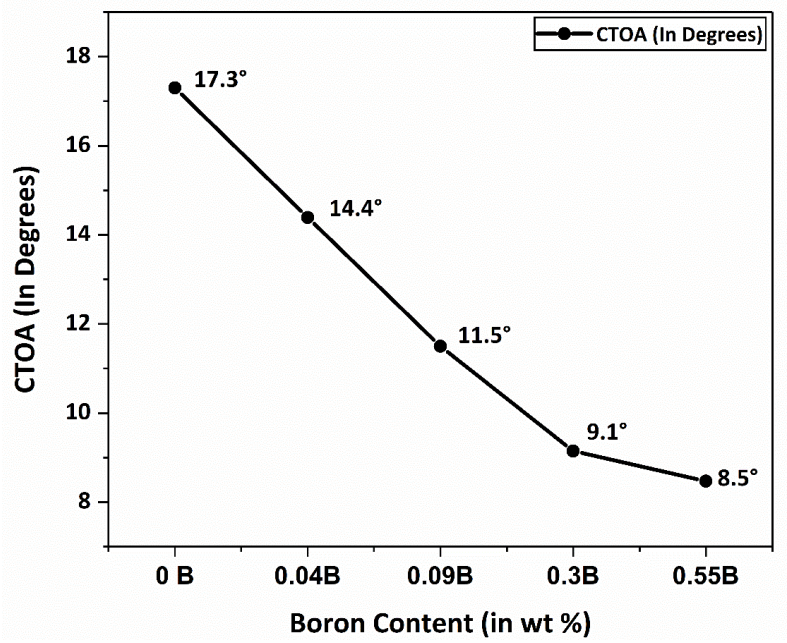

Fig 4.9: Variation of CTOA with increasing Boron content

4.2.2.3 Load Point Displacement ($u_p\ (t)$)

The load-point displacement values were calculated according to the concepts given by Rubio *et al* [85] which are already mentioned in the Methodology chapter. It was observed that for the samples tested at two different impact speeds, the sample tested at a higher speed exhibited a higher Load-Point Displacement value as compared to the one tested at a lower impact speed. Fig. 4.10 represents the schematic to calculate the Load-Point Displacement values using the High-Speed Camera videos.

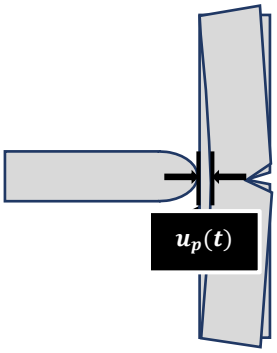

Fig 4.10: Schematic representing the Load-Point Displacement in 1B/3PB test samples

It was observed that the 0.04 B samples showed the highest values for Load-Point Displacement as compared to other Boron rich samples. The values dipped as the Boron content increased. Although, the values for other Ti-64-xB samples were higher than the 0 B sample. The analysis done proves to be in good agreement with the studies done by Sen *et al* [59] as they reported a sudden increase in ductility up to 0.05 wt % followed by a steep dip. The values for Load-Point Displacement also exhibit the same, the 0.04 wt % Ti-64-xB sample had the highest ductility leading to a very high value of Load-Point Displacement then a sudden dip occurred. The calculated values for Load-Point Displacement are summarised in Table 4.2.

Boron Content (in wt %)	Impact Speeds (in ms^{-1})	$u_p\ (t))$ (mm)
0	11.87	0.31
0.04	10.39	0.40
	11.69	0.48
0.09	10.79	0.33
	11.55	0.33
0.3	10.74	0.30
	12.07	0.35
0.55	11.9	0.25
	12.37	0.29

Table 4.2: Load-Point Displacement values for various samples wrt. impact speeds

4.2.2.4 Crack Propagation Speed

The crack propagation speed was also calculated using the High-Speed camera images. The following method was used to quantify the crack propagation speed:

- Firstly, with the help of the Phantom CV 3.7 Software the crack length for each sample was calculated
- Also, the time required for the crack to propagate was also noted
- The division of the aforementioned quantities helped in deciphering the crack propagation speed values.

The values calculated for Crack Length, Time and the Crack Propagation Speed are summarised in Table 4.3.

Boron Content (wt %)	Crack Length (mm)	Time required (µs)	Crack Propagation Speed (ms^{-1})
0 B	6.1	245.72	24.83
0.04 B	1.87	299.46	9.47
0.09 B	5.68	142	39.98
0.3 B	5.80	138.22	41.94
0.55 B	6.14	99.82	63.96

Table 4.3: Crack Propagation Speed values for various Ti-64-xB samples

The 0.04 B sample showed an anomalous behaviour here also like in the case of Load-Point Displacement. The High-Speed Camera images clearly depicted that the 0.04 B samples did not fracture which is evident from the values for crack length. After the 0.04 B sample, as the Boron content increased the Crack length also increased and the time required for the crack to propagate decreased. This clearly indicated the presence of Brittle character in the Boron rich samples pertaining to a sharp and quick crack propagation. Fig. 4.11 represents the variation of crack propagation speed with respect to the increasing Boron content.

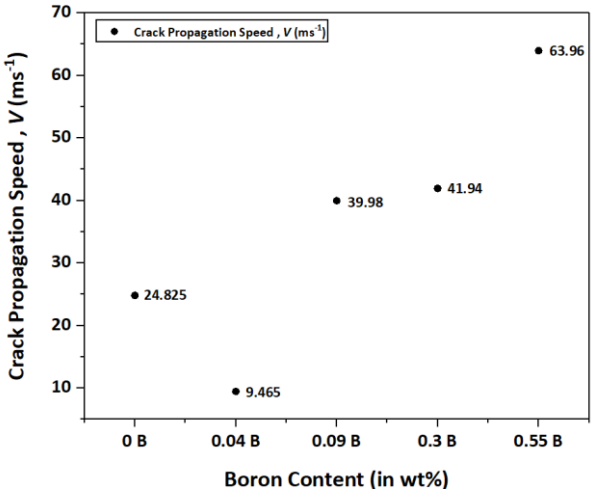

Fig 4.11: Variation of Crack Propagation Speed with increasing Boron Content

Frame-By-Frame Crack lengths were calculated where each frame represented the time required for the crack to propagate up till that frame. The variation of crack length with time is represented in Fig. 4.12. This calculation eventually gave the variation of crack propagation speed with time (Fig. 4.13). The samples having the same composition showed similar trends for crack propagation speed with time, the only difference being that: the sample tested at a higher impact speed exhibited a higher crack propagation speed as compared to the one tested at a lower speed. It is also observed that as the Boron content increases the curves for crack propagation speeds and the crack length become more steeper and steeper.

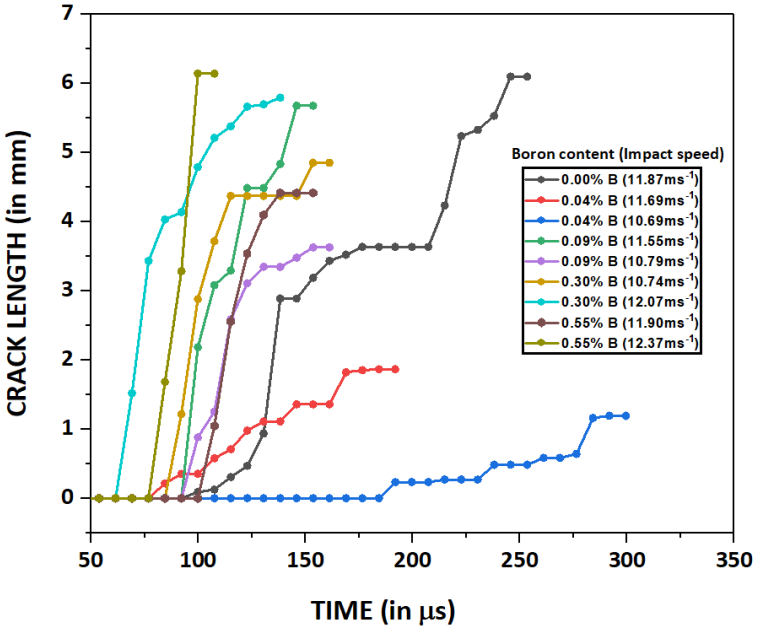

Fig 4.12: Frame-By-Frame Crack Length variation with time

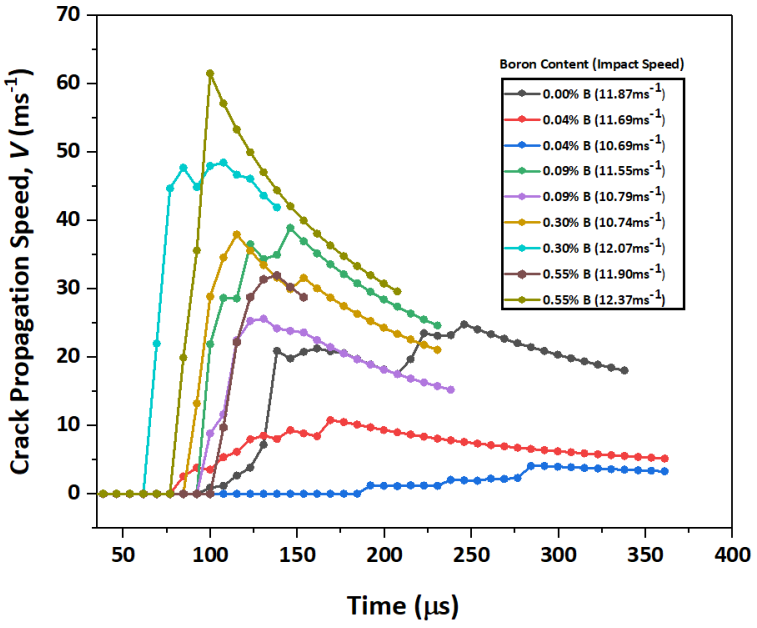

Fig 4.13: Frame-By-Frame Crack Propagation Speed variation with time

4.2.3 Fractography

Fractography of the Dynamically Fractured Samples was performed. It was observed that the Ti-6Al-4V-0B sample showed Ductile Fracture features like Equi-Axed and Conical Dimples along with Serpentine Glides. The observed features are in close agreement with the studies done by Roy *et al* [97], where they studied the deformation of the Ti-64-0.1B sample at a strain rate which falls in the Quasi-Static regime. Other features like Sheared (also observed in Muiruri *et al* [98]) and Elongated Dimples (as in Alaghmandfard *et al* [44]) when viewed at higher magnifications (~ 1200X) along with some micro-voids (as in Roy *et al* [97]). At lower magnifications one could see lath-like features in the fractographs which helps in concluding that the typical fracture mechanism is the **Cleavage Fracture of α-hcp Laths** and this conclusion is supported by the studies done by Sen *et al* [59] for Quasi-Static Fracture. Fig. 4.14 represents the Fractographic Images for the 0 B samples highlighting the evident features along with the literary article info that support the claims made.

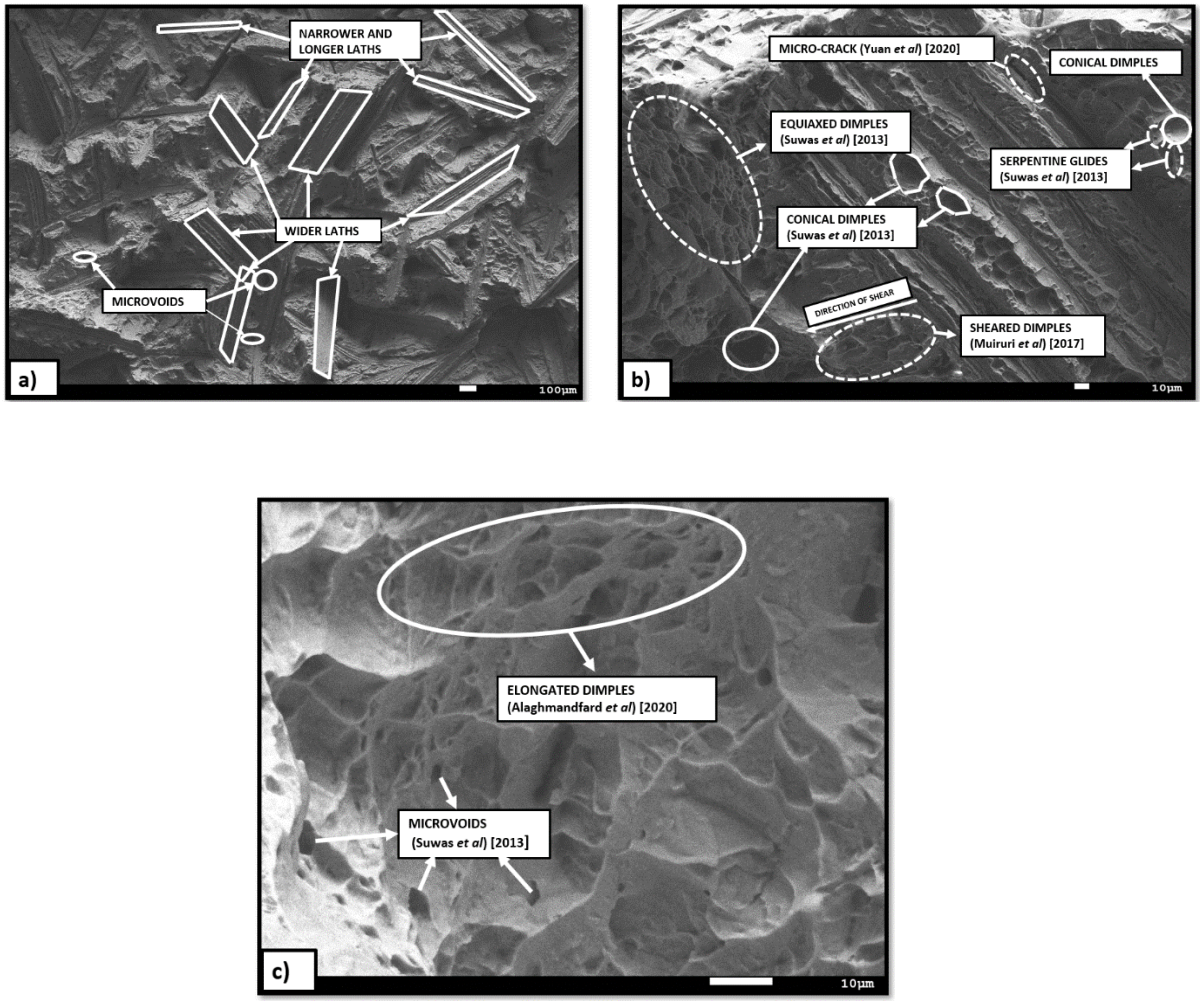

Fig 4.14: Fractographic Images of Ti-64-0B sample highlighting various fracture features

For the 0.09 B samples due to grain size reduction the same α-lath cleavage fracture occurs, the only difference being that the laths are now much smaller in size due to microstructural refinement. Fig. 4.15 represent the typical Fractographs for the Ti-64-0.09B samples highlighting the observable fracture features. One could observe typical brittle fracture features for the 0.09B samples like River and Step patterns (as in Liu *et al* [99]). Cleavage Cracks and Deep Shear Dimples (also observed in Ammar *et al* [100]) are also observed when viewed at higher magnifications. Very few Equi-axed dimples are also observed at some places.

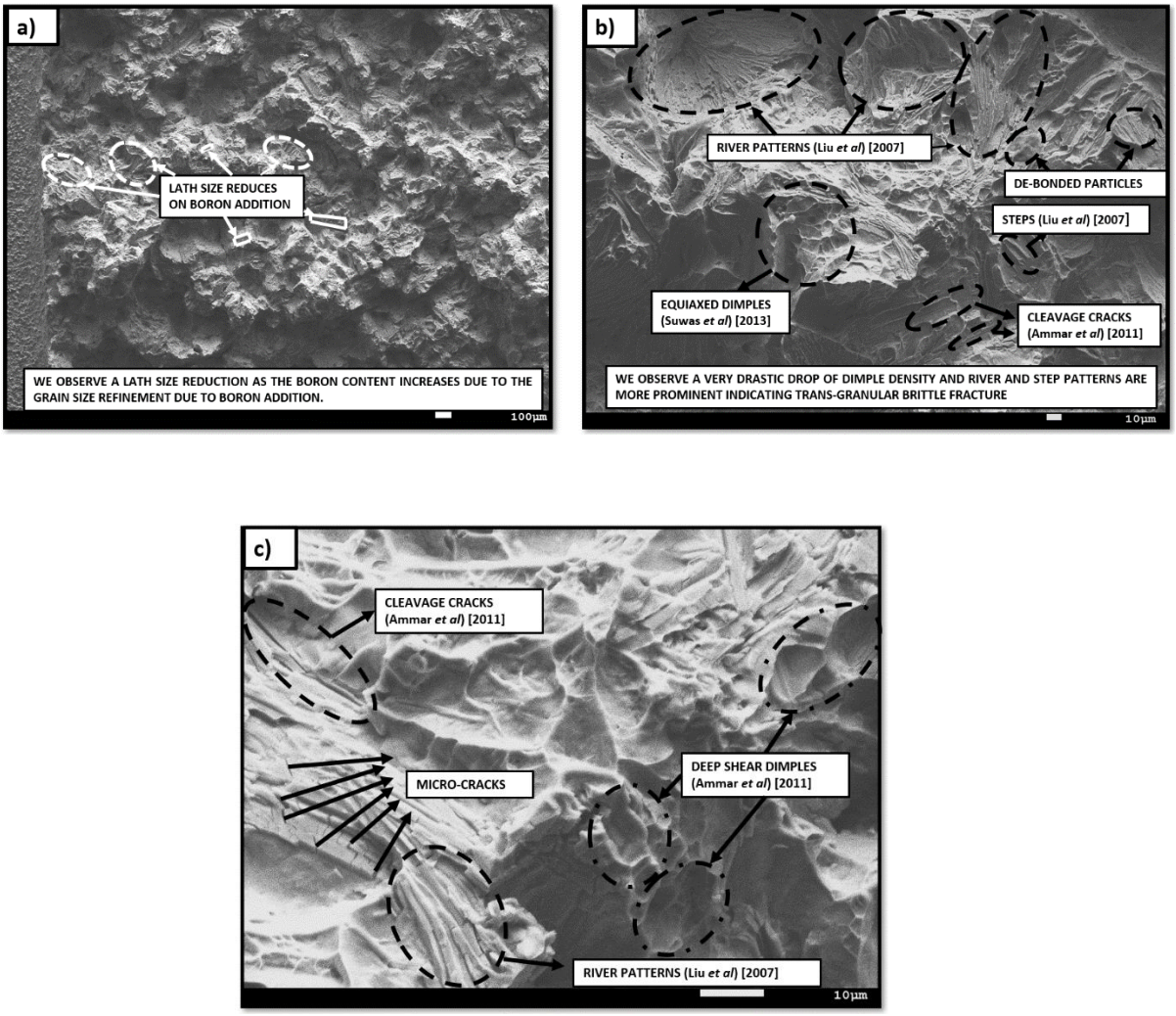

Fig 4.15: Fractographic Images of Ti-64-0.09B sample highlighting various fracture features

For the 0.3 B samples there is a further size reduction in the cleavage fractured α-laths due to increased microstructural refinement with increasing Boron content. The River patterns become even more pronounced here and one could observe dominating Step patterns at higher magnifications which is in good agreement with the studies performed by Lu *et al* [101]. Fig. 4.16 represent the typical Fractographs for the Ti-64-0.3B samples highlighting the observable fracture features.

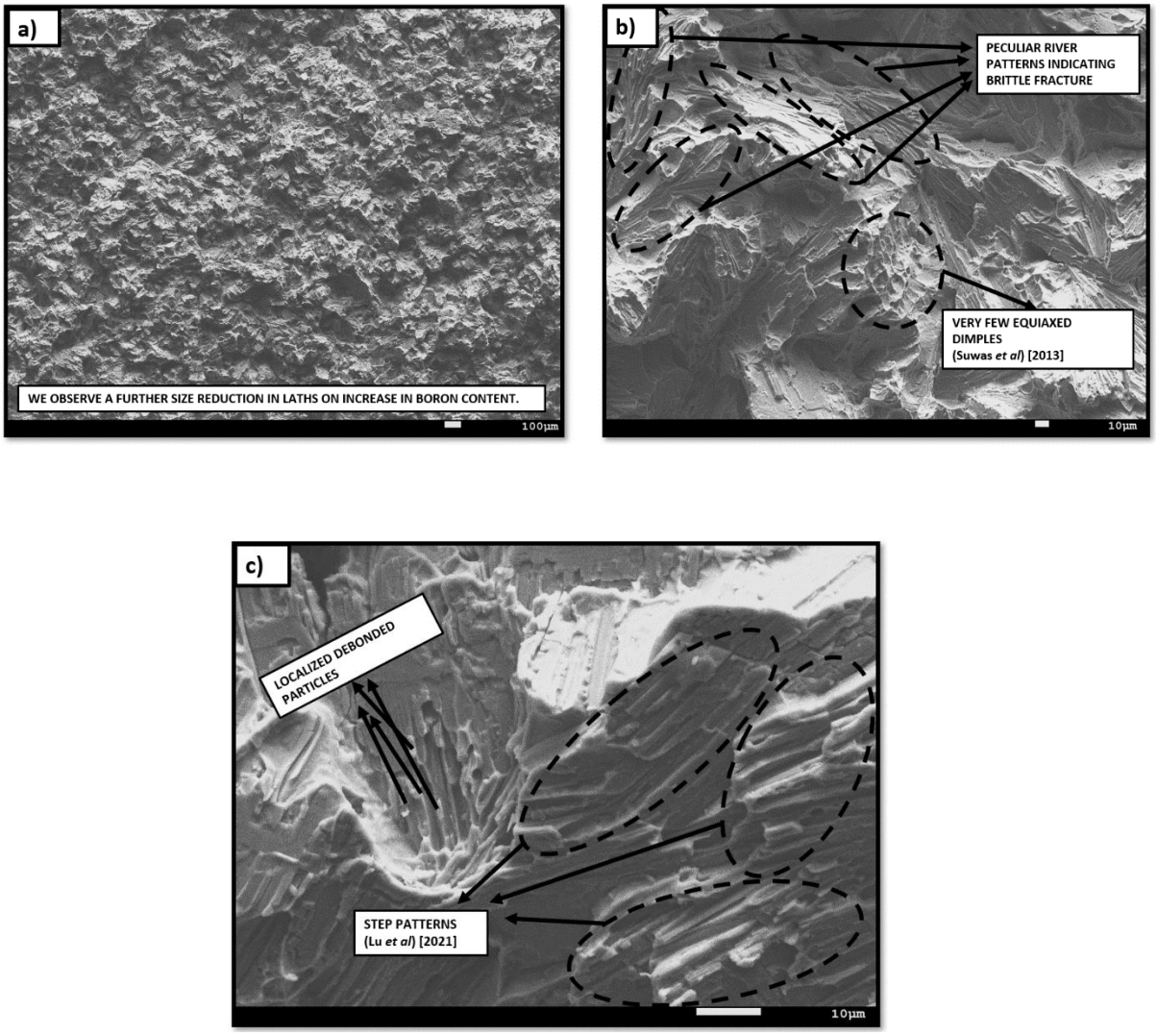

Fig 4.16: Fractographic Images of Ti-64-0.3B sample highlighting various fracture features

For the 0.55 B samples there is no significant decrease in the cleavage fracture laths as there is not much difference in the size of α-lath on further addition of Boron to Ti-64. So, no observable difference in fractured lath size is exhibited at lower magnifications (Fig. 4.17 (a)). Similar Cleavage Cracks and Facets are observed (as in Ammar *et al* [100]). Because of the drastically fine grain size, some smooth patches can also be seen which is

in good agreement with the studies done by Yao *et al* [102]. River and Step patterns indicating Trans-granular Brittle Fracture were the most prominent features for these samples. Very few Equi-axed Dimples are also observed at higher magnifications due to the abundance of TiB particles at grain boundaries forming a necklace like structure and promoting brittle fracture of the α-laths. Fig. 4.17 represent the typical Fractographs for the Ti-64-0.55B samples highlighting the observable fracture features.

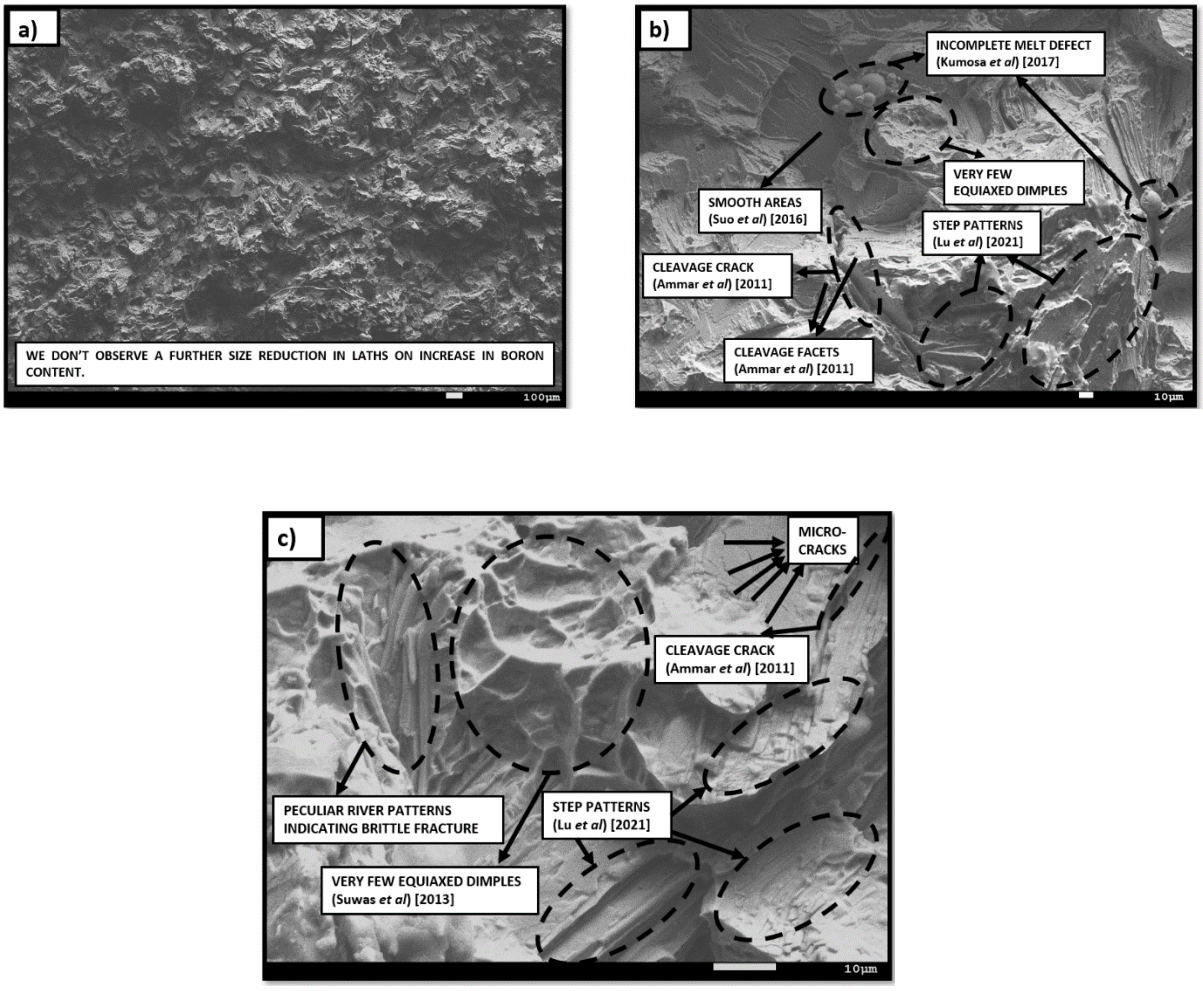

Fig 4.17: Fractographic Images of Ti-64-0.55B sample highlighting various fracture features

It is worth noting that the Fractographic Images for the 0.04 B samples cannot be taken because these samples did not fracture.

4.2.4 Dynamic Fracture Toughness Calculations

After calculating all the parameters proposed by Rubio *et al* [85] (Peak Load, CMOD and Load-Point Displacement) and Rosakis *et al* [24] (Plastic Zone Size) the values for the Dynamic Fracture Toughness (K_{ID}) were calculated using each method and then compared with the Quasi-Static Fracture Toughness (K_{IC}) values proposed by Sen *et al* [59].

a) Dynamic Fracture Toughness using Peak Load ($P(t)$)

A MATLAB tool proposed by Francis *et al* [103] was used to calculate the peak load during the dynamic deformation process (Fig.4.18 represents the interface of the MATLAB tool used). Separate Incident/Reflected and Transmitted Signal Excel files were created and then imported in the MATLAB tool and the Force vs Displacement curves were analysed to get the peak load. Also Force vs Time curves were also studied to check whether the peak load is achieved at the crack initiation time. The High-Speed camera footage supports the theory that the peak load is achieved at the time of crack initiation. Fig. 4.19 represent the Crack-Initiation Force vs Displacement Curves for different Ti-64-xB samples. Fig. 4.20 provides an idea of the load-time history for various samples proving the fact that crack initiation occurs at the Peak Load only.

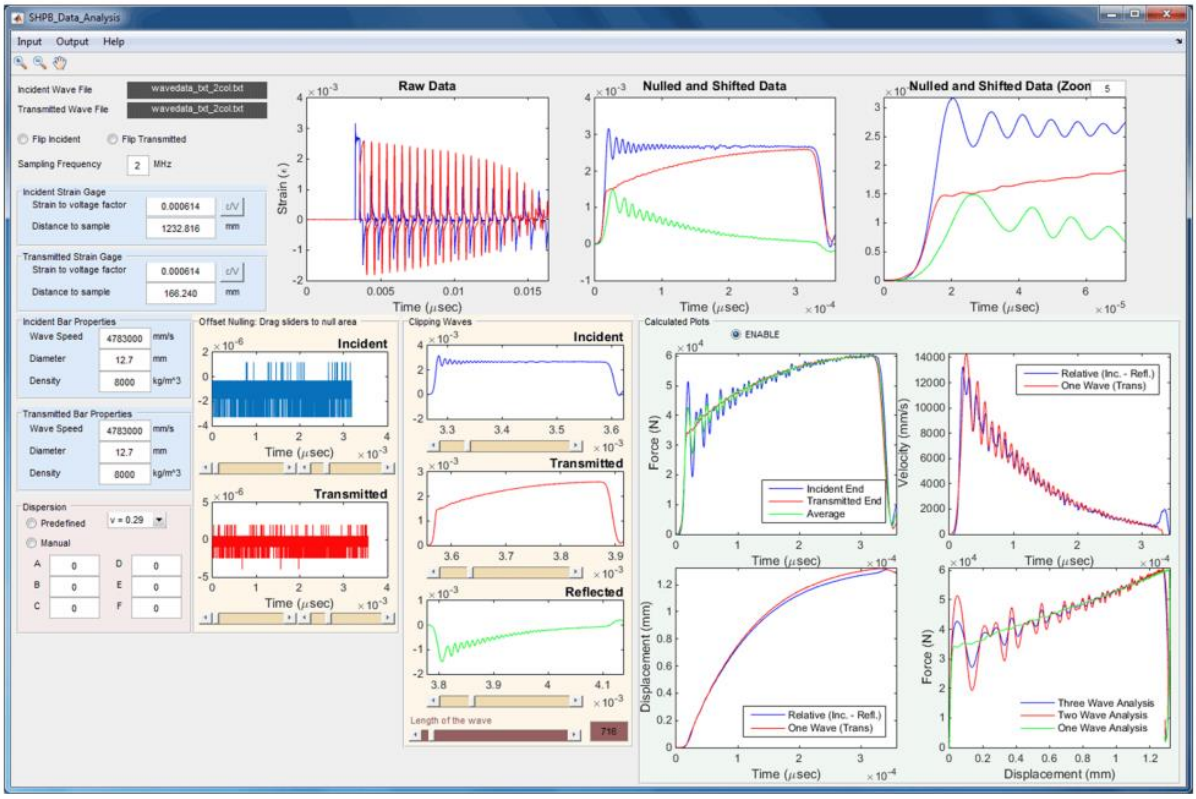

Fig 4.18: Interface of the MATLAB Graphical analysis tool proposed by Francis *et al* [103]

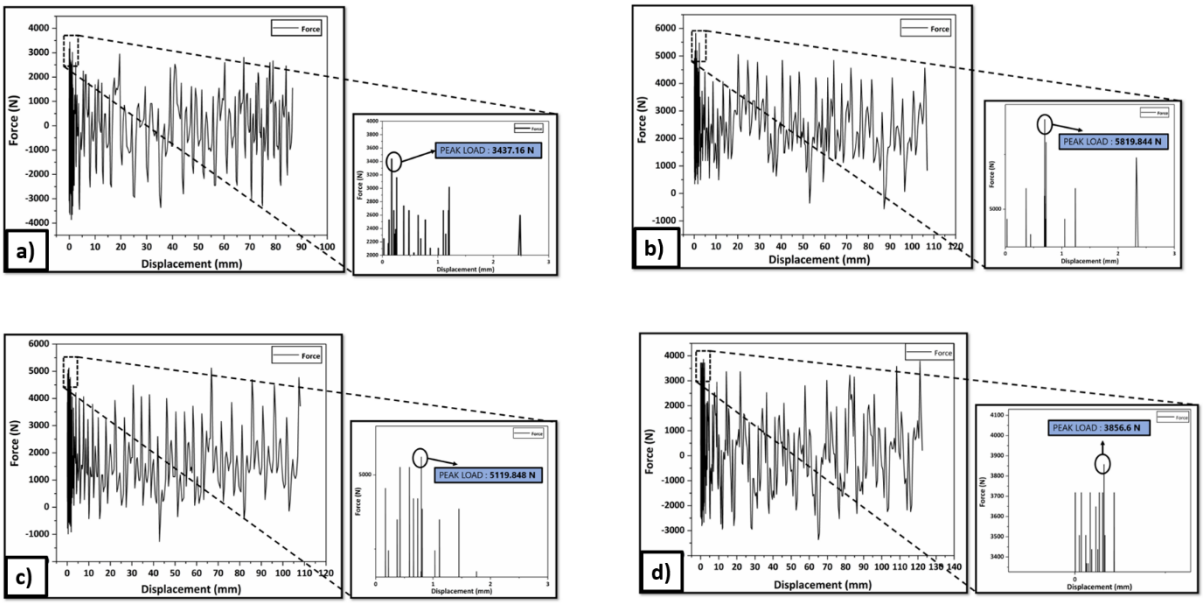

Fig 4.19: Peak Load values obtained for **a)** 0.04 B **b)** 0.09 B **c)** 0.3 B and **d)** 0.55 B

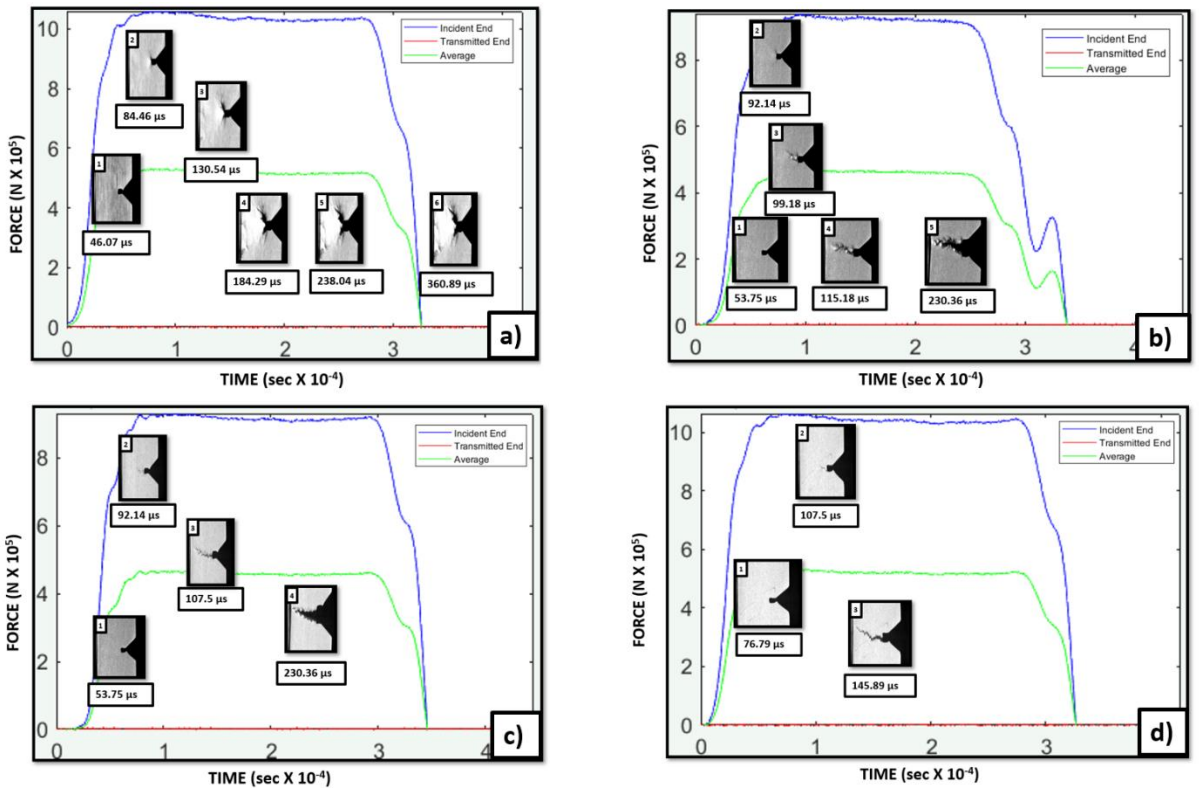

Fig 4.20: The Load-Time history for **a)** 0.04 B **b)** 0.09 B **c)** 0.3 B and **d)** 0.55 B supporting the fact that Crack-Initiation occurs at Peak Load

It has been observed that the peak load values increase from **5819.844 N** for 0.04B to **5119.848 N** for 0.09B and then dips to **3856.6 N** for 0.3B to even lower values of **3437.16 N** for 0.55B. After putting these peak load values in different theories proposed in different literary articles the K_{ID} values were obtained. The three theories used are as follows:

- Acc. to Sahraoui *et al* [104]

$$K_{ID} = \frac{3}{2}\frac{FL}{BW^2}\pi a^{1/2} f(\alpha)$$

Where, $f(\alpha) = [1.11 - 1.55\alpha + 7.71\alpha^2 - 13.53\alpha^3 + 14.23\alpha^4]$

- Acc. to Xiaohe *et al* [105]

$$K_{ID} = \frac{P_Q S}{BW^{3/2}} f(\alpha)$$

Where, $f(\alpha) = \alpha^{1/2}[2.9 - 4.6\alpha + 21.8\alpha^2 - 37.6\alpha^3 + 38.7\alpha^4]$

- Acc. to Shazly *et al* [106]

$$K_{ID} = \frac{P_Q}{BW^{1/2}} f(\alpha)$$

Where, $f(\alpha) = \frac{3\beta\sqrt{\alpha}}{2(1+2\alpha)(1-\alpha)^{3/2}}[1.99 - \alpha(1-\alpha)(2.15 - 3.93\alpha + 2.7\alpha^2)]$

Fig. 4.21 represent the K_{ID} values obtained using the aforementioned theories. It was observed that the 0.04 B sample exhibited the highest value of K_{ID} for all of the three proposed theories. Theories proposed by Xiaohe *et al* [105] and Shazly *et al* [106] almost showed identical values whereas the values calculated using Sahraoui *et al* [104] were a bit on the higher side.

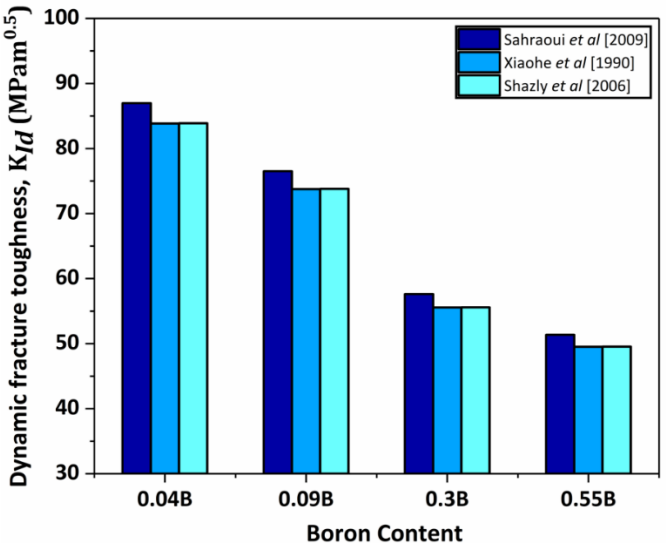

Fig 4.21: K_{ID} values calculated using Peak Load

b) Dynamic Fracture Toughness using CMOD

Using the High-Speed Camera Images the Crack-Mouth Opening Displacement was calculated and the quantification of K_{ID} was done according to the concepts proposed by Rubio *et al* [85] for CMOD. The CMOD values calculated are already mentioned in Table 4.1 and the proposed theory was mentioned in the Methodology Chapter (Chapter 3). Fig. 4.22 represents the Dynamic Fracture Initiation Toughness values according to the CMOD.

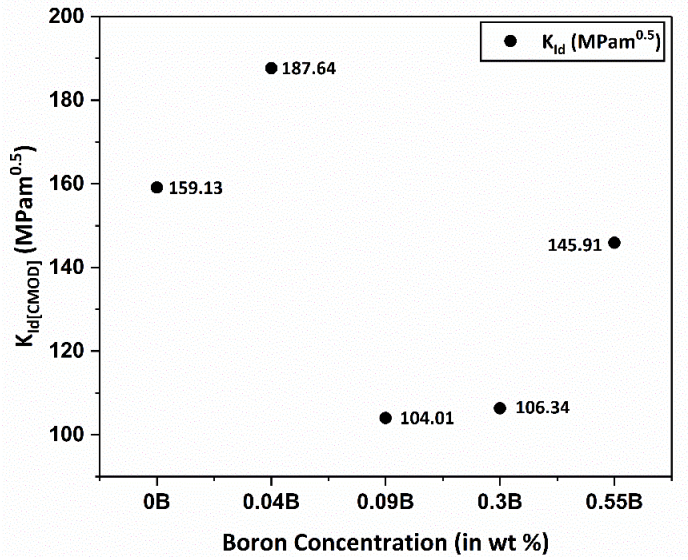

Fig 4.22: K_{ID} values calculated using CMOD

It has been observed that the 0.04 B sample exhibited the highest value for K_{ID} because it had the highest value for CMOD also, among all the other sample.

c) Dynamic Fracture Toughness using LPD

Using the High-Speed Camera Images the Load-Point Displacement was calculated and the quantification of K_{ID} was done according to the concepts proposed by Rubio *et al* [85] for LPD. The LPD values calculated are already mentioned in Table 4.2 and the proposed theory was mentioned in the Methodology Chapter (Chapter 3). Fig. 4.23 represents the Dynamic Fracture Initiation Toughness values according to the CMOD. Table 4.4 summarizes the KID values for different samples at different impact speeds.

Boron Content (in wt %)	Impact Speeds (in ms^{-1})	K_{ID} (MPa$\sqrt{m}$)
0	11.87	70.51
0.04	10.39	98.21
	11.69	117.76
0.09	10.79	77.03
	11.55	77.03
0.3	10.74	74.1
	12.07	84.69
0.55	11.9	63.87
	12.37	74.58

Table 4.4: Variation of $K_{ID[LPD]}$ with impact speed for different Ti-64-xB samples

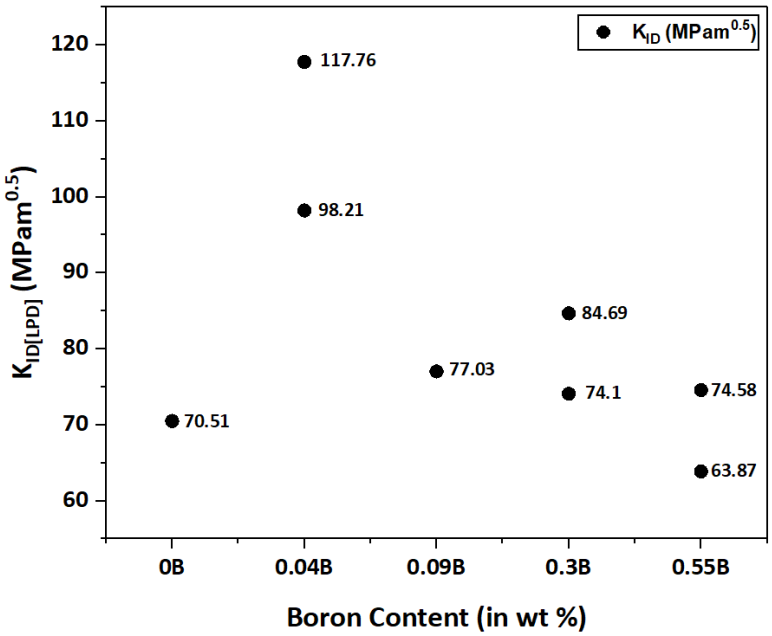

Fig 4.23: K_{ID} values calculated using Load-Point Displacement

d) Dynamic Fracture Toughness using Plastic Zone Size

By changing the filter of the High-Speed Camera Images to Edge HiPass 3X3 or 5X5 in the CV 3.7 software the Plastic Zone Size was measured. The Dynamic Fracture Initiation Toughness values were measured according to the concepts proposed by Anderson and Rosakis [24] (already mentioned in Chapter 3). Fig. 4.24 represents the calculated values for K_{ID} according to the Plastic Zone Size.

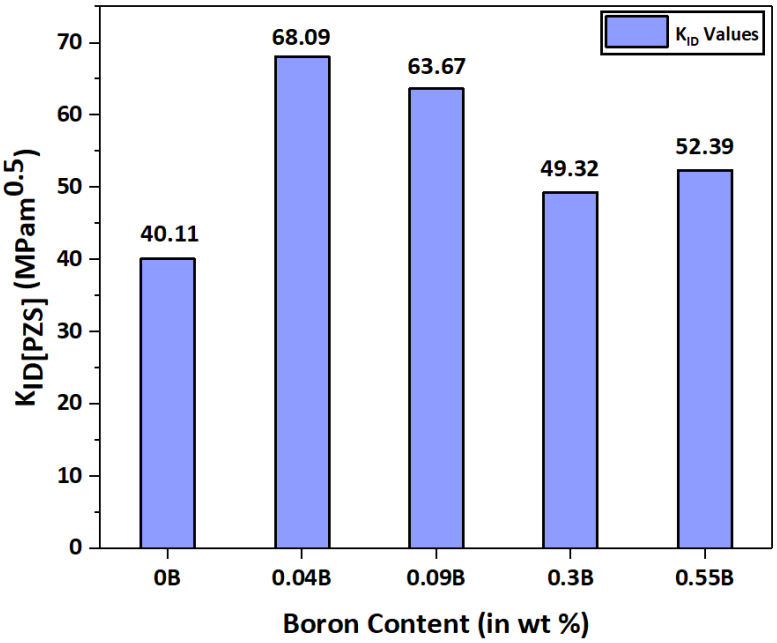

Fig 4.24: K_{ID} values calculated using Plastic Zone Size

e) Dynamic Fracture Toughness Values vs Quasi-Static Fracture Toughness Values

Sen *et al* [59] conducted Quasi-Static tests using Compact-Tension [C(T)] specimens for Ti-6Al-4V-xB (x = 0, 0.05, 0.1 and 0.4 wt %) to calculate the Quasi-Static Fracture Toughness (K_{IC}) values for the same. Fig. 4.25, 4.26, 4.27 and 4.28 basically represents the comparison of the K_{ID} values calculated via different theories in the present study with the K_{IC} values calculated by Sen *et al* [59] just to compare the toughness values in such varying strain-rate regimes.

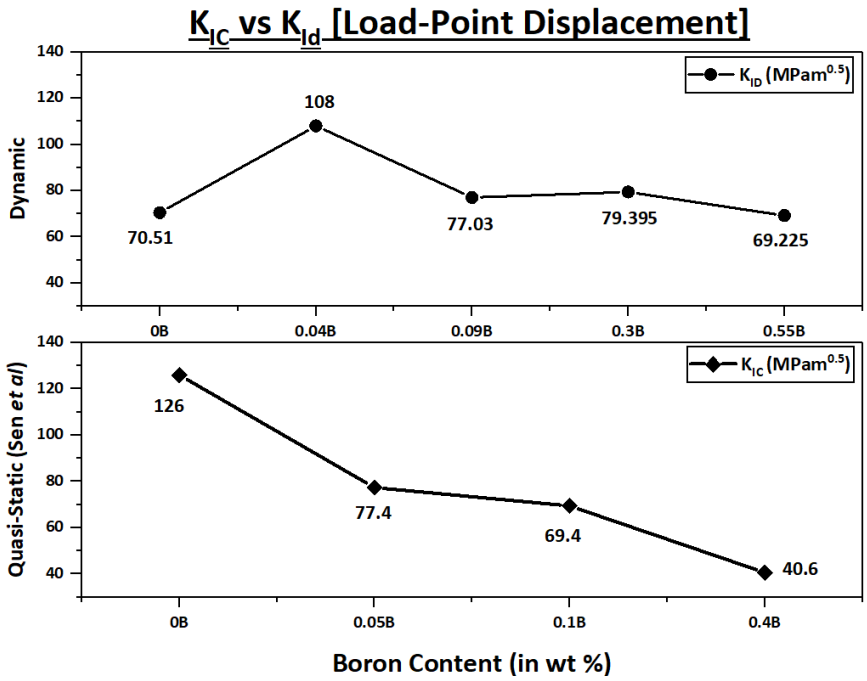

Fig 4.25: K_{ID} values using Load-Point Displacement vs K_{IC} values from Sen *et al* [59]

According to Sen *et al* [59] as the boron content increases the K_{IC} values decreases from 126 MPa√m for 0 B samples to 40.6 MPa√m for 0.4 B sample. In our case we do not see such a trend, we rather observe an increase in the K_{ID} values calculated via Load-Point Displacement method from 70.51 MPa√m for 0 B to 108 MPa√m for 0.04 B and then a dip to 77.03 MPa√m for 0.09 B followed by a slight increase for 0.3 B and finally a dip to 69.225 MPa√m for the 0.55 B sample. The 0.04 B sample shows an anomalous behaviour here (Fig. 4.25).

We observe a similar trend for the K_{ID} values calculated via Crack Mouth Opening Displacement method of the 0.04 B sample as we see a spike from 159.127 MPa√m for 0 B samples to 187.64 MPa√m for the 0.04B sample. After that we see a dip to 104.01 MPa√m for the 0.09B sample and then a slight increase up till 145.91 MPa√m for the 0.55 B sample. (Fig. 4.26).

We observe a dip in the K_{ID} values calculated via Force analysis as we move from 0.04 B to 0.55 B as the values change from 84.894 MPa√m to 50.14 MPa√m respectively. We see a similar trend as we observe for the K_{IC} values stated by Sen *et al* [59].

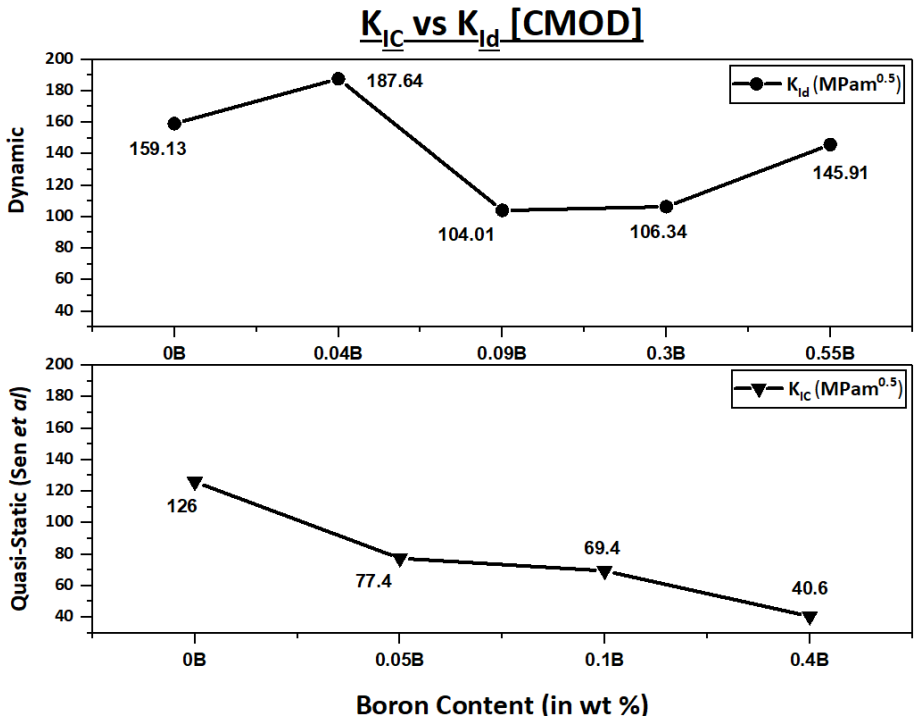

Fig 4.26: K_{ID} values using CMOD vs K_{IC} values from Sen *et al* [59]

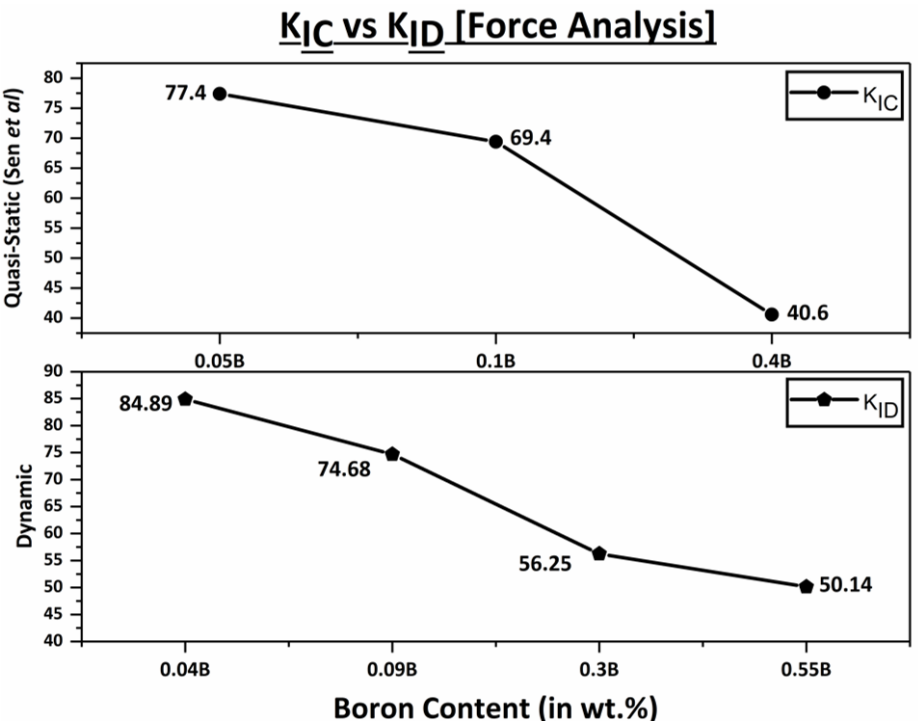

Fig 4.27: K_{ID} values using Force Analysis vs K_{IC} values from Sen *et al* [59]

Fig. 4.28 represents the comparison between K_{ID} values calculated according to the Plastic Zone Size theory and the K_{IC} values proposed by Sen *et al* [59]. Similar trends can be observed here also as in the case of Load-Point Displacement and Crack-Mouth Opening

Displacement. There is a spike in the K_{ID} value from 0 B (40.11 MPa√m) to 68.09 MPa√m for the 0.04 B and then a slight similar dip is observed for other Boron rich samples.

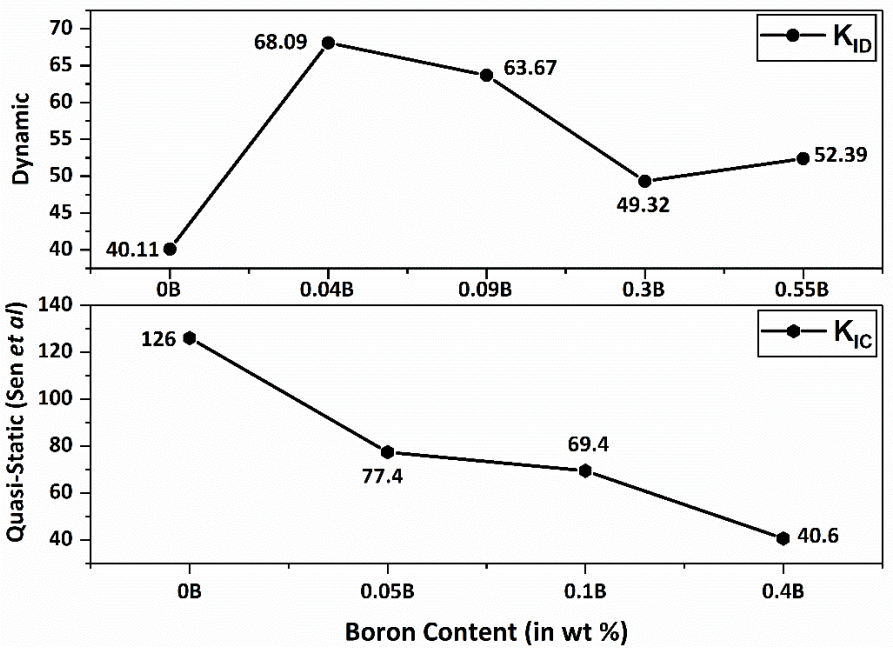

Fig 4.28: K_{ID} values using Plastic Zone Size vs K_{IC} values from Sen *et al* [59]

Chapter 5

Discussions

This upcoming chapter will provide a detailed and in-depth critical analysis of the outcomes that were presented in the previous chapter. The analysis will be conducted with the aim of justifying the results that were obtained from the research. The chapter will comprehensively explore the evidence and arguments presented in the previous chapter, evaluating the strengths and weaknesses of each finding. Additionally, the chapter will provide a discussion of the implications and significance of the results for the field of study. Overall, the upcoming chapter will offer a thorough and detailed analysis that aims to provide a more comprehensive understanding of the findings that were previously presented.

5.1 Discussions on Mechanical Behaviour

5.1.1 Hardness

The present study discovered that as the specimens' Boron contents rose, so did the hardness of the Ti-64-xB samples. The following are some potential causes of this behaviour:

- The existence of TiB particles at the GBs may be one of the factors for this increase in hardness. The microstructures of different Ti-64-xB sample clearly show the existence of TiB (Black in contrast) forming a garland/necklace type of orientation along the GBs. This theory is in good agreement with the study performed by Sen *et al* [59]. Also K. Euh *et al* [69] reported very high hardness values for TiB particles (~ 700 VHN).

- Anthony C. in his book *Nanoindentation* [68] mentions the Tabor's Equation which relates the Vickers's Hardness and the Yield Strength as:

$$\boldsymbol{H_v \sim C_v \sigma_y}$$

  Where, C_v is called as the Constraint Factor and its value depends on the material type, the indenter type and other criterions related to the experiment. Anthony C. [68] also reports that the experiments show that the value of C_v is nearly equal to 3 for materials having a very high ratio of Young's Modulus (E) to the Yield Strength (Y) i.e., E/Y ratio (Like in the case of Metals). So, as the value for C_v is fixed (3) then Vickers's Hardness depends directly on the Yield Strength of the material. As, the Yield Strength of the material increases due to micro-structural refinement (also reported by Sen *et al* [59]) the Vickers's Hardness values also increase.

- Sen *et al* [59] also developed some empirical relations for Boron modified as-cast Ti-64 based on the concepts of the Hall-Petch relation, relating the α-hcp and β-bcc lath size with the Vickers's Hardness values as follows:

$$H_v = 302.1 + 883.4\left(d_\beta\right)^{-1/2}$$
$$H_v = 188.6 + 369.2\ \left(d_\alpha\right)^{-1/2}$$

Where, d_β and d_α denote the α-hcp and β-bcc lath sizes respectively. Boron addition leads to grain size reduction which in turn leads to a decrease in the lath sizes, eventually increasing the Hardness values.

5.2 Discussions on High-Speed Camera Image Findings

5.2.1 Crack-Mouth Opening Displacement (CMOD)

- **Variation with Impact Speed:** It was observed that samples tested at varying impact speeds (0.04, 0.09, 0.3 and 0.55 wt. %) showed variations in the values for CMOD as well. The ones tested at higher speeds reported higher values for CMOD as compared to the one tested at a lower speed (Table 4.1). This is due to the fact that, with a higher impact speed of the striker bar the wave generated in the incident bar and eventually the 1B/3PB specimen will have a higher amplitude leading to a much higher amount of destruction near the crack tip causing the Crack Mouth to open a bit wider leading to higher CMOD values.
- **Variation with Boron Content:** In the present work it was reported that the Crack-Mouth Opening Displacement values decrease as the Boron content rises in the Ti-64-xB specimens. One possible reason for this to happen could be the increased probability of the presence of big TiB particles being present near the crack-tip. Due to this increased probability, there are chances that these TiB needles crack in a pre-mature manner when tested at such high impact speeds, thus not giving the chance for crack resistance, and acting as crack nucleation sites. The theory being put forward is highly congruent with the research carried out by Morsi *et al* [58], Gorsse *et al* [57] and Sen *et al* [107] where they performed experiments on Ti-TiB Composites, Ti-64-TiB composite and hyper-eutectic compositions of Ti-64-B alloy respectively.

5.2.2 Crack-Tip Opening Angle (CTOA)

The Crack-Tip Opening Angle was calculated using the High-Speed Camera Images and it was observed that the CTOA shows a decreasing trend with increase in Boron Content. The possible reasons for such an observation are as follows:

- As the Boron content increase the complexity of the crack path decreases leading to easier and sharper crack propagations. This reason is supported by the studies done by Sen *et al* [59] where they performed Quasi-Static tests on Ti-64xB (x = 0, 0.05, 0.1 and 0.04 wt %) samples.
- The other reason can be the role of surface roughness. The surface roughness decreases as the Boron content in the Ti-64xB sample rises. This theory is supported by the Fractography images where the fractured surface appears to be less rough with increasing Boron content leading to a decreased tendency for crack resistance and sharper cracks. Sharper the crack, lower the CTOA.

5.2.3 Load-Point Displacement

It was observed in the present study that Load-Point Displacement increases up till 0.04 wt % followed by a steady dip. The following observation can be directly related to the ductility of the samples. The possible reasons for such behaviour are as follows:

- The refinement of the grain size may be one of the factors that could potentially explain the observed phenomenon. However, it is important to remember that if the Boron concentration rises over 0.04 weight percent, the ductility may become constrained due to a potential restriction given by the brittle TiB particles, which frequently embellish the GBs. The conclusion that has been reached is reinforced by Sen *et al*'s [59] research, in which they conducted Quasi-Static tests on different Ti-64-xB samples and observed a similar trend. The ductility of the samples increased gradually until the Boron content reached 0.05 wt. %, after which it dropped precipitously. Therefore, it was found that the sample containing 0.04 B in the present study exhibited the highest ductility among all the compositions tested, which resulted in the highest Load-Point Displacement values.
- Luan *et al*'s [108] research suggests that the refinement of grain size alone cannot fully account for the increase in ductility observed up to 0.04 wt. % of Boron. The segregation of Boron, which enhances the cohesive strength of the β GBs, also plays a significant role. However, the cohesive strength becomes dominant in samples that have a low volume fraction of TiB or that lack them entirely, as in the case of the 0.04 B sample. Conversely, as the Boron content increases, a considerable amount of TiB segregates at the GBs, overpowering the β cohesion-induced strength, which ultimately leads to lower ductility values for Boron-rich samples and consequently reduces the Load-Point Displacement values.

5.2.4 Crack Propagation Speed

By analysing High-Speed Camera Images, it was possible to quantify the crack length and the time required for crack propagation. By dividing the former by the latter, the Crack-Propagation speed could be determined for each sample. It was found that the Crack-Propagation Speed increased with increasing Boron content, except in the case of the 0.04 B sample, which did not fracture. This observation can be attributed to the following reason:

- Through analysis of the Crack Length vs Time curves presented in Figure 4.12, it was observed that the sample with no added Boron (i.e., the 0 B sample) displayed the highest values for crack length. According to the findings reported by Sen *et al* [59], this could be attributed to the complexity of the crack path. However, it was also noted that the duration required for the crack to propagate in this sample was relatively high [~ 275 μs].

- As the Boron content increased, it was found that the crack length decreased nominally due to a reduction in the complexity of the crack paths and reduced surface roughness. However, more significantly, the duration required for the crack to propagate dropped drastically [120-175 μs]. This decrease in the time required for crack propagation ultimately led to an increase in the crack propagation speeds for samples with higher Boron content.

5.2.5 Plastic Zone Size

By analysing the High-Speed Camera Images, it was observed that the 0.04 B sample displayed the greatest plastic zone size. This finding can be attributed to the following possible reason:

- Upon examination of the K_{ID} vs Time curves for all Ti-64-xB samples, it was discovered that the 0.04 B sample exhibited the highest loading rate among the various Ti-64-xB compositions. The loading rate is a critical factor that directly influences the size of the Plastic Zone, which plays a significant role in fracture behaviour. This observation is substantiated by prior research conducted by Anderson and Rosakis [24], who put forward the theory that the Plastic Zone Size (PZS) is dependent on the loading rate experienced at the crack-tip. Therefore, the higher loading rate experienced by the 0.04 B sample likely contributed to its larger Plastic Zone Size.

5.3 Discussions on Dynamic Fracture Toughness

The Dynamic Fracture Toughness (K_{ID}) calculations in this study were built upon the ground-breaking research conducted by Rubio *et al* [85] and Anderson and Rosakis [24]. These influential works served as the basis for determining the DFT values, and upon analysis, it was found that the 0.04 B sample consistently exhibited the highest K_{ID} values among all the tested Ti-64-xB samples, as previously mentioned.

To calculate the K_{ID}, we utilized different methods: CMOD (Crack Mouth Opening Displacement), LPD (Load-Point Displacement), Plastic Zone Size and Peak Load. Remarkably, in each of these approaches, the 0.04 B sample consistently demonstrated the highest K_{ID} values. Whether evaluated through CMOD, LPD, or Plastic Zone Size, the 0.04 B sample consistently displayed superior performance.

The reasons underlying the exceptional behaviour of the 0.04 B sample for each of the case have been elaborated on in earlier sections of this study. The insights provided in these preceding sections shed light on the mechanisms and factors that contribute to the heightened K_{ID} values observed in the 0.04 B sample.

Chapter 6

Conclusions and Future Scope

6.1 Conclusions

In the present study, a comprehensive analysis was conducted to investigate the dynamic fracture response of Ti-64-xB samples. To facilitate this investigation, a customized approach was employed, involving the modification and conversion of a conventional SHPB into a 1B/3PB setup. This modified configuration allowed for the precise examination of the dynamic behaviour of the samples under investigation.

To capture and analyse the dynamic response, two complementary techniques were employed. Firstly, the strain gauge method was utilized to measure and quantify the mechanical properties and behaviour of the samples subjected to dynamic loading. This technique enabled the collection of valuable data on stress, strain, and related parameters, providing insights into the fracture response of the Ti-64-xB specimens.

Additionally, High-speed camera imaging played a pivotal role in capturing detailed visual information during the dynamic loading experiments. This technique allowed for the direct observation of crack initiation, propagation, and other fracture-related phenomena, providing a visual context to complement the quantitative data obtained through strain gauge measurements. Through the combined use of these techniques, the study yielded significant findings and valuable observations. The prime outcomes of this investigation can be summarized as follows:

- An interesting observation made during the study was the notable increase in hardness observed in the Ti-64-xB samples as the Boron content increased. This correlation between Boron content and hardness can be attributed to two primary factors. Firstly, the addition of Boron induced microstructural refinement within the samples, leading to enhanced hardness. Secondly, the presence of TiB particles forming a distinctive necklace-like structure along the grain boundaries also contributed to the overall increase in hardness.
- The relationship between impact speed, Boron content, and Crack-Mouth Opening Displacement (CMOD) was investigated using High-Speed camera imaging, revealing significant insights. It was observed that as the impact speed increased, the CMOD values exhibited an upward trend. This observation was linked to the generation of larger amplitude waves at higher impact speeds, resulting in more severe damage near the crack tip and consequently leading to higher CMOD values. Conversely, an inverse relationship was observed between CMOD values and increasing Boron content. This phenomenon was attributed to the higher likelihood of the presence of TiB particles near the crack tip. These particles, when subjected to such high impact speeds, experienced premature cracking, acting as crack nucleation sites and ultimately leading to their fracture. Consequently, this

premature failure of TiB particles contributed to a decrease in CMOD values as Boron content increased.

- The relationship between Boron content and the Crack-Tip Opening angle was examined, revealing a consistent decrease as Boron content increased. This phenomenon was attributed to two key factors. Firstly, the fractographic images provided evidence of reduced surface roughness on the fractured surfaces. Secondly, the grain size refinement played a significant role in reducing the complexity of the crack path.
- The examination of Load-Point Displacement revealed an initial increase until reaching a Boron content of 0.04 wt. %. Subsequently, a consistent decline was observed. This behaviour can be attributed to the enhanced ductility of the Ti-64-xB sample up to the mentioned composition, followed by a sharp decrease beyond that point.
- Through the utilization of High-Speed Camera Imaging, it was noted that an increase in Boron content resulted in a minor reduction in crack length. However, in contrast, there was a significant decrease in the time required for the samples to fracture. As a consequence, the crack propagation speed accelerated with higher levels of Boron.
- By adjusting the filters within the analysis software of the High-Speed Camera, the Plastic Zone Size was determined. The investigation revealed that the 0.04 B sample displayed the largest PZS amongst the tested Ti-64-xB samples. This notable finding can be attributed to the higher loading rate experienced specifically by the 0.04 B sample, in comparison to the other Ti-64-xB samples. The determination of loading rates was accomplished by analysing the $K_{ID}(t)$ vs Time curves. These findings align with existing literature that supports the aforementioned hypothesis.
- In all the methods outlined earlier, the 0.04B sample consistently demonstrated the highest values for K_{ID} Remarkably, these samples exhibited superior crack growth resistance as they remained intact and did not fracture completely even after undergoing post-dynamic impact conditions.
- By combining the methodologies of Strain Gauge Study and High-Speed Camera Imaging, an insightful revelation emerged from the investigation: the attainment of the Maximum Force occurs precisely at the critical juncture of crack initiation. This finding underscores the importance of the synchronized analysis of strain measurements and visual observation, as it provides a comprehensive understanding of the mechanical behaviour and fracture mechanics at play during the initial stages of crack formation. This knowledge contributes to the broader understanding of the dynamic processes governing crack initiation and propagation, shedding light on the intricate interplay between applied forces, material properties, and structural integrity.

6.2 Future Scope

To gain a comprehensive understanding of the influence of Boron incorporation on the dynamic mechanical properties of Ti-64-xB alloys, it is beneficial to integrate texture analysis. This approach can provide valuable insights into the underlying factors contributing to the anomaly observed in the trend, particularly in the case of the 0.04 B alloy. By combining the investigation of dynamic mechanical properties with texture analysis, a deeper understanding can be attained, unravelling the complex interplay between Boron content, material texture, and the resulting mechanical behaviour.

REFERENCES

[1] C. (Christoph) Leyens and M. (Manfred) Peters, *Titanium and titanium alloys: fundamentals and applications*. Wiley-VCH, 2003.

[2] W. D. Brewer, R. K. Bird, and T. A. Wallace, “Titanium alloys and processing for high-speed aircraft,” 1998.

[3] A. Gomez-Gallegos, P. Mandal, D. Gonzalez, N. Zuelli, and P. Blackwell, “Studies on titanium alloys for aerospace application,” in *Defect and Diffusion Forum*, Trans Tech Publications Ltd, 2018, pp. 419–423. doi: 10.4028/www.scientific.net/DDF.385.419.

[4] R. Santhosh, M. Geetha, and M. Nageswara Rao, “Recent Developments in Heat Treatment of Beta Titanium Alloys for Aerospace Applications,” *Transactions of the Indian Institute of Metals*, vol. 70, no. 7. Springer India, pp. 1681–1688, Sep. 01, 2017. doi: 10.1007/s12666-016-0985-6.

[5] T. L. Jones, K. Kondoh, T. Mimoto, N. Nakanishi, and J. Umeda, “The development of a Ti-6Al-4V alloy via oxygen solid solution strengthening for aerospace & defence applications,” *Key Eng Mater*, vol. 551, pp. 118–126, 2013, doi: 10.4028/www.scientific.net/KEM.551.118.

[6] M. Niinomi and C. J. Boehlert, “Titanium Alloys for Biomedical Applications,” 2015, pp. 179–213. doi: 10.1007/978-3-662-46836-4_8.

[7] L. Y. Chen, Y. W. Cui, and L. C. Zhang, “Recent development in beta titanium alloys for biomedical applications,” *Metals (Basel)*, vol. 10, no. 9, pp. 1–29, Sep. 2020, doi: 10.3390/met10091139.

[8] M. Niinomi, “Mechanical biocompatibilities of titanium alloys for biomedical applications,” *Journal of the Mechanical Behavior of Biomedical Materials*, vol. 1, no. 1. pp. 30–42, Jan. 2008. doi: 10.1016/j.jmbbm.2007.07.001.

[9] H. J. Rack and J. I. Qazi, “Titanium alloys for biomedical applications,” *Materials Science and Engineering C*, vol. 26, no. 8, pp. 1269–1277, Sep. 2006, doi: 10.1016/j.msec.2005.08.032.

[10] A. CASADEBAIGT, D. MONCEAU, and J. HUGUES, “HIGH TEMPERATURE OXIDATION OF TI-6AL-4V ALLOY FABRICATED BY ADDITIVE MANUFACTURING. INFLUENCE ON MECHANICAL PROPERTIES,” *MATEC Web of Conferences*, vol. 321, p. 03006, 2020, doi: 10.1051/matecconf/202032103006.

[11] Z. Liu, B. He, T. Lyu, and Y. Zou, “A Review on Additive Manufacturing of Titanium Alloys for Aerospace Applications: Directed Energy Deposition and Beyond Ti-6Al-4V,” *JOM*, vol. 73, no. 6. Springer, pp. 1804–1818, Jun. 01, 2021. doi: 10.1007/s11837-021-04670-6.

[12] D. P. Yan, T. Hilditch, H. A. Kishawy, and G. Littlefair, “On quantifying the strain rate during chip formation when machining aerospace alloy Ti-5553,” in *Procedia CIRP*, Elsevier B.V., 2013, pp. 123–128. doi: 10.1016/j.procir.2013.06.076.

[13] K. T. Ramesh, “High Strain Ra 33. High Strain Rate and Impact Experiments.”

[14] C. K. H. Dharan and F. E. Hauser, “Determination of Stress-Strain Characteristics at Very High Strain Rates.”

[15] G.L. Wulf and G.T. Richardson, “The measurement of dynamic stress-strain relationships at very high strains Apparatus and techniques.” [Online]. Available: http://iopscience.iop.org/0022-3735/7/3/006

[16] D. Jia and K. T. Ramesh, “A rigorous assessment of the benefits of miniaturization in the Kolsky bar system,” *Exp Mech*, vol. 44, no. 5, pp. 445–454, Oct. 2004, doi: 10.1177/0014485104047608.

[17] G. Singh and U. Ramamurty, “Boron modified titanium alloys,” *Progress in Materials Science*, vol. 111. Elsevier Ltd, Jun. 01, 2020. doi: 10.1016/j.pmatsci.2020.100653.

[18] M. G. Glavicic, P. A. Kobryn, F. Spadafora, and S. L. Semiatin, “Texture evolution in vacuum arc remelted ingots of Ti-6Al-4V.” [Online]. Available: www.elsevier.com/locate/msea

[19] Luterjing G and Williams J.C., *Engineering Materials and Processes*.

[20] Z. feng SHI, H. zhen GUO, J. wei ZHANG, and J. ning YIN, “Microstructure−fracture toughness relationships and toughening mechanism of TC21 titanium alloy with lamellar microstructure,” *Transactions of Nonferrous Metals Society of China (English Edition)*, vol. 28, no. 12, pp. 2440–2448, Dec. 2018, doi: 10.1016/S1003-6326(18)64890-3.

[21] C. Veiga, J. P. Davim, and A. J. R. Loureiro, “PROPERTIES AND APPLICATIONS OF TITANIUM ALLOYS: A BRIEF REVIEW.” [Online]. Available: https://www.researchgate.net/publication/283863116

[22] I. W. Hall and C. Hammond, “Fracture Toughness and Crack Propagation in Titanium Alloys.”

[23] B. Fu, H. Wang, C. Zou, and Z. Wei, “The effects of Nb content on microstructure and fracture behavior of near α titanium alloys,” *Mater Des*, vol. 66, no. PA, pp. 267–273, Feb. 2015, doi: 10.1016/j.matdes.2014.10.069.

[24] D. D. Anderson and A. J. Rosakis, “Dynamic fracture properties of titanium alloys,” *Exp Mech*, vol. 46, no. 3, pp. 399–406, Jun. 2006, doi: 10.1007/s11340-006-6421-9.

[25] Vydehi Arun Joshi, “Titanium Alloys: An Atlas of Structures and Fracture Features,” 2006.

[26] C. Wu and M. Zhan, “Microstructural evolution, mechanical properties and fracture toughness of near β titanium alloy during different solution plus aging heat

treatments," *J Alloys Compd*, vol. 805, pp. 1144–1160, Oct. 2019, doi: 10.1016/j.jallcom.2019.07.134.

[27] A. Chamanfar, M. F. Huang, T. Pasang, M. Tsukamoto, and W. Z. Misiolek, "Microstructure and mechanical properties of laser welded Ti–10V–2Fe–3Al (Ti1023) titanium alloy," *Journal of Materials Research and Technology*, vol. 9, no. 4, pp. 7721–7731, Jul. 2020, doi: 10.1016/j.jmrt.2020.04.028.

[28] J. K. Fan, J. S. Li, H. C. Kou, K. Hua, and B. Tang, "The interrelationship of fracture toughness and microstructure in a new near β titanium alloy Ti-7Mo-3Nb-3Cr-3Al," *Mater Charact*, vol. 96, pp. 93–99, 2014, doi: 10.1016/j.matchar.2014.07.018.

[29] Y. Liu, S. C. V. Lim, C. Ding, A. Huang, and M. Weyland, "Unravelling the competitive effect of microstructural features on the fracture toughness and tensile properties of near beta titanium alloys," *J Mater Sci Technol*, vol. 97, pp. 101–112, Jan. 2022, doi: 10.1016/j.jmst.2021.04.032.

[30] Z. Z. Fang, H. D. Lefler, F. H. Froes, and Y. Zhang, "Introduction to the development of processes for primary Ti metal production," in *Extractive Metallurgy of Titanium: Conventional and Recent Advances in Extraction and Production of Titanium Metal*, Elsevier Inc., 2019, pp. 1–10. doi: 10.1016/B978-0-12-817200-1.00001-6.

[31] R. R. Boyer, "A An overview on the use of titanium in the aerospace industry," 1996.

[32] R. H. Van Stone, J. R. Low, and J. L. Shannon, "Investigation of the Fracture Mechanism of Ti-5AI-2.5Sn at Cryogenic Temperatures."

[33] S. Fujishiro and F. H. Froes, "EFFECT OF PROCESSING ON THE MECHANICAL PROPERTIES OF IMl-829 TITANIUM ALLOYS."

[34] S. G. Lee, Y. S. Ma, G. L. Thimm, and J. Verstraeten, "Product lifecycle management in aviation maintenance, repair and overhaul," *Comput Ind*, vol. 59, no. 2–3, pp. 296–303, Mar. 2008, doi: 10.1016/j.compind.2007.06.022.

[35] "Materials and material requirements for aerospace structures and engines," in *Introduction to Aerospace Materials*, Elsevier, 2012, pp. 39–56. doi: 10.1533/9780857095152.39.

[36] T. S. Tshephe, S. O. Akinwamide, E. Olevsky, and P. A. Olubambi, "Additive manufacturing of titanium-based alloys- A review of methods, properties, challenges, and prospects," *Heliyon*, vol. 8, no. 3. Elsevier Ltd, Mar. 01, 2022. doi: 10.1016/j.heliyon.2022.e09041.

[37] R. Duan, S. Li, B. Cai, W. Zhu, F. Ren, and M. M. Attallah, "A high strength and low modulus metastable β Ti-12Mo-6Zr-2Fe alloy fabricated by laser powder bed fusion in-situ alloying," *Addit Manuf*, vol. 37, Jan. 2021, doi: 10.1016/j.addma.2020.101708.

[38] J. Vishnu, M. Sankar, H. J. Rack, N. Rao, A. K. Singh, and G. Manivasagam, "Effect of phase transformations during aging on tensile strength and ductility of metastable beta titanium alloy Ti–35Nb–7Zr–5Ta-0.35O for orthopedic applications," *Materials Science and Engineering A*, vol. 779, Mar. 2020, doi: 10.1016/j.msea.2020.139127.

[39] S. Kikuchi, Y. Nakamura, K. Nambu, and T. Akahori, "Formation of a hydroxyapatite layer on Ti–29Nb–13Ta–4.6Zr and enhancement of four-point bending fatigue characteristics by fine particle peening," *International Journal of Lightweight Materials and Manufacture*, vol. 2, no. 3, pp. 227–234, Sep. 2019, doi: 10.1016/j.ijlmm.2019.06.001.

[40] Q. Li *et al.*, "Low springback and low Young's modulus in Ti29Nb13Ta4.6Zr alloy modified by Mo addition," *Mater Trans*, vol. 60, no. 9, pp. 1755–1762, 2019, doi: 10.2320/matertrans.ME201912.

[41] Y. L. Hao, S. J. Li, S. Y. Sun, C. Y. Zheng, and R. Yang, "Elastic deformation behaviour of Ti-24Nb-4Zr-7.9Sn for biomedical applications," *Acta Biomater*, vol. 3, no. 2, pp. 277–286, 2007, doi: 10.1016/j.actbio.2006.11.002.

[42] H. Fujii, K. Takahashi, and Y. Yamashita, "Application of Titanium and Its Alloys for Automobile Parts," 2003.

[43] G. Lütjering, "Influence of processing on microstructure and mechanical properties of (alpha + beta) titanium alloys," 1998.

[44] R. Alaghmandfard, C. Dharmendra, A. G. Odeshi, and M. Mohammadi, "Dynamic mechanical properties and failure characteristics of electron beam melted Ti-6Al-4V under high strain rate impact loadings," *Materials Science and Engineering A*, vol. 793, Aug. 2020, doi: 10.1016/j.msea.2020.139794.

[45] S. Nemat-Nasser, "Introduction to high strain rate testing." [Online]. Available: https://www.researchgate.net/publication/285472544

[46] Meyers M A and H.-R. Pak, "Observation of an adiabatic shear band in titanium by high-voltage transmission electron microscopy."

[47] J. Zhu, A. Kamiya, T. Yamada, W. Shi, and K. Naganuma, "Influence of boron addition on microstructure and mechanical properties of dental cast titanium alloys." [Online]. Available: www.elsevier.com/locate/msea

[48] S. Roy, S. Suwas, S. Tamirisakandala, D. B. Miracle, and R. Srinivasan, "Development of solidification microstructure in boron-modified alloy Ti-6Al-4V-0.1B," *Acta Mater*, vol. 59, no. 14, pp. 5494–5510, Aug. 2011, doi: 10.1016/j.actamat.2011.05.023.

[49] S. Tamirisakandala, D. B. Miracle, R. Srinivasan, and J. S. Gunasekera, "Titanium Alloyed with Boron," 2006. [Online]. Available: https://corescholar.libraries.wright.edu/mmehttps://corescholar.libraries.wright.edu/mme/142

[50] S. Tamirisakandala, B. V Vedam, and R. B. Bhat, “Recent Advances in the Deformation Processing of Titanium Alloys.”

[51] S. Tamirisakandala, R. B. Bhat, J. S. Tiley, and D. B. Miracle, “Processing, microstructure, and properties of β titanium alloys modified with boron,” in *Journal of Materials Engineering and Performance*, Dec. 2005, pp. 741–746. doi: 10.1361/105994905X75547.

[52] S. Tamirisakandala and D. B. Miracle, “Microstructure engineering of titanium alloys via small boron additions,” *Int J Adv Eng Sci Appl Math*, vol. 2, no. 4, pp. 168–180, Dec. 2010, doi: 10.1007/s12572-011-0033-z.

[53] H. Feng, Y. Zhou, D. Jia, Q. Meng, and J. Rao, “Growth mechanism of in situ TiB whiskers in spark plasma sintered TiB/Ti metal matrix composites,” *Cryst Growth Des*, vol. 6, no. 7, pp. 1626–1630, Jul. 2006, doi: 10.1021/cg050443k.

[54] K. B. Panda and K. S. R. Chandran, “First principles determination of elastic constants and chemical bonding of titanium boride (TiB) on the basis of density functional theory,” *Acta Mater*, vol. 54, no. 6, pp. 1641–1657, Apr. 2006, doi: 10.1016/j.actamat.2005.12.003.

[55] O. M. Ivasishin, R. V. Teliovych, V. G. Ivanchenko, S. Tamirisakandala, and D. B. Miracle, “Processing, microstructure, texture, and tensile properties of the Ti-6Al-4V-1.55B eutectic alloy,” *Metall Mater Trans A Phys Metall Mater Sci*, vol. 39, no. 2, pp. 402–416, Feb. 2008, doi: 10.1007/s11661-007-9425-x.

[56] J. Li, L. Liu, S. Xu, J. Zhang, and W. She, “First-principles study of mechanical, electronic properties and anisotropic deformation mechanisms of TiB under uniaxial compressions,” *Appl Phys A Mater Sci Process*, vol. 125, no. 3, Mar. 2019, doi: 10.1007/s00339-019-2523-y.

[57] S. Gorsse and D. B. Miracle, “Mechanical properties of Ti-6Al-4V/TiB composites with randomly oriented and aligned TiB reinforcements,” *Acta Mater*, vol. 51, no. 9, pp. 2427–2442, May 2003, doi: 10.1016/S1359-6454(02)00510-4.

[58] K. Morsi and V. V. Patel, “Processing and properties of titanium-titanium boride (TiBw) matrix composites - A review,” in *Journal of Materials Science*, Mar. 2007, pp. 2037–2047. doi: 10.1007/s10853-006-0776-2.

[59] I. Sen, S. Tamirisakandala, D. B. Miracle, and U. Ramamurty, “Microstructural effects on the mechanical behavior of B-modified Ti-6Al-4V alloys,” *Acta Mater*, vol. 55, no. 15, pp. 4983–4993, Sep. 2007, doi: 10.1016/j.actamat.2007.05.009.

[60] I. Sen, K. Gopinath, R. Datta, and U. Ramamurty, “Fatigue in Ti-6Al-4V-B alloys,” *Acta Mater*, vol. 58, no. 20, pp. 6799–6809, Dec. 2010, doi: 10.1016/j.actamat.2010.09.008.

[61] I. Sen and U. Ramamurty, “Elastic modulus of Ti-6Al-4V-xB alloys with B up to 0.55 wt.%,” *Scr Mater*, vol. 62, no. 1, pp. 37–40, Jan. 2010, doi: 10.1016/j.scriptamat.2009.09.022.

[62] R. Pederson, R. Gaddam, and M. L. Antti, “Microstructure and mechanical behavior of cast Ti-6Al-4V with addition of boron,” *Central European Journal of Engineering*, vol. 2, no. 3, pp. 347–357, 2012, doi: 10.2478/s13531-012-0004-6.

[63] Weinong. W. Chen and B. Song, *Split Hopkinson (Kolsky) Bar*. 2011. [Online]. Available: www.springer.com/series/1161

[64] H. Kolsky, “An Investigation of the Mechanical Properties of Materials at very High Rates of Loading.”

[65] C. J. Boehlert, C. J. Cowen, S. Tamirisakandala, D. J. McEldowney, and D. B. Miracle, “In situ scanning electron microscopy observations of tensile deformation in a boron-modified Ti-6Al-4V alloy,” *Scr Mater*, vol. 55, no. 5, pp. 465–468, Sep. 2006, doi: 10.1016/j.scriptamat.2006.05.008.

[66] O. M. Ivasishin, R. V. Teliovych, V. G. Ivanchenko, S. Tamirisakandala, and D. B. Miracle, “Processing, microstructure, texture, and tensile properties of the Ti-6Al-4V-1.55B eutectic alloy,” *Metall Mater Trans A Phys Metall Mater Sci*, vol. 39, no. 2, pp. 402–416, Feb. 2008, doi: 10.1007/s11661-007-9425-x.

[67] G. G. Yapici, I. Karaman, Z. P. Luo, and H. Rack, “Microstructure and mechanical properties of severely deformed powder processed Ti-6Al-4V using equal channel angular extrusion,” *Scr Mater*, vol. 49, no. 10 SPEC., pp. 1021–1027, 2003, doi: 10.1016/S1359-6462(03)00484-6.

[68] A. C. Fischer-Cripps, “Contact Mechanics,” 2011, pp. 1–19. doi: 10.1007/978-1-4419-9872-9_1.

[69] K. Euh, J. Lee, S. Lee, Y. Koo, and N. J. Kim, “Microstructural modification and hardness improvement in boride/Ti-6Al-4V surface-alloyed materials fabricated by high-energy electron beam irradiation,” 2001. [Online]. Available: www.elsevier.com/locate/scriptamat

[70] R. 0 Ritchie, J. F. Knob, and J. R. Rice, “On the relation between Critical Tensile Stress and Fracture Toughness in Mild Steel,” Pergamon Press, 1973.

[71] Y. Yu, S. Hui, X. Mi, W. Ye, and Q. Gao, “0.1wt% Boron addition Effect on dynamic compressive mechanical properties of Ti-6Al-4V alloy,” *MATEC Web of Conferences*, 2016, doi: 10.1051/05018.

[72] H. HOMMA, Y. KANTO, and K. TANAKA, “CLEAVAGE FRACTURE UNDER SHORT PULSE LOADING,” *Le Journal de Physique IV*, vol. 01, no. C3, pp. C3-589-C3-596, Oct. 1991, doi: 10.1051/jp4:1991383.

[73] G. Weisbrod and D. Rittel, “A method for dynamic fracture toughness determination using short beams,” 2000.

[74] A. Shukla, *Dynamic Fracture Mechanics*. 2006.

[75] S. Rizal and H. Homma, “Dimple fracture under short pulse loading,” 2000.

[76] S. Rizal, H. Homma, M. Nazer, and E. Kishida, “Experimental approach to dimple fracture mechanisms under short pulse loading,” 2017. [Online]. Available: www.elsevier.com/locate/engfracmech

[77] H. Wada, “DETERMINATION OF DYNAMIC FRACTURE TOUGHNESS FOR PMMA,” 1992.

[78] H. Wada, M. Seika, C. A. Calder, and T. C. Kennedy, “TECHNICAL NOTE MEASUREMENT OF IMPACT FRACTURE TOUGHNESS FOR PMMA WITH SINGLE-POINT BENDING TEST USING AN AIR GUN,” 1993.

[79] H. Wada, M. Seika, T. C. Kennedy, C. A. Calder, and K. Murase, “INVESTIGATION OF LOADING RATE AND PLATE THICKNESS EFFECTS ON DYNAMIC FRACTURE TOUGHNESS OF PMMA,” 1996.

[80] A. Bertram and J. F. Kalthoff, “Crack propagation toughness of rock for the range of low to very high crack speeds,” in *Key Engineering Materials*, Trans Tech Publications Ltd, 2003, pp. 423–430. doi: 10.4028/www.scientific.net/kem.251-252.423.

[81] J. F. Kalthoff, “FRACTURE BEHAVIOR UNDER HIGH RATES OF LOADING,” 1986.

[82] O. Samudrala and A. J. Rosakis, “Effect of loading and geometry on the subsonic/intersonic transition of a bimaterial interface crack.” [Online]. Available: www.elsevier.com/locate/engfracmech

[83] J. Lambros and A. J. Rosakis, “An Experimental Study of Dynamic Delamination of Thick Fiber Reinforced Polymeric Matrix Composites.”

[84] R. A. W. Mines and C. Ruiz, “DYNAMIC BEHAVIOUR OF THE INSTRUMENTED CHARPY TEST.,” in *Journal de Physique (Paris), Colloque*, Aug. 1985, pp. 187–196. doi: 10.1051/jphyscol:1985524.

[85] L. Rubio, J. Fernandez-Sfiez, and C. Navarro, “Determination of Dynamic Fracture-initiation Toughness using Three-point Bending Tests in a Modified Hopkinson Pressure Bar.”

[86] C. Ruiz and R. A. W. Mines, “The Hopkinson pressure bar: an alternative to the instrumented pendulum for Charpy tests,” 1985.

[87] R. A. W. Mines, “Analysis of the Hopkinson Pressure Bar loaded Instrumented Charpy Test using an inertial modelling technique,” 1991.

[88] W. G. Guo, Y. L. Li, and Y. Y. Liu, “Analytical and experimental determination of dynamic impact stress intensity factor for 40 Cr steel.”

[89] X. Zejian, L. Yulong, and L. Yuanyong, “EFFECT OF LOADING RATE ON MODE I DYNAMIC FRACTURE TOUGHNESS OF HIGH STRENGTH STEELS 40Cr AND 30CrMnSiNi2A,” *Acta Metallurgica Sinica*, vol. 42, no. 9, pp. 965–970, 2006.

[90] C. E. Anderson, “A novel method for determining dynamic fracture toughness,” AIP Publishing, Feb. 2003, pp. 505–508. doi: 10.1063/1.1303525.

[91] V. K. Srivastava and K. Maile, “Measurement of critical stress intensity factor in C/C-SiC composites under dynamic and static loading conditions,” *Compos Sci Technol*, vol. 64, no. 9, pp. 1209–1217, Jul. 2004, doi: 10.1016/j.compscitech.2003.09.025.

[92] F. Jiang and K. S. Vecchio, “Experimental investigation of dynamic effects in a two-bar/three-point bend fracture test,” *Review of Scientific Instruments*, vol. 78, no. 6, 2007, doi: 10.1063/1.2746630.

[93] T. Yokoyama and K. Kishida, “A Novel Impact Three-point Bend Test Method for Determining Dynamic Fracture-initiation Toughness,” *Exp Mech*, pp. 188–194, 1989.

[94] C. Bacon and J. L. Lataillade, “Dynamic Fracture Toughness Determined from Load-point Displacement,” *Exp Mech*, pp. 217–223, 1994.

[95] G. V Guinea, J. Planas, and M. Elices, “Stress intensity factor, compliance and CMOD for a general three-point-bend beam,” 1998.

[96] K. Kishimoto, M. Kuroda, S. Aoki, and M. Sakata, “SIMPLE FORMULAS FOR DYNAMIC FRACTURE MECHANICS PARAMETERS OF ELASTIC AND VISCOELASTIC THREE-POINT BEND SPECIMENS BASED ON TIMOSHENKO’S BEAM THEORY,” *Fracture*, pp. 3177–3184, 1984.

[97] S. Roy and S. Suwas, “Deformation mechanisms during superplastic testing of Ti-6Al-4V-0.1B alloy,” *Materials Science and Engineering A*, vol. 574, pp. 205–217, Jul. 2013, doi: 10.1016/j.msea.2013.03.013.

[98] A. M. Muiruri, M. Maringa, W. B. Du Preez, and L. M. Masu, “DYNAMIC BEHAVIOUR OF DIRECT METAL LASER SINTERED TI-6AL-4V (ELI) UNDER HIGH STRAIN RATES IN COMPRESSION LOADING.”

[99] S. Liu, D. Liu, and S. Liu, “Transgranular fracture in low temperature brittle fracture of high nitrogen austenitic steel,” *J Mater Sci*, vol. 42, no. 17, pp. 7514–7519, Aug. 2007, doi: 10.1007/s10853-007-1614-x.

[100] H. R. Ammar, A. M. Samuel, F. H. Samuel, E. Simielli, G. K. Sigworth, and J. C. Lin, “Influence of aging parameters on the tensile properties and quality index of Al-9 pct Si-1.8 pct Cu-0.5 pct Mg 354-type casting alloys,” *Metall Mater Trans A Phys Metall Mater Sci*, vol. 43, no. 1, pp. 61–73, Jan. 2012, doi: 10.1007/s11661-011-0808-7.

[101] A. Lu, X. Chang, S. Hu, Y. Xia, and M. Li, “Impact of Moisture Content on the Brittle-Ductile Transition and Microstructure of Sandstone under Dynamic Loading Conditions,” *Advances in Civil Engineering*, vol. 2021, 2021, doi: 10.1155/2021/6690171.

[102] J. Yao *et al.*, “Influence of heat-treatment on the dynamic behavior of 3D laser-deposited Ti–6Al–4V alloy,” *Materials Science and Engineering A*, vol. 677, pp. 153–162, Nov. 2016, doi: 10.1016/j.msea.2016.09.036.

[103] D. K. Francis, W. R. Whittington, W. B. Lawrimore, P. G. Allison, S. A. Turnage, and J. J. Bhattacharyya, “Split Hopkinson Pressure Bar Graphical Analysis Tool,” *Exp Mech*, vol. 57, no. 1, pp. 179–183, Jan. 2017, doi: 10.1007/s11340-016-0191-9.

[104] S. Sahraoui, A. El Mahi, and B. Castagnède, “Measurement of the dynamic fracture toughness with notched PMMA specimen under impact loading,” *Polym Test*, vol. 28, no. 7, pp. 780–783, 2009, doi: 10.1016/j.polymertesting.2009.06.005.

[105] X. U. Xiaohe, “A NEW METHOD FOR MEASURING DYNAMIC FRACTURE TOUGHNESS OF ROCK,” 1990.

[106] M. Shazly, V. Prakash, and S. Draper, “Dynamic Fracture Initiation Toughness at Elevated Temperatures With Application to the New Generation of Titanium Aluminides Alloys.” [Online]. Available: www.worldscientific.com

[107] I. Sen, L. Maheshwari, S. Tamirisakandala, D. B. Miracle, and U. Ramamurty, “Micromechanisms of damage in a hypereutectic Ti-6Al-4V-B alloy,” *Materials Science and Engineering A*, vol. 518, no. 1–2, pp. 162–166, Aug. 2009, doi: 10.1016/j.msea.2009.04.039.

[108] J. H. Luan, Z. B. Jiao, L. Heatherly, E. P. George, G. Chen, and C. T. Liu, “Effects of boron on the fracture behavior and ductility of cast Ti-6Al-4V alloys,” *Scr Mater*, vol. 100, pp. 90–93, Apr. 2015, doi: 10.1016/j.scriptamat.2014.12.022.